

Pt₃Ti Nanoparticles: Fine Dispersion on SiO₂ Supports, Enhanced Catalytic CO Oxidation, and Chemical Stability at Elevated Temperatures

Govindachetty Saravanan,^{*,†} Hideki Abe,^{*,†} Ya Xu,[†] Nobuaki Sekido,[†] Hirohito Hirata,[‡] Shin-ichi Matsumoto,[‡] Hideki Yoshikawa,[§] and Yoko Yamabe-Mitarai[†]

[†]National Institute for Materials Science (NIMS), Sengen 1-2-1, Tsukuba, Ibaragi 305-0047, Japan,

[‡]Toyota Motor Corporation, Mishuku 1200, Susono, Shizuoka 410-1107, Japan, and [§]NIMS Beamline Station at SPring-8, 1-1-1 Kouto, Sayo, Hyogo 679-5148, Japan

Received March 8, 2010. Revised Manuscript Received April 30, 2010

A platinum-based intermetallic phase with an early *d*-metal, Pt₃Ti, has been synthesized in the form of nanoparticles (NPs) dispersed on silica (SiO₂) supports. The organometallic Pt and Ti precursors, Pt(1,5-cyclooctadiene)Cl₂ and TiCl₄(tetrahydrofuran)₂, were mixed with SiO₂ and reduced by sodium naphthalide in tetrahydrofuran. Stoichiometric Pt₃Ti NPs with an average particle size of 2.5 nm were formed on SiO₂ (particle size: 20–200 nm) with an atomically disordered FCC-type structure (*Fm**m*; *a* = 0.39 nm). A high dispersivity of Pt₃Ti NPs was achieved by adding excessive amounts of SiO₂ relative to the Pt precursor. A 50-fold excess of SiO₂ resulted in finely dispersed, SiO₂-supported Pt₃Ti NPs that contained 0.5 wt % Pt. The SiO₂-supported Pt₃Ti NPs showed a lower onset temperature of catalysis by 75 °C toward the oxidation reaction of CO than did SiO₂-supported pure Pt NPs with the same particle size and Pt fraction, 0.5 wt %. The SiO₂-supported Pt₃Ti NPs also showed higher CO conversion than SiO₂-supported pure Pt NPs even containing a 2-fold higher weight fraction of Pt. The SiO₂-supported Pt₃Ti NPs retained their stoichiometric composition after catalytic oxidation of CO at elevated temperatures, 325 °C. Pt₃Ti NPs show promise as a catalytic center of purification catalysts for automobile exhaust due to their high catalytic activity toward CO oxidation with a low content of precious metals.

Introduction

Bimetallic nanoparticles (NPs) have drawn much attention in recent years owing to their outstanding catalytic, electronic, and/or optical properties.^{1–5} Bimetallic NPs have been obtained either as an alloy or as a core–shell structure by either simultaneous or sequential reduction of precursors, respectively.^{6–9} Finely dispersed bimetallic NPs on solid supports have been used for a variety of catalytic applications. For instance, carbon-supported

bimetallic Pt–M (M = Ru, Cu, Au, Pd, Ni, etc.) NPs have been used as active electrocatalysts for fuel cells.^{10–17} Selective hydrogenation of various organic molecules has been achieved by Pd-based bimetallic NPs deposited on carbon and/or TiO₂ supports.^{18–20} CeO₂-, SiO₂-, or γ-Al₂O₃-supported bimetallic NPs have been used for the purification of automobile exhaust.^{21–26}

The catalytic performance of alloy and core–shell NPs, however, tends to decay with use due to the migration of surface atoms into bulk when used at elevated temperatures for exhaust purification. Bimetallic alloy NPs containing late *d*-metal elements are readily decomposed in an oxidizing atmosphere of exhaust. NPs of intermetallic compounds that have higher thermal and chemical stabilities than alloy NPs would be desirable as a practical catalyst for exhaust purification. A Pt-based intermetallic compound containing an early *d*-metal element, Pt₃Ti, is a thermally stable material with a high enthalpy of formation, ΔH_f = –298 (kJ/mol of Ti).²⁷ Moreover, the authors and their collaborators recently showed that NPs of Pt₃Ti have great promise as

- *To whom correspondence should be addressed. E-mail: SARAVANAN.Govindachetty@nims.go.jp; ABE.Hideki@nims.go.jp.
- (1) Thomas, J. M.; Raja, R.; Johnson, B. F. G.; Hermans, S.; Jones, M. D.; Khimyak, T. *Ind. Eng. Chem. Res.* **2003**, *42*, 1563–1570.
- (2) Bronstein, L. M.; Chernyshov, D. M.; Volkov, I. O.; Ezernitskaya, M. G.; Valetsky, P. M.; Matveeva, V. G.; Sulman, E. M. *J. Catal.* **2000**, *196*, 302–314.
- (3) Mulvaney, P.; Giersig, M.; Henglein, A. *J. Phys. Chem.* **1992**, *96*, 10419–10424.
- (4) Mulvaney, P. *Langmuir* **1996**, *12*, 788–800.
- (5) Chushak, Y. G.; Bartell, L. S. *J. Phys. Chem. B* **2003**, *107*, 3747–3751.
- (6) Link, S.; Wang, S. Z. L.; El-Sayed, M. A. *J. Phys. Chem. B* **1999**, *103*, 3529–3535.
- (7) Damle, C.; Kumar, A.; Sastry, M. *J. Phys. Chem. B* **2002**, *106*, 297–302.
- (8) Rivas, L.; Sanchez-Cortes, S.; Garcia-Ramos, J. V.; Morcillo, G. *Langmuir* **2000**, *16*, 9722–9728.
- (9) Henglein, A. *J. Phys. Chem. B* **2000**, *104*, 2201–2203.
- (10) Long, J. W.; Stroud, R. M.; Swider-Lyons, K. E.; Rolison, D. R. *J. Phys. Chem. B* **2000**, *104*, 9772–9776.
- (11) Schmidt, T. J.; Gasteiger, H. A.; Behm, R. J. *J. Electrochem. Soc.* **1999**, *146*, 1296–1304.
- (12) Costamanga, P.; Srinivasan, S. *J. Power Sources* **2001**, *102*, 242–252.
- (13) Casado-Rivera, E.; Gál, Z.; Angelo, A. C. D.; Lind, C.; DiSalvo, F. J.; Abruna, H. D. *Chem. Phys. Chem.* **2003**, *4*, 193–199.
- (14) Casado-Rivera, E.; Volpe, D. J.; Alden, L. R.; Lind, C.; Downie, C.; Vázquez-Alvarez, T.; Angelo, A. C. D.; DiSalvo, F. J.; Abruna, H. D. *J. Am. Chem. Soc.* **2004**, *126*, 4043–4049.
- (15) Volpe, D. J.; Casado-Rivera, E.; Alden, L. R.; Lind, C.; Hagerdon, K.; Downie, C.; Korzeniewski, C.; DiSalvo, F. J.; Abruna, H. D. *J. Electrochem. Soc.* **2004**, *151*, A971–A977.
- (16) Luo, J.; Njoki, P. N.; Lin, Y.; Mott, D.; Wang, L.; Zhong, C. *J. Langmuir* **2006**, *22*, 2892–2898.

- (17) Yen, C. H.; Shimizu, K.; Lin, Y.-Y.; Bailey, F.; Cheng, I. F.; Wai, C. M. *Energy Fuels* **2007**, *21*, 2268–2271.
- (18) Yoon, B.; Wai, C. M. *J. Am. Chem. Soc.* **2005**, *127*, 17174–17175.
- (19) Rebrov, E. V.; Klinger, E. A.; Berenguer-Murcia, A.; Sulman, E. M.; Schouten, J. C. *Org. Proc. Res. Dev.* **2009**, *13*, 991–998.
- (20) Yoon, B.; Pan, H.-B.; Wai, C. M. *J. Phys. Chem. C* **2009**, *113*, 1520–1525.
- (21) Abdelsayed, V.; Aljarash, A.; El-shall, M. S.; Al Othman, Z. A.; Alghamdi, A. H. *Chem. Mater.* **2009**, *21*, 2825–2834.
- (22) Yen, C.-W.; Lin, M.-L.; Wang, A.; Chen, S.-A.; Chen, J.-M.; Mou, C. Y. *J. Phys. Chem. C* **2009**, *113*, 17831–17839.
- (23) Liu, L.; Guan, X.; Li, Z.; Zi, X.; Dai, H.; He, H. *Appl. Catal., B* **2009**, *90*, 1–9.
- (24) Lang, H.; Maldonado, S.; Stevenson, K. J.; Chandler, B. D. *J. Am. Chem. Soc.* **2004**, *126*, 12949–12956.
- (25) Zhou, S.; McIlwrath, K.; Jackson, G.; Eichhorn, B. *J. Am. Chem. Soc.* **2006**, *128*, 1780–1781.
- (26) Hoover, N. N.; Auten, B. J.; Chandler, B. D. *J. Phys. Chem. B* **2006**, *110*, 8606–8612.
- (27) Meschter, P. J.; Warrell, W. L. *Met. Trans.* **1976**, *7A*, 299–305.

an electrocatalyst for direct methanol fuel cells.²⁸ Pt₃Ti NPs show much higher electrocatalytic activities than either pure Pt or Pt–Ru NPs toward the oxidation of C1-fuels including methanol and/or formic acid. The outstanding C1-oxidation performance of Pt₃Ti NPs indicated that the material may be applicable to purifying CO in automobile exhaust.

Unlike direct methanol fuel cells, however, exhaust purification is usually performed at elevated temperatures in oxygen (O₂)-containing atmospheres. Pt₃Ti NPs have been synthesized in the form of either free NPs²⁸ or graphite-supported NPs.²⁹ Free NPs readily agglomerate at elevated temperatures, diminishing the active surface area. Graphite supports can be decomposed when exposed to O₂-containing atmospheres. It is therefore necessary to develop a method to finely disperse Pt₃Ti NPs on a supporting material that is chemically and thermally stable under the catalytic conditions of exhaust purification.

Various methods and supporting materials have been developed to disperse Pt–M NPs to achieve large active surface areas.^{30–34} Zeolite supercages were used to trap Pt–M NPs to suppress agglomeration.³⁵ Organic surfactants and dendrimers were used to produce finely dispersed Pt–M NPs on solid supports.^{26,36,37} Some of the supporting materials, such as porous CeO₂, significantly enhanced the catalytic activity of supported NPs through charge transfer from valence-fluctuating Ce³⁺/Ce⁴⁺ to NPs (supporting-material effects).³⁸ To explore the potential of Pt₃Ti NPs as a catalytic center for exhaust purification, a careful comparison would be desired between Pt₃Ti NPs and reference NPs, both of which are supported by a catalytically inert support. SiO₂ is a chemically and thermally stable supporting material and may not show supporting-material effects because of the valence stability of Si⁴⁺. SiO₂ is therefore a good supporting material for Pt₃Ti NPs to evaluate their inherent catalytic performance toward automobile exhaust purification.

This paper describes a wet-chemical synthesis of SiO₂-supported Pt₃Ti NPs using air sensitive Pt and Ti precursors. The inherent catalytic activity of Pt₃Ti NPs was evaluated in comparison to that of SiO₂-supported pure Pt NPs with the same particle size, loading weight, and dispersivity. The crystal structure of SiO₂-supported Pt₃Ti NPs was characterized by powder X-ray diffraction (*p*XRD) and selective area electron diffraction (SAED) analysis. The chemical composition of SiO₂-supported Pt₃Ti NPs was examined by electron-probe microanalysis (EPMA) and inductively coupled plasma mass spectrometry (ICP-MS). The core-level state of Pt₃Ti NPs on SiO₂ supports was examined by hard X-ray photoemission spectroscopy (HX-PES). The particle size, morphology, and dispersivity of Pt₃Ti NPs on SiO₂ supports were examined with an ultrahigh vacuum scanning transmission electron microscope (UHV-STEM). Catalytic oxidation

of CO was carried out at elevated temperatures to compare the CO purification activity of SiO₂-supported Pt₃Ti NPs to that of SiO₂-supported pure Pt NPs.

Experimental Section

Materials. The organometallic Pt precursor, Pt(1,5-cyclooctadiene)Cl₂ (99%), was purchased from STREM Chemicals. The Ti precursor, Ti(tetrahydrofuran)₂Cl₄, was synthesized from TiCl₄ (99%, Kishida Chemicals) according to a literature method.³⁹ SiO₂ (particle size 20–200 nm with specific surface area = 83 m² g⁻¹) was obtained from C.I. Kasei Co. Ltd. The pore size of the SiO₂ support ranged from 10 to 100 nm, centered at 50 nm. Sodium metal and naphthalene were purchased from Aldrich and Kishida Chemicals, respectively. Pt (99%) and Ti (99%) metals were purchased from Furuya-Kinzoku Co. Ltd. The solvents, tetrahydrofuran (99.5%), hexane (96%), and methanol (99.8%), were received from Kishida Chemicals. Tetrahydrofuran and hexane were distilled prior to use under a dry Ar (99.9999%) atmosphere to remove oxygen and moisture. Methanol was deaired by bubbling with dry Ar for 30 min. SiO₂ was dried at 200 °C for 3 h under a dry Ar atmosphere. The chemicals and solvents were always treated under a dry Ar atmosphere.

Synthesis of Free and SiO₂-Supported Pt₃Ti Nanoparticles. An O₂- and moisture-free environment (<5 ppm) is necessary to synthesize Pt₃Ti NPs because the Pt and Ti precursors are highly air-sensitive. An aliquot of 0.04 mmol (15.6 mg) of Pt precursor and 0.16 mmol (55.7 mg) of Ti precursor were weighed under a dry Ar atmosphere. Various amounts of SiO₂ with relative weights to the Pt precursor, *x*, of *x* = 2 (31.2 mg), 10 (156 mg), and 50 (780 mg) were weighed also under a dry Ar atmosphere. A precursor solution for free Pt₃Ti NPs without SiO₂ supports was prepared by dissolving the Pt and Ti precursors in 10 mL of tetrahydrofuran. Precursors for SiO₂-supported Pt₃Ti NPs were prepared by dissolving the Pt and Ti precursors in 30 mL of tetrahydrofuran along with the necessary amounts of SiO₂. The precursor solutions were stirred for 30 min under a dry Ar atmosphere.

A sodium naphthalide solution was prepared by dissolving 1.5 mmol each of sodium metal (34.5 mg) and naphthalene (192.3 mg) in 50 mL of tetrahydrofuran. The precursor solutions were transferred into the sodium naphthalide solution without being exposed to air. The dark green color of sodium naphthalide turned dark brown immediately upon transfer of the precursor solutions. The dark brown solution was stirred overnight to complete the reaction. The solvent was removed by distillation under reduced pressure to leave a dark brown precipitate. The precipitate was washed with hexane and methanol in sequence. The precipitate was separated from the washing solvents by centrifugation at 6000 rpm for 10 min and dried under vacuum at room temperature over several hours. The obtained products were stable in air and were black in color (free Pt₃Ti NPs and *x* = 2) or gray in color (*x* = 10 and 50).

Characterization. *p*XRD was performed for structural characterization using Cu K α radiation (RIGAKU RINT2000; λ = 0.15418 nm) over 12 h at a count time of 10 s with 0.02° increments. A UHV-STEM (TECNAL G²) was used for microscopic observation of the products. The products were dispersed in methanol by sonication and recovered with collodion-coated copper TEM grids. The chemical composition of the products was determined using an EPMA instrument attached to the UHV-STEM and by ICP-MS (PE-3300 DV). SAED was performed to characterize the product before/after catalytic oxidation of CO. For ICP-MS, 5 mg of the products were dissolved in 12 mL of aqua regia which was buffered by 2 mL of HF and 1 g of B₂O₃. HX-PES measurements were performed using an X-ray with a photon energy of 5.95 keV, on the beamline BL15XU of the Spring-8 facility.⁴⁰

(28) Abe, H.; Matsumoto, F.; Alden, L. R.; Warren, S. C.; Abruna, D. H.; DiSalvo, F. J. *J. Am. Chem. Soc.* **2008**, *130*, 5452–5458.

(29) Ding, E.; More, K. L.; He, T. *J. Power. Sources* **2008**, *175*, 794–799.

(30) Mihut, C.; Descomme, C.; Duprez, D.; Amiridis, M. D. *J. Catal.* **2003**, *212*, 125–135.

(31) Shen, J.; Hill, J. M.; Ramachandra, M. W.; Podkolzin, S. G.; Dumesic, J. A. *Catal. Lett.* **1999**, *60*, 1–9.

(32) Schwank, J.; Balakrishnan, K.; Sachdev, A. In *New Frontiers in Catalysis: Proceedings of the 10th International Congress on Catalysis*; Solymosi, F., Ed.; Elsevier: Amsterdam, 1993; pp 905–918.

(33) Chandler, B. D.; Schabel, A. B.; Blanford, C. F.; Pignolet, L. H. *J. Catal.* **1999**, *187*, 367–383.

(34) Balakrishnan, K.; Sachdev, A.; Schwank, J. *J. Catal.* **1990**, *121*, 441–445.

(35) Riahi, G.; Guillemot, D.; Polisset-Thfoin, M.; Khodadadi, A. A.; Fraissard, J. *Catal. Today* **2002**, *72*, 115–121.

(36) Gupta, G.; Patel, M. N.; Ferrer, D.; Heitsch, A. T.; Korgel, B. A.; Jose-Yacaman, M.; Johnston, K. P. *Chem. Mater.* **2008**, *20*, 5005–5015.

(37) Zhao, M.; Crooks, R. M. *Adv. Mater.* **1999**, *11*, 217–220.

(38) Martinez-Huerta, M. V.; Deo, G.; Fierro, J. L. G.; Bañares, M. A. *J. Phys. Chem. C* **2007**, *111*, 18708–18714.

(39) *Inorganic Synthesis*, Vol. XXI; Fackler, J. P., Ed.; Wiley and Sons: New York, 1982; pp 135–140.

(40) Ohsawa, T.; Adachi, Y.; Sakaguchi, I.; Matsumoto, K.; Haneda, H.; Ueda, S.; Yoshikawa, H.; Kobayashi, K.; Ohashi, N. *Chem. Mater.* **2009**, *21*, 144–150.

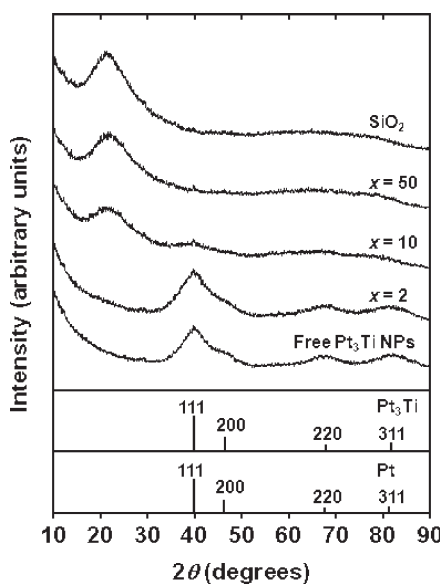


Figure 1. *p*XRD profiles for free Pt_3Ti NPs and SiO_2 -supported Pt_3Ti NPs with various amounts of SiO_2 , x , relative to the Pt precursors. Simulated *p*XRD peaks for atomically disordered Pt_3Ti and pure Pt are shown by solid lines.

The core-level state of the products was examined at room temperature in UHV with an electron energy analyzer (Scienta R4000). Samples for HX-PES measurements were prepared by mixing the products with carbon black (Vulcan XC-72, Cabot Co. Ltd.). The HX-PES spectra were referenced to the Fermi edge of a Au standard. A bulk sample of Pt_3Ti was prepared as the reference surface. Pt and Ti metals with a mole ratio of 3:1 (0.9244 and 0.0756 g for Pt and Ti, respectively) were, using an arc furnace, molten and cooled to room temperature in a pure Ar atmosphere (99.9999%) to obtain the desired material.

CO Oxidation Catalysis. A catalytic CO oxidation reaction was performed over the as-synthesized, SiO_2 -supported catalysts in a conventional fixed-bed flow microreactor setup equipped with a gas chromatograph and a thermal conductivity detector.^{41,42} An aliquot of 50 mg of the SiO_2 -supported catalysts was placed in the microreactor and subjected to a constant flow (100 mL min^{-1}) of feed gas with volume fractions of 2 vol % CO, 1 vol % O₂, and 97 vol % helium (Sumitomo Seika Chemicals Co. Ltd.). The composition of the outlet gas from the microreactor was analyzed in the temperature range from room temperature to 325 °C. The conversion rate of CO to carbon dioxide (CO₂) was calculated as the ratio of the volume fraction of CO₂ to that of CO in the outlet gas.

Results and Discussion

Figure 1 shows the *p*XRD profiles for free Pt_3Ti NPs and the SiO_2 -supported Pt_3Ti NPs with different amounts of SiO_2 support. The *p*XRD profile for free Pt_3Ti NPs shows three broad peaks at $2\theta = 40^\circ$, 68° , and 82° . The observed peaks are assigned to the 111, 220, and 311 reflections of an atomically disordered Pt_3Ti phase with the FCC-type structure ($Fm\bar{3}m$; $a = 0.39 \text{ nm}$).²⁸ The lattice parameter of the atomically disordered Pt_3Ti phase is close to that of pure Pt ($Fm\bar{3}m$; $a = 0.3922 \text{ nm}$).⁴³ The *p*XRD profile for the product with $x = 2$ is virtually identical to that for free Pt_3Ti NPs, indicating that this product contains a high content of Pt_3Ti NPs. The peaks corresponding to Pt_3Ti NPs become weak with an increasing amount of x and disappear for

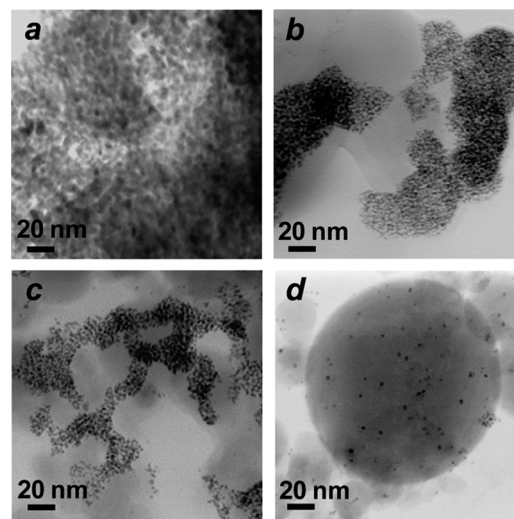


Figure 2. Bright field UHV-STEM images of free Pt_3Ti NPs (a) and SiO_2 -supported Pt_3Ti NPs with various amounts of SiO_2 relative to Pt precursors: $x = 2$ (b), $x = 10$ (c), and $x = 50$ (d).

$x = 50$. In addition to the reflections of Pt_3Ti NPs, a broad 111 reflection of amorphous SiO_2 is observed at $2\theta = 22^\circ$ for $x = 10$ and above. The average particle size of free Pt_3Ti NPs was determined to be 2.5 nm using the Scherrer equation. The average size of the Pt_3Ti NPs for $x = 2$ was calculated to be the same, 2.5 nm. However, the average size of NPs for $x = 10$ or above cannot be determined solely from the *p*XRD data due to the weakness of the reflections. Indeed, the Pt_3Ti 200 reflection, observed as a shoulder at 46° for $x = 0$ and 2, becomes invisible for $x = 10$ and above.

Figure 2 presents bright field UHV-STEM images of free Pt_3Ti NPs (Figure 2a) and the SiO_2 -supported catalysts (Figure 2b–d). The free Pt_3Ti NPs, seen in Figure 2a as dark spots, agglomerate to form large clusters. Pt_3Ti NPs for $x = 2$ also form clusters adhering to the surface of SiO_2 supports which are seen in the figure as a light-colored material (Figure 2b). The clusters of NPs, however, become small and discrete with an increasing amount of SiO_2 (Figure 2c). Moreover, the distances between individual NPs increase with increasing SiO_2 amounts. Individual NPs can be clearly recognized and are finely dispersed on the surface of SiO_2 for $x = 50$ (Figure 2d).

Figure 3a shows the particle-size distributions of Pt_3Ti NPs for varying x , evaluated from the STEM images (Figure 2b–d). The particle size shows a normal distribution ranging from 1.9 to 3.1 nm and centered at 2.5 nm, regardless of x . The average particle size is calculated as 2.5 nm, which is consistent with the value obtained from the *p*XRD data. Figure 3b presents histograms of the interparticle distances, d , of the NPs for $x = 2, 10$, and 50. The histogram for $x = 2$ shows a peak at $d = 2.8 \text{ nm}$. The NPs form close-packing clusters, since this value is close to the average size of NPs, 2.5 nm. The histogram for $x = 10$ shows a peak at $d = 3.4 \text{ nm}$. The interparticle distance is elongated compared to $x = 2$, but there still remains a positional correlation among the NPs. Unlike either $x = 2$ or 10, no peak is recognized in the histogram for $x = 50$. For $x = 50$, the NPs are finely dispersed on SiO_2 without any positional correlations. It is worth noting that excessive SiO_2 strongly suppressed the agglomeration of NPs to achieve high dispersivity without any organic surfactants. These finely dispersed NPs on SiO_2 are ideal samples for single-particle compositional analysis as well as catalytic performance tests.

Single-particle EPMA was performed to determine the composition of individual NPs dispersed on SiO_2 . Figure 4 shows a comparison between the EPMA profiles of the SiO_2 support and

(41) Xu, Y.; Kameoka, S.; Kishida, K.; Demura, M.; Tsai, A. P.; Hirano, T. *Mater. Trans.* **2004**, *45*, 3177–3179.

(42) Chun, D. H.; Xu, Y.; Demura, M.; Kishida, K.; Oh, M. H.; Hirano, T.; Wee, D. M. *Catal. Lett.* **2006**, *106*, 71–75.

(43) Ellner, M. *J. Less-Common Metals* **1981**, *78*, 21–32.

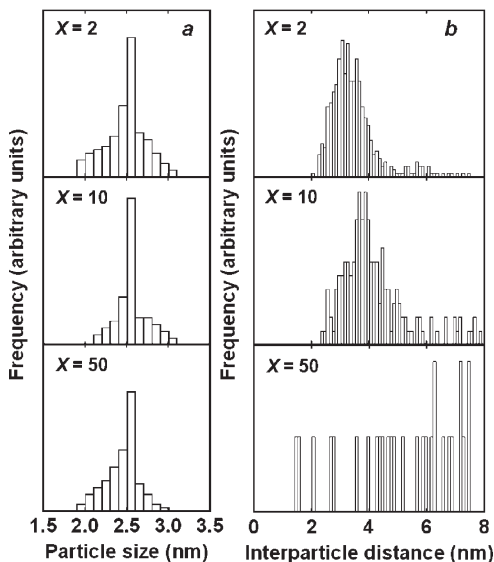


Figure 3. Histograms for the particle size (a) and interparticle distance (b) of Pt_3Ti NPs on SiO_2 with various amounts of SiO_2 relative to Pt precursors.

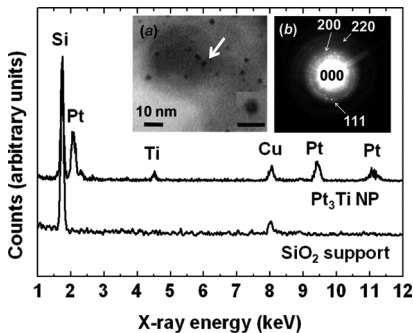


Figure 4. EPMA profiles for a Pt_3Ti NP and SiO_2 supports ($x = 50$). Inset shows (a) an EPMA profile was obtained from the Pt_3Ti NP as indicated by an arrow in the UHV-STEM image. A magnified individual NP is also shown in the inset; scale bar = 5 nm. (b) SAED pattern for as-synthesized Pt_3Ti NP at $x = 50$.

an individual NP for $x = 50$. The EPMA profile for the SiO_2 support shows two peaks at 1.7 and 8 keV, which are assigned to Si and the TEM grid material (Cu), respectively. In addition to these peaks, four more peaks are recognized in the EPMA profile for a single NP at 2.1, 4.6, 9.4, and 11.1 keV. The peaks at 2.1, 9.4, and 11.1 keV correspond to Pt. The weak peak at 4.6 keV is assigned to Ti. The mole ratio of Pt and Ti was calculated to be 73 ± 3 and 24 ± 4 , respectively. A large-area scan ($\approx 100 \mu\text{m}^2$) over hundreds of NPs resulted in the same mole ratio of Pt/Ti = $73 \pm 3:27 \pm 2$. The other NPs on SiO_2 , for $x = 2$ and 10, also had the same composition of Pt/Ti = 3:1 within experimental errors (Figure S1, Supporting Information). SAED on the SiO_2 -supported Pt_3Ti NPs for $x = 50$ showed strong {111}, {200} reflections and a weak {220} reflection of the $Fm\bar{3}m$ -type structure ($a = 0.39 \text{ nm}$). We conclude that the SiO_2 -supported catalyst for $x = 50$ was finely dispersed Pt_3Ti NPs with the stoichiometry of Pt/Ti = 3:1 and an atomically disordered $Fm\bar{3}m$ -type structure.

HX-PES measurements were performed on the SiO_2 -supported Pt_3Ti NPs to ensure the formation of the intermetallic Pt_3Ti phase. Carbon black as an inner standard was mixed with the SiO_2 -supported Pt_3Ti NPs for $x = 2$. Figure 5a shows HX-PES spectra in the C 1s region for pure carbon black and the carbon

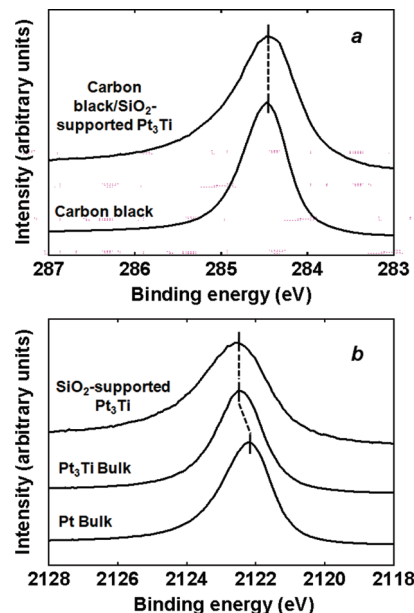


Figure 5. (a) HX-PES spectra for carbon black and for carbon black mixed with SiO_2 -supported Pt_3Ti NPs ($x = 2$), in the C 1s region. (b) HX-PES spectra for SiO_2 -supported Pt_3Ti NPs ($x = 2$) in the Pt 3d_{5/2} region. HX-PES spectra for the bulk surfaces of Pt_3Ti and Pt are presented as the reference.

black mixed with SiO_2 -supported Pt_3Ti NPs. Both of the profiles show peaks at the same binding energy of $284.5 \pm 0.05 \text{ eV}$, indicating that the SiO_2 -supported Pt_3Ti NPs were free from a charging effect. The Pt 3d_{5/2} emission, which has a much larger photoionization cross section than do Pt 4f emissions, was selected as a sensitive probe for the Pt_3Ti NPs that were highly diluted by SiO_2 supports and carbon black. Figure 5b shows HX-PES profiles in the Pt 3d_{5/2} region for SiO_2 -supported Pt_3Ti NPs and for bulk samples of Pt and Pt_3Ti . The Pt 3d_{5/2} emission from the bulk Pt surface has a binding energy of $2122.2 \pm 0.05 \text{ eV}$. The Pt 3d_{5/2} binding energy for the bulk Pt_3Ti surface, $2122.5 \pm 0.05 \text{ eV}$, shows a chemical shift by 0.3 eV relative to that for the Pt surface. The Pt 3d_{5/2} binding energy for the SiO_2 -supported Pt_3Ti NPs, $2122.5 \pm 0.05 \text{ eV}$, is consistent with the value for the Pt_3Ti surface. The Pt_3Ti NPs existed as an intermetallic Pt_3Ti phase on SiO_2 supports.

ICP-MS spectrometry was performed on the SiO_2 -supported Pt_3Ti NPs for $x = 50$ to determine the fraction of Pt relative to SiO_2 . The weight percentages of Pt and Si were estimated to be 0.47 and 45, respectively. These results showed that 0.5 wt % of Pt was contained in the SiO_2 -supported Pt_3Ti NPs for $x = 50$ (called $\text{Pt}_3\text{Ti}(0.5)/\text{SiO}_2$ hereafter). As a catalyst to compare to $\text{Pt}_3\text{Ti}(0.5)/\text{SiO}_2$, SiO_2 -supported pure Pt NPs with the same fraction of Pt (0.5 wt %) were synthesized by the method described in the Supporting Information (called Pt(0.5)/ SiO_2 hereafter). Pure Pt NPs were as highly dispersed on SiO_2 as were the SiO_2 -supported Pt_3Ti NPs and had the same average particle size, 2.5 nm (Figure S2, Supporting Information).

Figure 6 shows catalytic CO conversion at elevated temperatures over $\text{Pt}_3\text{Ti}(0.5)/\text{SiO}_2$ and Pt(0.5)/ SiO_2 . At room temperature, neither catalysts show any evidence of CO conversion. With increasing temperature, the CO conversion over Pt(0.5)/ SiO_2 becomes finite at an onset temperature of 200 °C and steeply grows, reaching full conversion at 325 °C. The trend of catalytic CO conversion over $\text{Pt}_3\text{Ti}(0.5)/\text{SiO}_2$ is similar, but a finite CO conversion is recognized at a lower onset temperature of 125 °C. The onset temperatures and CO conversion at given temperatures for these catalysts are listed in the first two rows of Table 1. Pt(0.5)/ SiO_2

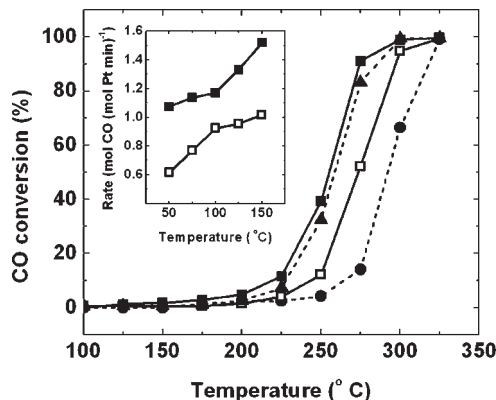


Figure 6. Temperature dependence of CO conversion over SiO₂-supported Pt₃Ti with 0.5 wt % Pt (Pt₃Ti(0.5)/SiO₂, ■) and SiO₂-supported pure Pt NPs containing 0.5 wt % Pt (Pt(0.5)/SiO₂, □). SiO₂-supported pure Pt NPs with different Pt fractions are plotted for comparison: 0.25 wt % (Pt(0.25)/SiO₂, ●) and 1.0 wt % (Pt(1.0)/SiO₂, ▲). Inset shows the temperature dependence of conversion rates for Pt₃Ti(0.5)/SiO₂ (■) and Pt(0.5)/SiO₂ (□).

Table 1. Onset Temperatures and CO Conversion at Different Temperatures for SiO₂-Supported Pt₃Ti NPs and SiO₂-Supported Pure Pt NPs Containing Different Pt Fractions^a

sample	onset temperature (°C)	CO conversion (%) at specific temperatures		
		125 °C	225 °C	300 °C
Pt ₃ Ti(0.5)/SiO ₂	125	1.3	11.5	99.1
Pt(0.5)/SiO ₂	200	0.6	3.9	94.7
Pt(0.25)/SiO ₂	225	0.0	2.4	66.4
Pt(1.0)/SiO ₂	200	0.6	7.3	99.2

^a The weight percentages of Pt in these catalysts are mentioned in parentheses.

showed a negligible CO conversion rate at the onset temperature of Pt₃Ti(0.5)/SiO₂, 125 °C. At 225 °C, 11.5% CO conversion was achieved by Pt₃Ti(0.5)/SiO₂, but only 3.9% was converted by Pt(0.5)/SiO₂. Full CO conversion was achieved at 300 °C by Pt₃Ti(0.5)/SiO₂, but for Pt(0.5)/SiO₂ this was done at 325 °C.

The inset of Figure 6 shows the CO conversion rates for Pt₃Ti(0.5)/SiO₂ and Pt(0.5)/SiO₂ at temperatures lower than 150 °C, which are normalized to the mole amounts of Pt contained in the catalysts (mol CO (mol Pt min)⁻¹). The CO conversion rate for Pt(0.5)/SiO₂ is consistent with the reported values (Pt NPs/SiO₂, particle size 3.3 nm).^{24,26} The CO conversion rate for Pt₃Ti(0.5)/SiO₂ is higher than double the CO conversion rate for Pt(0.5)/SiO₂ over the entire temperature range.

SiO₂-supported pure Pt NPs with 0.25 (called Pt(0.25)/SiO₂ hereafter) and 1.0 wt % of Pt (called Pt(1.0)/SiO₂ hereafter) were also synthesized using the same method as that for Pt(0.5)/SiO₂. Data for the catalytic CO conversion over SiO₂-supported pure Pt NPs with different Pt fractions are shown in Figure 6 and Table 1. The onset temperature for Pt(0.25)/SiO₂ was 225 °C, and only 66.4% CO conversion was achieved at 300 °C by this catalyst. The catalytic activity of Pt(0.25)/SiO₂ was lower than that of the Pt(0.5)/SiO₂. The onset temperature for Pt(1.0)/SiO₂ was 200 °C, and 7.3% CO conversion was achieved at 225 °C by this catalyst. It is worth noting that the onset temperature for Pt₃Ti(0.5)/SiO₂ was higher than that for Pt(1.0)/SiO₂ by 75 °C. In addition, the CO conversion rate for Pt(1.0)/SiO₂ was lower than that for the Pt₃Ti(0.5)/SiO₂ at any temperature. The sizes of the catalytic NPs were the same for SiO₂-supported Pt₃Ti NPs and SiO₂-supported pure Pt NPs. The support, SiO₂, likely does not affect the activity

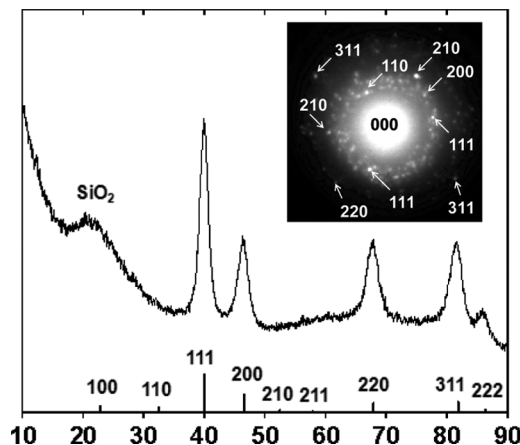


Figure 7. A pXRD profile and an SAED pattern (inset) for Pt₃Ti(0.5)/SiO₂ after catalytic oxidation of CO. Simulated pXRD peaks for the Cu₃Au-type structure ($Pm\bar{3}m$, $a = 0.39$ nm) are shown by solid lines.

of the catalytic NPs. We conclude that Pt₃Ti NPs possess a much higher catalytic activity toward CO oxidation than pure Pt NPs. The incorporation of Ti into Pt NPs promotes enhanced catalytic activity toward CO oxidation.

The mechanism of catalytic CO conversion reactions has been studied extensively by many research groups in terms of CO adsorption to catalyst surfaces.^{44–48} It has been shown that desorption of CO admolecules, which fully cover the catalyst surface at ambient temperature, triggers the catalytic CO conversion at a definite onset temperature (light-off phenomenon). The weaker the CO adsorption onto the catalyst surface, in general, the lower the onset temperature for CO conversion. It has been reported earlier that the adsorption energy of CO on bulk Pt₃Ti surface is 20% smaller than that on a pure bulk Pt surface.^{49–51} Therefore, the observed high catalytic activity of the Pt₃Ti NPs prepared in this work may be attributed to the weak adsorption of CO to the Pt₃Ti surface. This weak CO adsorption has been supported by the fact that Pt₃Ti NPs show much higher resistance against CO-poisoning than pure Pt NPs.²⁸

The crystal structure and chemical composition of Pt₃Ti(0.5)/SiO₂ were examined after the catalytic oxidation of CO up to 325 °C. A pXRD profile for Pt₃Ti(0.5)/SiO₂ after catalysis shows five peaks at 40°, 46°, 68°, 82°, and 86° corresponding to the primary reflections of the Pt₃Ti phase, 111, 200, 220, 311, and 222, respectively (Figure 7). SAED on this sample also showed the {111}, {200}, {220}, and {311} reflections of the Pt₃Ti phase. Interestingly, {210} and {110} satellite reflections of the atomically ordered Cu₃Au-type structure ($Pm\bar{3}m$, $a = 0.39$ nm), which were not detected by pXRD, were observed by SAED (inset of Figure 6). The binary phase of Pt_yTi_{1-y} adopts the Cu₃Au-type structure in a narrow range of $y = 0.75$ to 0.80.^{27,52} The presence of the satellite reflections of the Cu₃Au-type structure shows that Pt₃Ti NPs retained their stoichiometric composition after the catalysis.

(44) Berlowitz, P. J.; Peden, C. H. F.; Goodman, D. W. *J. Phys. Chem.* **1988**, *92*, 5213–5221.

(45) Engel, T.; Ertl, G. *Adv. Catal.* **1979**, *28*, 1–77.

(46) Jia, J. F.; Kondo, J. N.; Domen, K.; Tamaru, K. *J. Phys. Chem. B* **2001**, *105*, 3017–3022.

(47) Zhdanov, V. P.; Kasemo, B. *J. Chem. Phys.* **2001**, *114*, 5351–5357.

(48) Baraldi, A.; Gregoratti, L.; Comelli, G.; Dhanak, V. R.; Kiskinova, M.; Rosei, R. *Appl. Surf. Sci.* **1996**, *99*, 1–8.

(49) Bardi, U.; Somorjai, G. A.; Ross, P. N. *J. Catal.* **1984**, *85*, 272–276.

(50) Bardi, U.; Dahlgren, D.; Ross, P. N. *J. Catal.* **1986**, *100*, 196–209.

(51) Ross, P. N. *Electrochim. Acta* **1991**, *36*, 2053–2062.

(52) Murray, J. L. In *Phase Diagrams of Binary Titanium Alloys*; Murray, J. L., Ed.; ASM International: Metals Park, OH, 1987; pp 247–252.

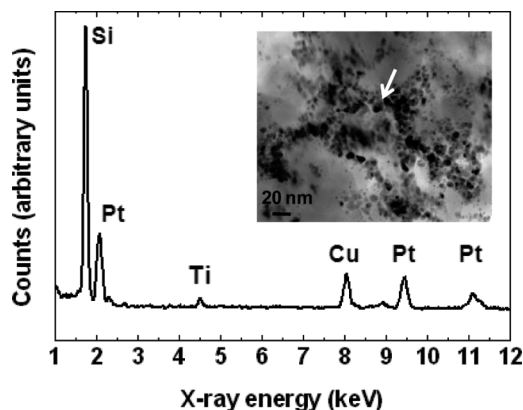


Figure 8. An EPMA profile and an UHV-STEM image (inset) for $\text{Pt}_3\text{Ti}(0.5)/\text{SiO}_2$ after catalytic oxidation of CO. The EPMA profile was obtained from the Pt_3Ti NP as indicated by an arrow in the UHV-STEM image.

The catalysis at elevated temperatures resulted in a development of atomic ordering in Pt_3Ti NPs from the atomically disordered FCC-type ($Fm\bar{3}m$) to the atomically ordered Cu_3Au -type ($Pm\bar{3}m$) structures. The atomically disordered Pt_3Ti NPs, which are synthesized at a much lower temperature than the melting point of bulk Pt_3Ti ($1900\ ^\circ\text{C}$),⁵² may be a metastable phase. The metastable, atomically disordered Pt_3Ti NPs are converted to stable, atomically ordered Pt_3Ti NPs by the heat provided through catalysis.

Figure 8 shows an EPMA profile and a UHV-STEM image of $\text{Pt}_3\text{Ti}(0.5)/\text{SiO}_2$ (inset) after catalytic oxidation of CO. Pt_3Ti NPs retained their stoichiometric composition ($\text{Pt}/\text{Ti} = 74 \pm 2.26 \pm 3$), as shown in the EPMA profile. The average particle size was calculated to be 4.8 nm from the UHV-STEM image. This value is larger than the particle size of Pt_3Ti NPs in as-synthesized $\text{Pt}_3\text{Ti}(0.5)/\text{SiO}_2$, 2.5 nm . The catalysis at elevated temperatures resulted in an increase in the particle size of Pt_3Ti NPs.

Conclusion

Pt_3Ti NPs with an average particle size of 2.5 nm were formed on SiO_2 supports by simultaneous reduction of organometallic Pt and Ti precursors in an oxygen- and moisture-free environment. Finely dispersed SiO_2 -supported Pt_3Ti NPs were obtained by adding a 50-fold excess amount of SiO_2 . A SiO_2 -supported Pt_3Ti NPs catalyst showed a higher catalytic activity toward CO oxidation than a SiO_2 -supported Pt NPs catalyst containing a 2-fold more amount of Pt. SiO_2 -supported Pt_3Ti NPs catalysts were not deactivated during catalytic oxidation of CO at elevated temperatures. Pt_3Ti NPs have promise as a catalytic center for the purification of automobile exhaust in terms of their high catalytic activity toward CO oxidation and relatively low content of precious metals. Future work should address a number of issues including the synthesis of atomically ordered Pt_3Ti NPs, preventing agglomeration at elevated temperatures. Catalytic activity toward the toxic nitrogen oxides (NO_x) also present in exhaust should be also tested.

Acknowledgment. We gratefully acknowledge Toyota Motor Corporation for financial support for this work. We thank Dr. Ito and Dr. Kobayashi of the Analytic Station of NIMS for ICP-MS measurements. The HX-PES measurements were performed under the approval of the NIMS Beamline Station (Proposal No. 2009B4608). The authors are grateful to HiSOR, Hiroshima University, and JAEA/SPring-8 for the development of HX-PES at BL15XU of SPring-8.

Supporting Information Available: Single-particle EPMA profiles for SiO_2 -supported Pt_3Ti NPs for $x = 2$ and 10 ; preparation of SiO_2 -supported Pt NPs as well as a bright field UHV-STEM image of the material. This material is available free of charge via the Internet at <http://pubs.acs.org>.

Pt₃Ti Nanoparticles: Fine Dispersion on SiO₂ Supports, Enhanced Catalytic CO Oxidation and Chemical Stability at Elevated Temperatures

Govindachetty Saravanan*, Hideki Abe*, Ya Xu, Nobuaki Sekido, Hirohito Hirata, Shin-ichi Matsumoto, Hideki Yoshikawa, and Yoko Yamabe-Mitarai

Supporting information

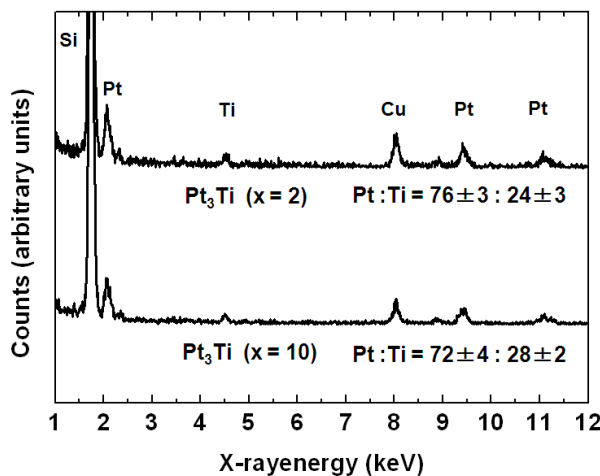


Figure S1. Single-particle EPMA profiles for SiO₂-supported Pt₃Ti NPs at 2- and 10-fold excess of SiO₂ relative to Pt precursors.

Preparation of SiO₂-supported Pt NPs

292.6 ml of aqueous H₂PtCl₆ (Tanaka Kikinzoku Co. Ltd.) solution (0.3 wt. %) was added slowly to 300 ml of 22.5 mmol aqueous polyvinylpyrrolidone (Nakaraitesk Co. Ltd.). After vigorous stirring, 150 ml of ethanol was added to the solution and then refluxed for 6 h at 100° C. The yellowish precursor solution turned black during reflux. The solution was then condensed by

distillation under reduced pressure to leave a black colored solution. The concentration of Pt in the Pt NPs solution was determined to be 0.62 wt. % by ICP analysis.

0.25, 0.50, and 1.0 wt. % of Pt NPs relative to the amount of SiO₂ were added to 20 g of SiO₂ suspension in 200 ml of ion-exchange water. After removal of water, the residue was dried for 2 h at 120° C. The final product was crushed and then annealed at 450° C in air for 2 hours to yield the desired catalysts.

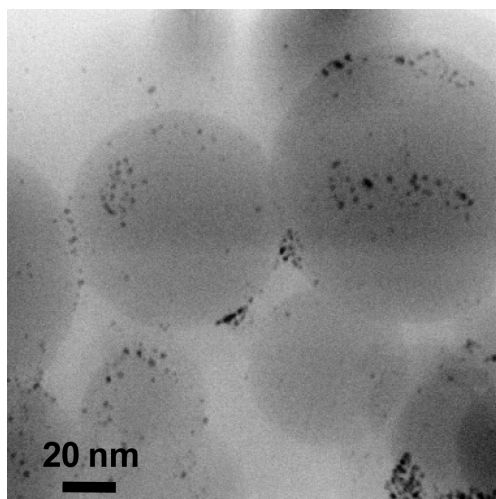


Figure S2. Bright field UHV-STEM image of SiO₂-supported Pt NPs with 0.5 wt. % of Pt.

Open-Mouthed Metallic Microcapsules: Exploring Performance Improvements at Agglomeration-Free Interiors

Saikat Mandal,[†] Marappan Sathish,[‡] Govindachetty Saravanan,[¶] K. K. R. Datta,^{†,§} Qingmin Ji,[†] Jonathan P. Hill,^{†,§} Hideki Abe,[¶] Itaru Honma,[‡] and Katsuhiko Ariga^{*,†,§}

WPI Center for Materials Nanoarchitectonics (MANA), National Institute For Materials Science (NIMS), 1-1 Namiki, Tsukuba 305-0044, Japan, JST, CREST, 1-1 Namiki, Tsukuba 305-0044, Japan, Advanced Electronic Materials Center, NIMS, 1-2-1 Sengen, Tsukuba 305-0047, Japan, Institute of Multidisciplinary Research for Advanced Materials, Tohoku University, Sendai 980-8577, Japan, and Jawaharlal Nehru Centre for Advanced Scientific Research (JNCASR), Bengaluru-560064, India

Received August 22, 2010; E-mail: ARIGA.Katsuhiko@nims.go.jp

Abstract: Although artificial capsule structures have been thoroughly investigated, functionality at the surfaces of their interiors has been surprisingly overlooked. In order to exploit this aspect of capsular structure, we here report the breakthrough fabrication of metallic (platinum) microcapsules with sufficient accessibility and electroactivity at both interior and exterior surfaces (open-mouthed platinum microcapsules), and also we demonstrate improvements in electrochemical and catalytic functions to emphasize the practical importance of our concept. The open-mouthed platinum microcapsules were prepared by template synthesis using polystyrene spheres, where surface-fused crystalline nanoparticles formed a capsule shell. Subsequent removal of the polystyrene spheres induced formation of mouth-like openings. The open-mouthed platinum microcapsules exhibit a substantial increase of their electrode capability for methanol oxidation and catalytic activities for carbon monoxide (CO) oxidation. Notably, activity loss during CO oxidation due to undesirable particle agglomeration can be drastically suppressed using the open-mouthed microcapsules.

As exemplified by living cells, capsular structures lead to sophisticated functions which depend on differentiation between the interior and exterior environments as well as specific interactions occurring at the capsule shell interface. Organic mimics of cells including lipid vesicles¹ and polymer capsules² have been widely investigated, and hollow spheres composed of hybrids and inorganic materials including silica,³ carbon,⁴ quantum dots,⁵ and metal⁶ have been also developed in order to compensate for the relative mechanical weakness of the organic counterparts. Some of these exhibit excellent properties suitable for drug delivery, sensing, and reactor applications.⁷ Interestingly, most of these functions rely only on permeation control through the capsule membrane and/or specific interactions at their outer surfaces. Functionalities of inner surfaces of artificial capsular structures have not been fully explored except for some pioneering examples⁸ although biological cells effectively use inner surface functions as can be seen in signal transduction and photoenergy conversion. Considered simply, effective use of capsular inner surfaces could double the available functionality relative to traditional systems, which rely only on use of exterior surfaces. Additionally, the interior surface environment is not susceptible to particle agglomeration.

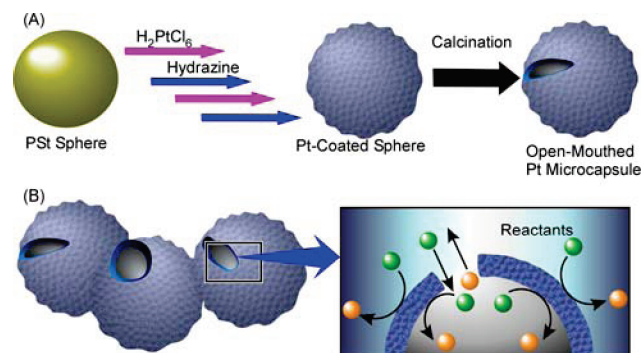


Figure 1. (A) Synthetic scheme for open-mouthed Pt microcapsules and (B) their usage for inside/outside active reactor.

In order to develop this unexplored breakthrough concept, we here report fabrication of metallic (platinum) microcapsules with sufficient accessibility to their interiors and with a variety of functions at both interior and exterior surfaces, which we refer to as open-mouthed platinum microcapsules, and we also demonstrate improvements in the electrochemical and catalytic functions emphasizing the practical importance of our concept. So far, different platinum nanomaterials⁹ including nanosheets and nanoparticles have been used in several applications including fuel cells and catalysts in automobile technologies because of their high surface areas, which are however often subject to deterioration caused by their agglomeration. On the contrary, interior surfaces of hollow structures would be *completely free from* the surface area loss associated with particle agglomeration. In a clear demonstration of the advantages of our concept, the open-mouthed platinum microcapsules fabricated in this research showed a significant increase (substantially more than a 2-fold improvement) in their electrochemical and catalytic capabilities. In the latter, the open-mouthed platinum microcapsules exhibited a particularly enhanced activity in carbon monoxide (CO) oxidation at a rather low reaction temperature, thus providing a potential ideal solution for the relevant automobile technologies.

As illustrated in Figure 1, the platinum-coated polystyrene (PSt) latex spheres were first prepared by suspension of the template PSt spheres in an ethanolic solution of H_2PtCl_6 ($\text{PSt}/\text{H}_2\text{PtCl}_6 = 1:3$ w/w) at room temperature, followed by drying at 60°C for 12 h with subsequent reduction using hydrazine solution.¹⁰ The black platinum-coated PSt spheres obtained were calcined by heating to 500°C with a heating rate of 5°C min^{-1} and then maintained at 500°C for 6 h, resulting in platinum microcapsules as a black powder,

[†] MANA, NIMS

[‡] Tohoku Univ.

[¶] Advanced Electronic Materials Center, NIMS

[§] JST, CREST.

^{*} JNCASR.

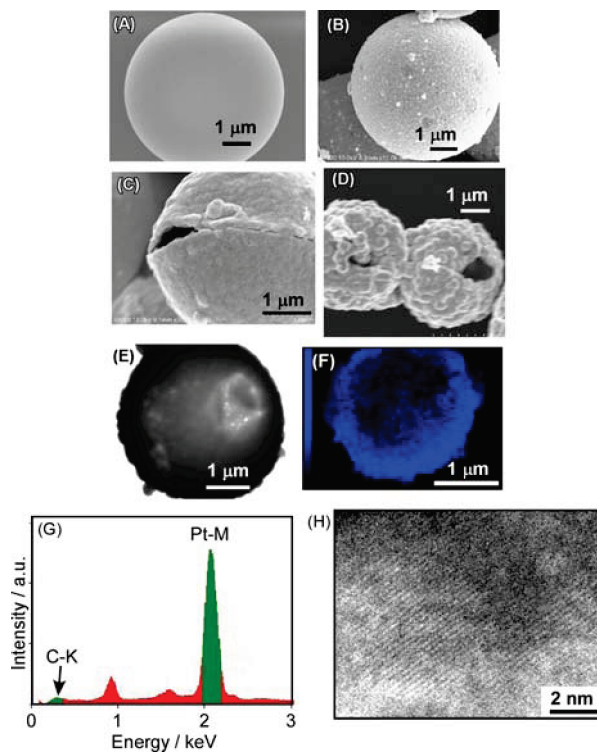


Figure 2. Morphologies: (A) FE-SEM image of PSt template; (B) FE-SEM image of Pt-coated sphere; (C and D) open-mouthed Pt microcapsule; (E) TEM image of the open-mouthed Pt microcapsule; (F) Pt distribution in EDS elemental mapping of the open-mouthed Pt microcapsule; (G) EDS spectrum of the open-mouthed Pt microcapsule; (H) high resolution TEM of {200} plane of the open-mouthed Pt microcapsule.

which were finally washed with distilled water and absolute ethanol prior to further characterization.

Field emission scanning electron microscopy (FE-SEM) images revealed that spherical morphologies with several μm diameters were maintained before (Figure 2A) and after Pt coating (Figure 2B). While the surfaces of the original PSt spheres are very smooth, coating with Pt leads to an increase in surface roughness, due to the presence of many nanoparticles with diameters ranging from 20 to 60 nm. Calcination to remove the PSt template induced interesting changes in their morphologies; i.e., the spherical shape was maintained but mouth-like openings could be observed in each sphere (see Figure 2C and 2D). Pt particles do not fully melt under the calcination conditions applied but may be surface-fused through low-temperature welding as has been reported for other metallic nanoparticles.¹¹ Fusion between Pt particles leads to shells free of small pores in contrast to organic capsules and mesoporous capsules, and this probably results in formation of the mouth-like openings caused by escaping residues of the decomposing template. In fact, most of the capsule objects have one or two mouth-like structures. The thickness of the open mouth sphere is 40 to 50 nm by SEM observation. The thickness can be controlled by the ratio between PSt and H_2PtCl_6 and the number of the coating cycles. The FT-IR spectrum¹⁰ of an uncalcined sample shows clear peaks assignable to PSt templates at 696, 756, 1068, and 3025 cm^{-1} due to the phenyl group and peaks at 2848 and 2920 cm^{-1} due to the C–H vibrations. All of these peaks disappeared after calcination, indicating complete removal of the PSt template.

Further investigation by transmission electron microscopy (TEM) confirms the hierarchic structure of the hollow capsules composed of Pt nanoparticles (Figure 2E). Elemental mapping (Figure 2F) by energy dispersive X-ray spectroscopy (EDS) indicates homo-

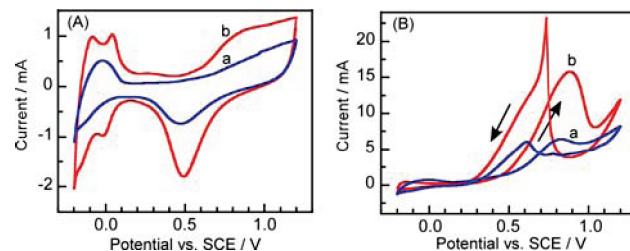


Figure 3. Cyclic voltammograms in (A) aqueous H_2SO_4 solution (0.5 M) and (B) H_2SO_4 (0.5 M) solution containing methanol (1 M) at scan rate of 25 mV s^{-1} at room temperature, as measured using a glassy carbon electrode coated with a (a) Pt-coated sphere and an (b) open-mouthed Pt microcapsule.

geneous distributions of platinum in the open-mouthed microcapsules, although only a small amount of carbon could be detected (see EDS spectrum, Figure 2G). High resolution TEM (HRTEM) imaging (Figure 2H) revealed a regular {200} lattice plane with a *d*-spacing of 0.196 nm. In a powder X-ray diffraction (XRD) pattern,¹⁰ all peaks could be perfectly indexed to the fcc structure of crystalline Pt.¹² The high definition of the XRD peaks attests to the high purity and crystallinity of Pt in the capsule.

Cyclic voltammetric curves of electrodes coated with either uncalcined spheres or the open-mouthed capsules in 0.5 M aqueous H_2SO_4 solution showed two broad peaks in the potential range from -0.20 to 1.10 V (Figure 3A). These cathodic and anodic current densities at the same Pt content in both the hydrogen adsorption/desorption and oxide formation/reduction regions of the open-mouthed capsules are much larger than those of uncalcined spheres (ca. 2.5-fold increase). This clearly indicates a larger electroactive surface area¹³ and easy accessibility to the Pt capsular surfaces due to the open-mouthed morphology. Their performance was further investigated by applying them in an electrochemical reaction in an aqueous solution of 0.5 M H_2SO_4 containing 1 M methanol (Figure 3B). Both the Pt hollow capsules and uncalcined Pt spheres exhibited catalytic activity for the electro-oxidation of methanol. Again, a much higher current density for methanol electro-oxidation was observed for the open-mouthed capsules relative to the uncalcined Pt spheres. The enhanced electroactivity of open-mouthed capsules clearly confirms the advantages of using the interior surfaces of the open-mouthed capsule structures in electrochemical applications.

The catalytic performance of the open-mouthed Pt microcapsules in the gas phase was investigated in the oxidation of carbon monoxide (CO) by oxygen (O_2). Time courses of CO conversion (Figure 4), which are normalized for the net amount of Pt, indicate that Pt on the polymer sphere showed twice the CO oxidation rate at any duration time compared to a standard catalyst (pure Pt powder, average particle diameter: $6\text{ }\mu\text{m}$) owing to the greater surface roughness and/or the smaller particle size in the former case. Surprisingly, the open-mouthed Pt capsules exhibited significantly superior catalytic activities to both the Pt on the polymer spheres and Pt powder. Enhancement of the catalytic activity in the open-mouthed Pt capsules relative to the Pt-coated spheres reaches ca. 5-fold, which is much greater than the difference between their apparent surface areas (<2). In addition, the open-mouthed Pt capsules showed significant CO oxidation catalytic activity at an onset temperature (temperature at which 1% CO was converted) of $125\text{ }^\circ\text{C}$, which is much lower than the values reported previously for bulk Pt or Pt-supported catalysts ($>200\text{ }^\circ\text{C}$).¹⁴ It is known that one of the biggest challenges for exhaust catalysts is minimization of thermal agglomeration of the catalytic centers at elevated temperatures, which results in significant degradation of

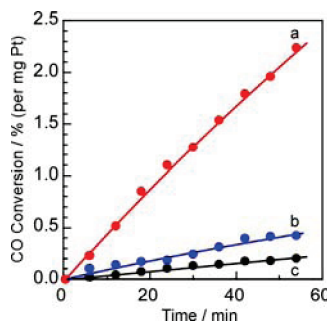


Figure 4. Time course conversion of CO oxidation at 125 °C normalized by Pt content: (a) open-mouth Pt microcapsule; (b) Pt-coated sphere; (c) Pt powder.

the apparent activity.¹⁵ The interior surface of the open-mouthing capsules is most likely free from thermal agglomeration since it is isolated from the other capsules by the exterior surface. The very high CO oxidation activity of the open-mouthing capsules can be ascribed to the highly active, agglomeration-free interior surface. The open-mouthing Pt capsules have great potential as an exhaust catalyst, in terms of the high CO removal activity and the superior tolerance to thermal agglomeration of the active sites. We should emphasize again the following fact. The activity ratio of the open-mouthing capsule to Pt-coated sphere remains ca. 2.5-fold in application at room temperature (Figure 3), but it reached up to ca. 5-fold for functions at elevated temperature (Figure 4). It means that the open-mouthing structure is much more advantageous in applications at higher temperature where thermal agglomeration of particles becomes a serious problem.

This research reports a strategy for formation of open-mouthing metallic microcapsules where the advantages of using the interior surface of microcapsules in electrochemical and gaseous catalytic applications are clearly demonstrated. Because of its simplicity and ease of implementation, the concept of effective use of capsule interior surfaces can be extended to general applications including sensors, functional electrodes, and reactors. In addition, use of both interior and exterior surfaces of thin capsule shells could also lead to more effective use of scarce natural resources, in this case the precious element platinum. As demonstrated here, the huge increase of CO oxidation activity by the open-mouthing Pt capsules suggests especially that this concept may provide ideal solutions to demands in practical applications such as exhaust catalysts for automobile technologies. As known in actual uses, the apparent activity of the practical catalysts is strongly enhanced by alloying Pt nanoparticles with Pd and/or Rh. Our synthetic strategy for capsular catalysts would be widely applicable to the alloys of Pt, Pd, and/or Rh to realize much superior activity in future than that of the pure Pt material at present.

Acknowledgment. This work was in part supported by World Premier International Research Center (WPI) Initiative on Materials Nanoarchitectonics, MEXT, Japan and JST, CREST. S.M. thanks Japan Society for the Promotion of Science (JSPS) for a research fellowship. K.K.R.D. thanks NIMS for an International Joint Graduate School (IJGS) Fellowship and Prof. C. N. R. Rao for his kind support and encouragement.

Supporting Information Available: Synthetic details and additional characterization data. This material is available free of charge via the Internet at <http://pubs.acs.org>.

References

- (a) Kunitake, T.; Okahata, Y. *J. Am. Chem. Soc.* **1977**, *99*, 3860–3861. (b) Steinberg-Yfrach, G.; Rigaud, J.-L.; Durantin, E. N.; Moore, A. L.; Gust, D.; Moore, T. A. *Nature* **1998**, *392*, 479–482. (c) Sakai, T.; Mukawa, T.; Tsuchiya, K.; Sakai, H.; Abe, M. *J. Nanosci. Nanotechnol.* **2009**, *9*, 461–466.
- (a) Caruso, F.; Caruso, R. A.; Möhwald, H. *Science* **1998**, *282*, 1111–1114. (b) Caruso, F. *Adv. Mater.* **2001**, *13*, 11–22. (c) Schneider, G. F.; Decher, G. *Nano Lett.* **2008**, *8*, 3598–3604. (d) Wang, Y.; Angelatos, A. S.; Caruso, F. *Chem. Mater.* **2008**, *30*, 848–858.
- (a) Katagiri, K.; Ariga, K.; Kikuchi, J. *Chem. Lett.* **1999**, 661–662. (b) Caruso, R. A.; Susha, A.; Caruso, F. *Chem. Mater.* **2001**, *13*, 400–409. (c) Katagiri, K.; Hamasaki, R.; Ariga, K.; Kikuchi, J. *J. Am. Chem. Soc.* **2002**, *124*, 7892–7893. (d) Katagiri, K.; Hamasaki, R.; Ariga, K.; Kikuchi, J. *Langmuir* **2002**, *18*, 6709–6711. (e) Li, W.; Sha, X.; Dong, W.; Wang, Z. *Chem. Commun.* **2002**, 2434–2435. (f) Katagiri, K.; Hashizume, M.; Ariga, K.; Terashima, T.; Kikuchi, J. *Chem.—Eur. J.* **2007**, *13*, 5272–5281. (g) Ji, Q.; Miyahara, M.; Hill, J. P.; Acharya, S.; Vinu, A.; Yoon, S. B.; Yu, J.-S.; Sakamoto, K.; Ariga, K. *J. Am. Chem. Soc.* **2008**, *130*, 2376–2377. (h) Ji, Q.; Acharya, S.; Hill, J. P.; Vinu, A.; Yoon, S. B.; Yu, J.-S.; Sakamoto, K.; Ariga, K. *Adv. Funct. Mater.* **2009**, *19*, 1792–1799.
- (a) Yoon, S. B.; Sohn, K.; Kim, J. Y.; Shin, C.-H.; Yu, J.-S.; Hyeon, T. *Adv. Mater.* **2002**, *14*, 19–21. (b) Ji, Q.; Yoon, S. B.; Hill, J. P.; Vinu, A.; Yu, J.-S.; Ariga, K. *J. Am. Chem. Soc.* **2009**, *131*, 4220–4221.
- Harrison, R. G.; Washburn, A. L.; Pickett, A. T.; Call, D. M. *J. Mater. Chem.* **2008**, *18*, 3718–3722.
- (a) Kim, S.-W.; Kim, M.; Lee, W. Y.; Hyeon, T. *J. Am. Chem. Soc.* **2002**, *124*, 7642–7643. (b) Sun, Y.; Mayers, B.; Xia, Y. *Adv. Mater.* **2003**, *15*, 641–646. (c) Song, Y.; Garcia, R. M.; Dorin, R. M.; Wang, H.; Qiu, Y.; Shelnutt, J. A. *Angew. Chem., Int. Ed.* **2006**, *45*, 8126–8130. (d) Song, Y.-Y.; Li, Y.; Xia, X.-H. *Electrochim. Commun.* **2007**, *9*, 201–205. (e) Alayoglu, S.; Nilekar, A. U.; Mavrikakis, M.; Eichhorn, B. *Nat. Mater.* **2008**, *7*, 333–338. (f) Garcia, R. M.; Song, Y.; Dorin, R. M.; Wang, H.; Li, P.; Qiu, Y.; van Swol, F.; Shelnutt, J. A. *Chem. Commun.* **2008**, 2535–2537.
- (a) Lvov, Y.; Antipov, A. A.; Mamedov, A.; Möhwald, H.; Sukhorukov, G. B. *Nano Lett.* **2001**, *1*, 125–128. (b) Otsuka, H.; Nagasaki, Y.; Kataoka, K. *Adv. Drug. Delivery Rev.* **2003**, *55*, 403–419. (c) Johnston, A. P. R.; Cortez, C.; Angelatos, A. S.; Caruso, F. *Curr. Opin. Colloid Interface Sci.* **2006**, *11*, 203–209. (d) Nayak, S. R.; McShane, M. J. *J. Biomed. Nanotechnol.* **2007**, *3*, 170–177. (e) Ariga, K.; Hill, J. P.; Lee, M. V.; Vinu, A.; Charvet, R.; Acharya, S. *Sci. Technol. Adv. Mater.* **2008**, *9*, 014109. (f) Ariga, K.; Hill, J. P.; Ji, Q. *Macromol. Biosci.* **2008**, *8*, 981–990. Agarwal, A.; Lvov, Y.; Sawant, R.; Torchilin, V. *J. Controlled Release* **2008**, *128*, 255–260. (g) Ariga, K.; Ji, Q.; Hill, J. P.; Kawazoe, N.; Chen, G. *Expert Opin. Biol. Ther.* **2009**, *9*, 307–320.
- (a) Duan, L.; He, Q.; Wang, K.; Yan, X.; Cui, Y.; Möhwald, H.; Li, J. *Angew. Chem., Int. Ed.* **2007**, *46*, 6996–7000. (b) He, Q.; Duan, L.; Qi, W.; Wang, K.; Cui, Y.; Yan, X.; Li, J. *Adv. Mater.* **2008**, *20*, 2933–2937.
- (a) Joo, S. H.; Choi, S. J.; Oh, I.; Kwak, J.; Liu, Z.; Terasaki, O.; Ryoo, R. *Nature* **2001**, *412*, 169–172. (b) Wang, C.; Daimon, H.; Lee, Y.; Kim, J.; Sun, S. *J. Am. Chem. Soc.* **2007**, *129*, 6974–6975. (c) Wang, C.; Daimon, H.; Onodera, T.; Koda, T.; Sun, S. *Angew. Chem., Int. Ed.* **2008**, *47*, 3588–3591. (d) Kijima, T.; Nagatomo, Y.; Takemoto, H.; Uota, M.; Fujikawa, D.; Sekiya, Y.; Kishishita, T.; Shimoda, M.; Yoshimura, T.; Kawasaki, H.; Sakai, G. *Adv. Funct. Mater.* **2009**, *19*, 545–553.
- See Supporting Information.
- (a) Ferguson, G.; Chaudhury, M. K.; Sigal, G. B.; Whitesides, G. M. *Science* **1991**, *253*, 776–778. (b) Mandal, S.; Shundo, A.; Acharya, S.; Hill, J. P.; Ji, Q.; Ariga, K. *Chem.—Asian J.* **2009**, *4*, 1055–1058.
- Mandal, S.; Selvakannan, P. R.; Roy, D.; Chaudhari, R. V.; Sastry, M. *Chem. Commun.* **2002**, *2002*, 3003–3003.
- The similar possibility was suggested for a Co–Pt sphere. See: Chen, G.; Dingguo, X.; Nie, Z.; Wang, Z.; Wang, L.; Zhang, L.; Zhang, J. *Chem. Mater.* **2007**, *19*, 1840–1844.
- (a) Saravanan, G.; Abe, H.; Xu, Y.; Sekido, N.; Hirata, H.; Matsumoto, S.; Yoshikawa, H.; Yamabe-Mitarai, Y. *Langmuir* **2010**, *26*, 11446–11451. (b) Daniel, C.; Clarté, M.-O.; Teh, S.-P.; Thionon, O.; Provendier, H.; Van Veen, A. C.; Beccard, B. J.; Schuurman, Y.; Mirodatos, C. *J. Catal.* **2010**, *272*, 55–64.
- Nishihata, Y.; Mizuki, J.; Akao, T.; Tanaka, H.; Uenishi, M.; Kimura, M.; Okamoto, T.; Hamada, N. *Nature* **2002**, *418*, 164–167.

JA107589M

Supporting information

Open-Mouthed Metallic Microcapsules: Exploring Performance Improvements at Agglomeration-Free Interiors

Saikat Mandal, Marappan Sathish, Govindachetty Saravanan, Kasibhatta K. R. Datta,
Qingmin Ji, Jonathan P. Hill, Hideki Abe, Itaru Honma, and Katsuhiko Ariga

WPI Center for Materials Nanoarchitectonics (MANA), National Institute For Materials Science (NIMS), 1-1 Namiki, Tsukuba 305-0044, Japan, JST, CREST, 1-1 Namiki, Tsukuba 305-0044, Japan, Advanced Electronic Materials Center, NIMS, 1-2-1 Sengen, Tsukuba 305-0047, Japan, Institute of Multidisciplinary Research for Advanced Materials, Tohoku University, Sendai 980-8577, Japan, and Jawaharlal Nehru Centre for Advanced Scientific Research (JNCASR), Bengaluru-560064, India

1. Detailed Experimental Procedure

1-1. Materials: Polystyrene latex spheres (3-5 μm), 5 wt% Nafion solution and chloroplatinic acid hydrate ($\text{H}_2\text{PtCl}_6 \cdot x\text{H}_2\text{O}$) were purchased from Sigma-Aldrich, Japan and used as received. Hydrazine hydrate, Ethanol, Methanol and H_2SO_4 were purchased from Wako, Japan and used as received. Highly pure samples (CO gas in 99.95% from Taiyo-Nissan and Pt powder in 99.9818% from Furuya Kinzoku) were used for CO oxidation reaction.

1-2. Synthesis of open-mouthed platinum microcapsule: In a typical experiment, the polystyrene (PSt) latex spheres were added into the ethanolic solution (10 ml) of H_2PtCl_6 ($\text{PSt}:\text{H}_2\text{PtCl}_6 = 1:3$ w/w) under sonication over 20 min to form a homogeneous suspension and followed by stirring at room temperature for 24 h, then the temperature was raised to 60 °C to evaporate the excess ethanol solution and a dry powder obtained. The powder was dried at 60°C for 12 h and re-dispersed into 10 ml of ethanol, then reduced by adding 2 ml of hydrazine solution (0.1 M). Then, the reaction mixture was

turned black and indicated the formation of platinum nanoparticles. After completion of the color change, the final black solid products were centrifuged and washed with distilled water and absolute ethanol several times, and then dried at 40° C under a vacuum for 4 h. The above processes were repeated for 4 times to get the complete coverage of PSt spheres by Pt nanoparticles. In order to prepare hollow capsule structures, the Pt-coated PSt spheres were calcined at 500 °C with a ramping rate of 5 °C min⁻¹ and then maintained at 500 °C for 6 h. A black residual powder was collected and then washed with distilled water and absolute ethanol for further characterization.

1-3. Characterization: Powder X-ray diffraction (XRD) patterns of the samples were recorded on a Rigaku RINT 2000 instrument consisting of a rotating anode generator with a copper target (Cu K α - radiation) operating at 45 kV and 40mA. The FT-IR spectra were recorded on a Nicolet 670 Fourier transform infrared spectrometer with a MCT/A detector, operating with 100 scans at 25 °C. Field-emission scanning electron microscopy (FE-SEM) observations of the samples were carried out using a Hitachi S-4800 at an accelerating voltage of 10 kV. Transmission electron microscopy (TEM) measurements were performed on a JEOL JEM 2000 instrument operated at an accelerating voltage of 200 kV. High resolution transmission electron microscopy (HR-TEM) and elemental mapping measurements were performed on a JEOL JEM 2100F instrument operated at an accelerating voltage of 200 kV. Thermogravimetric (TG) experiments (SII, TG/DTA 6300) were carried out in air atmosphere from room temperature to 800°C at a heating rate of 10°C/min.

1-4. Electrochemical analysis: Cyclic voltammograms were recorded on an ALS/H CH Instrument Electrochemical Analyzer, Model 612B. The electrochemical oxidation of methanol was carried out in 0.5 M aqueous H₂SO₄ solution containing 1M methanol at room temperature. The reference and counter electrodes used in the present work were saturated Ag/AgCl and Pt wire, respectively. The working electrode (glassy carbon electrode) was prepared as follows; 5 mg of open-mouthed Pt microcapsules was dispersed in 0.1 ml distilled water and sonicated for a few minutes to obtain a homogeneous dispersion. From the dispersion 20 μ l was placed on the glassy carbon

surface and dried in air followed by the addition of 5 μ l of 5% Nafion solution as binder. Before recording the cyclic voltammograms, the electrode was soaked in the test solution for 10 min to allow the system to reach a stable state. The potential scan was started at the open circuit potential and was stepped up to -0.20 V before proceeding to 1.2 V and then returned to -0.20 V. The same measurement was performed for the uncalcined samples (Pt-coated PSt sphere) at the same Pt content. These experiments were conducted at room temperature.

1-5. CO Oxidation: Pt samples (50 mg) (Pt powder, Pt-coated sphere, or open-mouthed Pt capsule) were kept in the U-shaped sample tube and allowed under vacuum at 125° C for overnight to remove moisture. Prior to the CO oxidation catalysis, the samples were pre-treated with H₂ (50 kPa) at 125 °C for 2 h (Pt surface activation). Gas mixture of CO and O₂ in 2:1 mole ratio (total pressure 10 kPa) was passed over the sample at constant temperature, 125 °C to study the oxidation catalysis of CO. Gas (3 mL) from the circulation line was examined using a Gas Chromatograph (Shimadzu GC-8A) every 6 min. CO oxidation catalytic activity of the sample was examined by the ratio of concentration of CO₂ (due to oxidation of CO on Pt-polymer beads/Pt hollow spheres) and CO. The Pt loading weight of Pt-coated sample was determined from TGA/DTA measurements (SII, TG/DTA 6300). Five separate data runs collected under identical condition were averaged and standard deviation of each point was calculated as +/- 0.035 (%/mg of Pt). The observed data were normalized by using Pt loading weight.

2. Additional Characterization Data

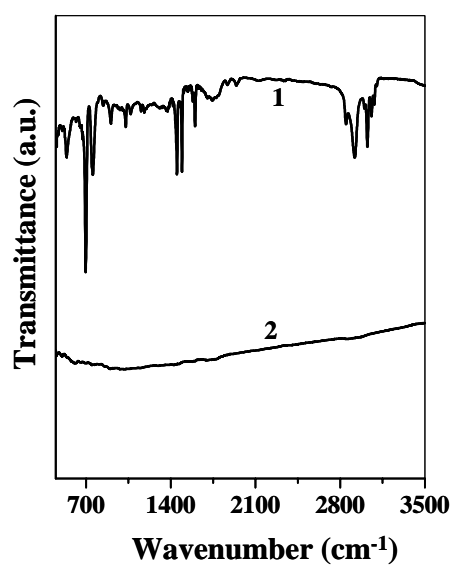


Figure S1. FTIR spectra of the uncalcined sample (Pt-coated PSt sphere) (curve 1) and open-mouthed Pt microcapsule (curve 2).

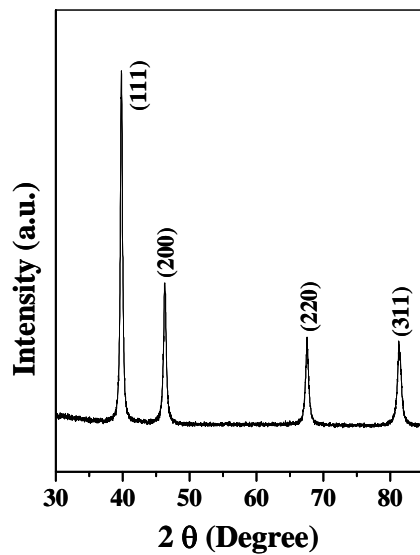


Figure S2. A XRD pattern recorded for the open-mouthed Pt microcapsule.

Magnetic Field Control of Electron Tunneling Pathways in the Monolayer of (Ferrocenylmethyl)dodecyldimethylammonium Bromide on a Gold Electrode

Govindachetty Saravanan and Sumio Ozeki*

Department of Chemistry, Faculty of Science, Shinshu University, 3-1-1 Asahi, Matsumoto, Nagano 390-8621, Japan

Received: August 19, 2007; In Final Form: October 18, 2007

The electron-tunneling reaction in the monolayer of (ferrocenylmethyl)dodecyldimethylammonium bromide (FDAA) and the mixed monolayer of FDAA and 11-mercaptopoundecanoic acid (MUA) on gold electrodes was affected by homogeneous, steady magnetic fields perpendicular to the monolayer membrane. Both the current and peak-to-peak separation potential of the ferrocenyl/ferricinium redox couple in cyclic voltammograms increased with increasing magnetic field intensity. The electron tunneling reaction of FDAA depended not on the barrier thickness of the monolayer but on the electron tunneling pathways. The increase in the tilt angle of hydrocarbon chains of FDAA and MUA due to cooperative magnetic orientation may bring about change of the electron tunneling pathway of the through-bond to through-space. With increasing magnetic fields, the increase in the path length and interchain superexchange hops led to an increase in the peak-to-peak separation potential and tunneling current. The positive shift of the formal potential due to magnetic fields is ascribed to promotion of hydration around the redox couple.

Introduction

It is well-known that a self-assembled monolayer (SAM) forms highly insulating barriers on the surface of metal electrodes.^{1–4} The experimental electron-transfer rate constant k_{et} depends exponentially on the length l_c of an alkane chain or the number of methylene groups n . The classical Marcus theory includes the term of the electronic coupling between the redox species and the electrode, which is the dominant distance dependent term for the large distance.⁵ The electronic coupling through an alkane monolayer membrane also depends exponentially on the physical thickness d of the membrane along the surface normal. The d dependence corresponds to the observed exponential n dependence of the electron-transfer rate constant. However, the observation deviated from the exponential dependences on distance for short alkanethiol SAMs¹ and nature of the electron tunneling path which includes an ether link and an amide moiety forming hydrogen bond networks² and on l_c or n and d for oriented membrane having largely tilted chains.³ These findings suggest that superexchange coupling between alkane chains should be taken into accounts in understanding the distance dependence of the tunneling reaction. A few experiments showed that interchain coupling played an important role in the electron-tunneling reactions of alkanes having covalently linked and membrane-buried redox couples,⁴ which were interpreted successfully for the distance dependence of k_{et} by interchain through-space coupling as well as through-bond pathways.³ The model in which the electron tunneling proceeds by both through-bond and through-space accounted for the pathway dependence of electron tunneling through alkanethiol SAMs on a Hg droplet and different alkanethiol-

coated Au and InP electrodes, in which the tilt angle of the chains could systematically vary.

Steady magnetic fields have been widely used to control structures and functions of molecular assemblies and membranes such as lipid bimolecular membranes, liposomes, and organogels.^{6–8} Molecular assemblies comprising magnetically anisotropic alkyl chains will become orientated in a steady magnetic field H . The magnetic orientation energy E_r of diamagnetic chain molecules having the magnetic anisotropy $\Delta\chi$ is given by the following equation:

$$E_r = -(N_m \Delta\chi H / 2) \cos^2 \varphi \quad (1)$$

where φ is the angle between a magnetic field and the molecular axis and N_m is the number of molecules. Although the magnetic energy of a diamagnetic chain molecule is not enough to orient under a magnetic field, a membrane comprising large number of molecules may orient cooperatively under a high magnetic field. The average orientation angle is determined by the probability $p(\varphi) = p(0)\exp(-E_r/kT)$. For example, the orientation of a rod (domain) comprising more than 10^6 alkane molecules may occur at 2 T and $\langle |\cos\{\pi/2 - \varphi\}| \rangle$ increases in sigmoid with H ; that is, the molecular axis along a hydrocarbon chain tends to orient in perpendicular to the direction of a magnetic field.⁸ Therefore, the high magnetic field perpendicular to a membrane surface could change the tilt angle of chain molecules in the membrane on an electrode to control the electron tunneling reaction.

In this paper, we examined magnetic field effects on electron tunneling reactions of a ferrocenyl surfactant on a gold electrode. Magnetic fields depressed apparent electron tunneling rate by changing the electron tunneling pathway from the through-bond to through-space with cooperative orientation of alkyl chains. Steady magnetic fields may be useful to investigate the tunneling

* To whom correspondence should be addressed. E-mail: sozeki@shinshu-u.ac.jp

processes in organized molecular systems and control the tunneling reactions.

Experimental Section

(Ferrocenylmethyl)dodecyldimethylammonium bromide (FDDA; TCI, Co. Ltd.) and 11-mercaptopoundecanoic acid (MUA; Aldrich Chemicals, Co. Ltd.) were used without further purification. All aqueous solutions were prepared with a deionized, distilled water prepared by a Toyo Aquarius GS-20N apparatus.

Au disk electrodes (Bare-Au) of the diameter of 2 mm for the working electrode were polished carefully with an alumina slurry (0.05 μm in diameter), followed by sonication with water for 15 min, and cleaned electrochemically in 0.05 mol dm^{-3} (M) aqueous H_2SO_4 solution prior to membrane formation. An FDDA coated Au electrode (FDDA-Au) and the mixed monolayer⁹ of FDDA and MUA coated on an Au electrode (FDDA(SAM)-Au) were prepared by immersion of a Bare-Au electrode and an MUA coated Au electrode (SAM-Au), respectively, in 0.5 mM aqueous FDDA solution for 2 h, rinsed with water, and then dried under a N_2 gas. The SAM-Au was obtained by immersing a Bare-Au electrode into 3 mM MUA ethanol solution for 8 h, washed with ethanol and subsequently water, followed by drying under a N_2 gas.

A conventional three-electrodes arrangement was used for cyclic voltammetry (CV) which was measured with an electrochemical instrument Hokuto Denko HAB-151; a Ag/AgCl/saturated KCl electrode as the reference electrode, the working Au electrode, and a Pt disk as the counter electrode. The electron-tunneling reaction of the ferrocenyl/ferricinium (Fc/Fc^+) redox couple on FDDA-Au or FDDA(SAM)-Au in 1 M KNO_3 aqueous solution and on Bare-Au and SAM-Au in 0.5 mM aqueous FDDA solution of 10 mM KCl, referring to FDDA/Au and FDDA/(SAM)Au, respectively, was examined at a scan rate 100 mV s^{-1} and 308 \pm 0.1 K under homogeneous, steady magnetic fields (6 T; within 2%) using a superconducting magnet (JASTEC, Co. Ltd.). The magnetic fields were applied in perpendicular to the electrode surface in order to avoid the magnetohydrodynamic effect.

Results

The cyclic voltammograms of FDDA-Au in 1 M KNO_3 solution were very similar to those of the FDDA/Au system (Bare-Au in 0.5 mM FDDA solution containing 10 mM KCl), besides the magnitude of the peak current, indicating that FDDA molecules should be adsorbed to form an FDDA membrane on Bare-Au, despite no thiolates. Therefore, most CV were measured in FDDA/Au systems, instead of FDDA-Au systems, because the membrane of FDDA-Au was unstable against CV scans or standing time (over 1 h) in 1 M KNO_3 solution.

The cyclic voltammograms of FDDA/Au systems at various magnetic field intensities are shown in Figure 1. It seems that the anodic peak changed much more than the cathodic peak with magnetic fields. Both the peak to peak separation ΔE_p ($=E_{\text{pa}} - E_{\text{pc}}$, where the subscripts a and c mean anodic and cathodic peaks, respectively) and the peak currents i_{pa} and $|i_{\text{pc}}|$ increased with increase in magnetic field, as shown in Figure 2. The trends in FDDA/Au systems are very different from usual ones in the electron-tunneling reaction of thiolates having a redox couple, in which ΔE_p increased with increasing i_c , whereas the peak currents decreased. Moreover, the formal potential E^0 ($= (E_{\text{pa}} + E_{\text{pc}})/2$) increased almost linearly with increase in magnetic field because of an increase in both E_{pa} and E_{pc} (Figure 2A), also different from usual cases in which E^0 was kept constant because E_{pa} and E_{pc} would change linearly to the oppo-

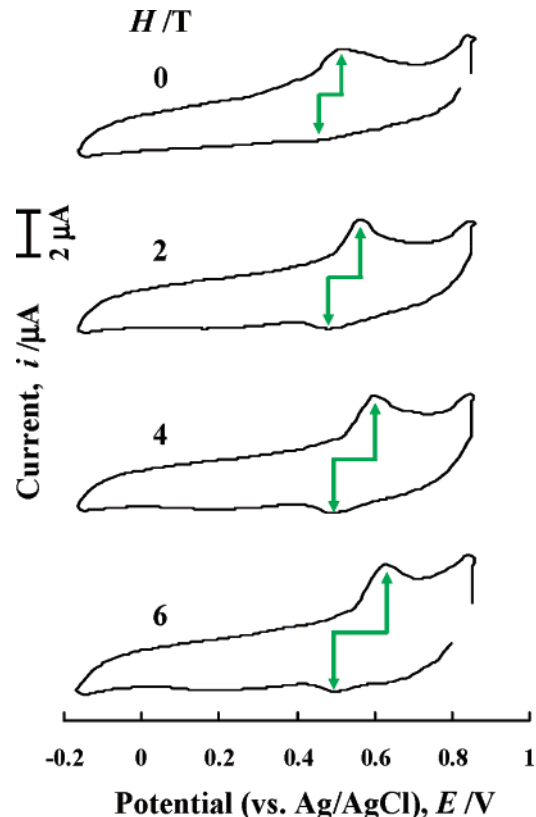


Figure 1. Cyclic voltammograms of FDDA/Au systems, i.e., 0.5 mM FDDA in 10 mM aqueous KCl solution using Bare-Au, at various magnetic field intensities H and 308 ± 0.1 K. The magnetic fields were applied in perpendicular to the membrane or electrode surface. CV scan rate was 100 mV s^{-1} .

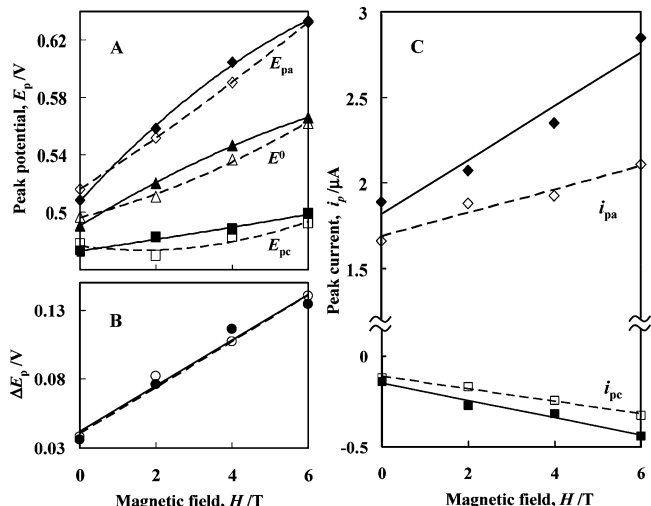


Figure 2. CV peak data of FDDA/Au systems estimated from Figure 1 (solid line) and FDDA/(SAM)Au systems (broken line). Steady magnetic fields H were applied in perpendicular to the membrane or electrode surface at 308 ± 0.1 K. CV scan rate was 100 mV s^{-1} . (A) Anodic E_{pa} (diamond), cathodic E_{pc} (square), and formal potentials E^0 (triangle) as a function of H . (B) Peak-to-peak separation potential ΔE_p as a function of H . (C) Anodic i_{pa} (diamond) and cathodic peak currents $|i_{\text{pc}}|$ (square) as a function of H .

site directions. Thus, it should be noted that the cathodic peak rather was greatly influenced by magnetic fields to bring about an increase in E^0 and ΔE_p , demonstrating that the environment, probably hydration states, around the Fc/Fc^+ couple and the electron-tunneling pathway should be modified by magnetic fields.

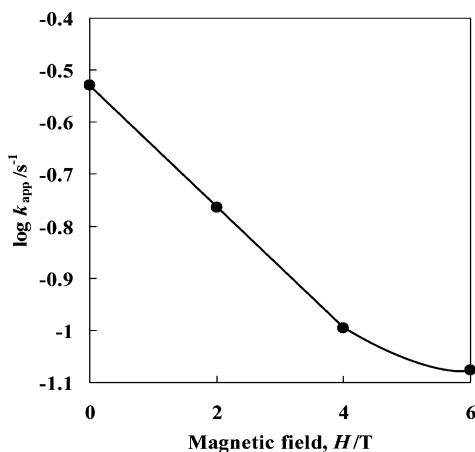


Figure 3. Logarithm of the apparent electron-transfer rate constant k_{app} of FDDA/Au systems as a function of H . The k_{app} values were estimated from eqs 2 and 3 using CV data at various scan rates.

The mixed monolayer of FDDA and MUA molecules, FDDA(SAM)-Au, was prepared in order to stabilize an FDDA membrane. The cyclic voltammograms of the FDDA(SAM)-Au systems were again very similar to those of the FDDA/(SAM)Au system. Figure 2 includes the results for the FDDA/(SAM)Au systems. The results are very similar to those for the FDDA/Au system, suggesting that the Au...CH₃ and Au-S contacts should not be a dominant step in the electron tunneling.

The apparent electron-transfer rate constant k_{app} of the FDDA/Au systems under magnetic fields was estimated from the redox potential splittings between the peak potentials E_{pc}^H or E_{pa}^H at H and the formal potential E^0 at zero field, based on the Laviron's formalism.¹⁰

$$E_{pc}^H - E^0 = (RT/\alpha n_e F) \ln[\alpha n_e F v / RT k_{app}] \quad (2)$$

$$E_{pa}^H - E^0 = [RT/(1-\alpha)n_e F] \ln[(1-\alpha)n_e F v / RT k_{app}] \quad (3)$$

where v is the potential scan rate (0.05, 0.1, 0.2, and 0.5 V s⁻¹), α is the electron-transfer coefficient, n_e is the number of transfer electrons per a redox couple, and F , R , and T have the usual meanings. The k_{app} and α values at each magnetic field intensity were estimated using $E^0(H)$ for E^0 . The α value changed from 0.66 at zero field to 0.31 at 6 T. Figure 3 shows that $\log k_{app}$ decreased linearly with increasing H , besides in the high H region, or that k_{app} changed exponentially with H :

$$k_{app} = k_{app}^0 \exp(-\gamma H) \exp \delta(H) \quad (4)$$

where γ is the positive constant and $\delta(H)$ is the parameter to express the higher order dependence on H . It suggests that the tunneling process of the Fc/Fc⁺ couple in the FDDA membrane systems should be retarded under steady magnetic fields.

Discussion

The characteristics of the magnetic field effects on cyclic voltammograms in the FDDA and mixed FDDA monolayers is apparent contradiction between ΔE_p and i_p , that is, the facts that both increased with increasing magnetic fields and increased in the formal potential $E^0(H)$ with increasing a magnetic field. The barrier thickness d is reduced by tilt of the molecular axes of FDDA and MUA through magnetic orientation. Since the reduction of d should lead to a decrease in ΔE_p and an increase in i_p , the behaviors observed in the systems under magnetic fields are very different from the usual tunneling processes.

The d dependence, usually the l_c dependence, appears in ΔE_p . When the alkyl chains orient under a magnetic field perpendicular to the membrane surface to tilt greatly from an initial angle to the average tilt angle $\varphi(H)$, the barrier thickness d of the membrane will decrease monotonically to $l_c \cdot \cos \varphi(H)$ with increasing magnetic field and then ΔE_p should decrease with H . However, the observation under magnetic fields was not the case, as seen in Figure 2A, suggesting that the electron-tunneling pathway is neither the through-bond nor the through-space. The findings seem to demonstrate that the space-through pathway due to superexchange chain-to-chain coupling between tilted hydrocarbon chains as well as the through-bond superexchange pathway must play an important role in the electron tunneling. The increase in the tilt angle of hydrocarbon chains due to cooperative, magnetic orientation may bring about change of the electron tunneling pathway of the through-bond to through-space. The increase in the path length associated with interchain superexchange hops will lead to the increase ΔE_p . The length $L_t(H)$ of a tunneling pathway comprising the through-bond superexchange along a chain, and the through-space superexchange due to a single interchain hop is given by the following equation:

$$L_t(H) = l_c - a \sin \varphi(H) + a \cos \varphi(H) = \\ l_c + 2^{1/2} a \cos[\varphi(H) + \pi/4] \quad (5)$$

where a is the distance between adsorption sites of the electrode surface and $a \cdot \cos \varphi(H) \equiv d_{cc}$ is the chain-to-chain distance or the hopping distance. In many cases, a is 0.5 nm or more for thiolates adsorbed on Au surfaces such as (111) and (100) crystal surfaces and amorphous Au surfaces, and the tilt angle (at zero magnetic field) is around 27°.^{1,2,4} Though the second term of the last equation in eq 5 would depend on the tunnel-hopping probability p , its value should be positive whenever the tilt angle $\varphi(H)$ is not beyond $\pi/4$. Thus, the tunneling path length $L_t(H)$ may become greater than the chain length l_c by one hop, which should lead to an increase in ΔE_p , but an increase in a magnetic field should bring about a decrease in ΔE_p because the increase of $\varphi(H)$ reduces $L_t(H)$. In order to increase $L_t(H)$ with an increase in magnetic field, the number of hop $N(H)$ and the hopping probability $p(H)$ should increase with increasing magnetic field intensity; that seems to be possible because the larger the tilt angle is, the smaller the chain-to-chain distance d_{cc} is. Then, eq 5 is modified into the following equation.

$$L_t(H) = l_c + 2^{1/2} N(H)p(H)a \cos[\varphi(H) + \pi/4] \quad (6)$$

We can expect that the increment of the factor $N(H)p(H)$ due to magnetic field overcomes the decrement of the factor $\cos[\varphi(H) + \pi/4]$.

The expectation seems to be consistent with the peak current enhancement due to magnetic field (Figure 2C), though i_p usually decreased when ΔE_p increased with increasing d or l_c . The closer side-by-side contact of chains tilting under magnetic fields may proceed to superexchange couple between the chains to promote the chance of hops. The parallel conduction pathways for a tunneling electron may enhance the peak current under magnetic fields. Figure 4 depicts a schematic model for the magnetic field effect on the electron tunneling through an organic monolayer. Referring to a theory at zero magnetic field,³ the total tunneling current I_t under a magnetic field may be given by the following equation:

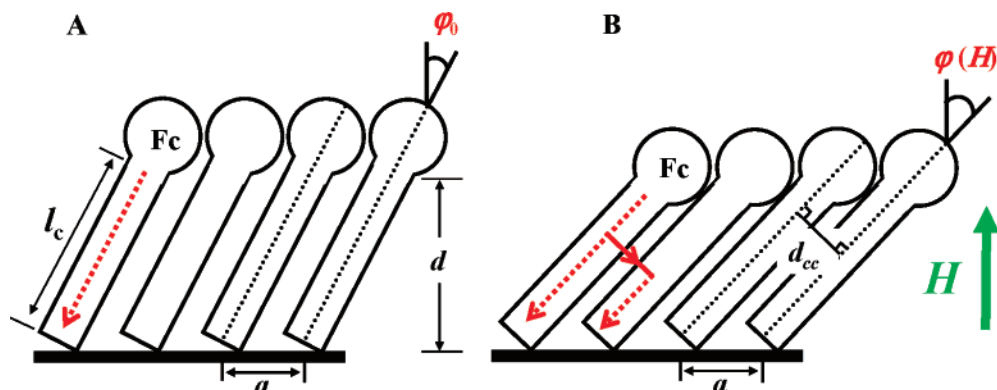


Figure 4. Schematic model for the magnetic field effect on the electron tunneling through an FDDA monolayer on an Au electrode: Changes of the electron tunneling pathways of the through-bond to the through-space with magnetic fields. (A) The average tilt angle φ_0 of hydrocarbon chains in the initial state at zero magnetic field. Red dotted arrow shows the through-bond tunneling current. (B) The average tilt angle $\varphi(H)$ under a magnetic field H perpendicular to the membrane surface. Red solid arrow shows the interchain tunneling current. Here, a is the distance between adsorption sites of the electrode surface, l_c is the chain length, d is the physical thickness of the membrane along the surface normal, and d_{cc} is the chain-to-chain distance or the hopping distance.

$$I_t = I_0 \exp(-\beta_{tb} l_c) + I_0 \sum N(H) C n_s \exp[-\beta_{tb} \{l_c - N(H)a \sin \varphi(H)\}] \exp[-\beta_{ts}(H)N(H)a \cos \varphi(H)] \quad (7)$$

where n_s is the statistical factor which may be assumed to be the same as the number of carbons in a hydrocarbon chain, β_{tb} is the decay constant for through-bond tunneling, and $\beta_{ts}(H)$ is the tunneling constant for interchain tunneling at H . In the sum, the number of interchain hops $N(H)$ is constrained by $N(H) \leq l_c/\{a \sin \varphi(H)\}$. The total current in the $\text{Ru}(\text{NH}_3)_6^{3+}/\text{dodecane-thiolate}/\text{Hg}$ (drop electrode) system increased drastically as the tilt angle of the thiolates increased beyond 30° and was simulated successfully by single interchain hop.^{3a} In the case of multiple interchain hopping, the total current depended strongly on the tilt angle higher than 35° .^{3b} These results suggest that in our systems the multiple interchain hopping pathways should contribute to the tunneling current at large tilt angle or high magnetic fields.

The Marcus theory⁵ for k_{et} takes into account the electronic coupling between a redox couple and electrode through a membrane, which depends exponentially on the physical thickness d of the membrane along the surface normal:

$$k_{et} \propto \exp\{-\beta(d - 3)\} \exp\{-(\Delta G^\circ + \lambda)^2/4RT\lambda\} \propto \exp(-\beta d) \quad (8)$$

Here, β is the electron tunneling constant and ΔG° and λ are the free energy change and reorganization energy associated with the electron transfer, respectively. Since ΔG° and λ are generally unchanged during electron transfer, the second relation is assumed. Under magnetic fields, the d dependence of the rate constant, $\exp(-\beta d)$, should be replaced by the pathways dependence, as described in eqs 6 and 7. Thus, the exponent must become a complex function of H , $f(H)$. Supposing that ΔG° and λ should depend on a magnetic field, the electron-transfer rate constant at H , k_{et}^H , may be expressed by

$$k_{et}^H \propto \exp\{-f(H)\} \exp\{-(\Delta G^\circ(H) + \lambda(H))^2/4RT\lambda(H)\} \quad (9)$$

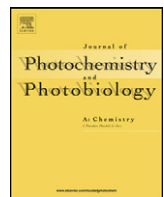
Equation 9 seems to be comparable for the experimental k_{app} , eq 4, and may explain the magnetic field dependence of the formal potential (Figure 2A). Redox reactions are very sensitive to an atmosphere around a redox couple, for example, the number and orientation of water molecules hydrated. Since it was reported that magnetic fields promoted hydration around solid surfaces¹¹ and ions¹² and hydrogen bonds of water,^{13,14}

an Fc/Fc^+ couple may be affected by magnetic fields. Thus, it is likely that a hydrophobic Fc and hydrophilic Fc^+ should be stabilized and destabilized, respectively, under steady magnetic fields to change the formal potential of the Fc/Fc^+ couple.

Acknowledgment. This work was supported by Grant-in-Aid of Scientific Research for Priority Area (Area 767, No. 15085204) and No. 16655004 from MEXT of Japan.

References and Notes

- Khoshtariya, D. E.; Dolidze, T. D.; Zusman, L. D.; Waldeck, D. H. *J. Phys. Chem. A* **2001**, *105*, 1818.
- Napper, A. M.; Liu, H.; Waldeck, D. H. *J. Phys. Chem. B* **2001**, *105*, 7699. Sek, S.; Misicka, A.; Bilewicz, R. *J. Phys. Chem. B* **2000**, *104*, 5399. Sek, S.; Bilewicz, R. *J. Electroanal. Chem.* **2001**, *509*, 11.
- (a) Slowinski, K.; Chamberlain, R. V.; Miller, C. J.; Majda, M. *J. Am. Chem. Soc.* **1997**, *119*, 11910. (b) Yamamoto, H.; Waldeck, D. H. *J. Phys. Chem. B* **2002**, *106*, 7469.
- Finklea, H. O.; Liu, L.; Ravenscraft, M. S.; Ounturi, S. *J. Phys. Chem.* **1996**, *100*, 18852.
- Marcus, R. A.; Sutin, N. *Biochim. Biophys. Acta* **1985**, *811*, 265.
- Gaffney, B. J.; McConnell, H. M. *Chem. Phys. Lett.* **1974**, *24*, 310. Maret, G.; Dransfeld, K. *Physica* **1977**, *86–88B*, 1077. Tenforde, T. S.; Liburdy, R. P. *J. Theor. Biol.* **1988**, *133*, 385.
- Ozeki, S.; Kurashima, H.; Miyanaga, M.; Nozawa, C. *Langmuir* **2000**, *16*, 1478. Ozeki, S.; Kurashima, H.; Abe, H. *J. Phys. Chem. B* **2000**, *104*, 5657. Kurashima, H.; Abe, H.; Ozeki, S. *Mol. Phys.* **2002**, *100*, 1445. Ozeki, S.; Kurashima, H. *Encyclopedia of Surfaces and Colloid Science*; Hubbard, A., Ed.; Marcel Dekker: New York, 2002; Vol. 3, p 3109. Otsuka, I.; Abe, H.; Ozeki, S. *Sci. Technol. Adv. Mater.* **2006**, *7*, 327. Ozeki, S.; Fujio, K. *Magneto-Science*; Tanimoto, T., Yamaguchi, M., Eds.; Kodansha-Elsevier: Tokyo, 2006; p 150.
- Bragonza, L. F.; Blott, B. H.; Coe, T. J.; Melville, D. *Biochim. Biophys. Acta* **1984**, *801*, 66.
- The FDDA(SAM)-Au membrane could not be a bilayer comprising an FDDA monolayer formed on the SAM monolayer of MUA, but a mixed monolayer of FDDA and MUA molecules, because there was no dependence of ΔE_p on the barrier thickness of other SAMs used instead of the SAM of MUA.
- Laviron, E. *J. Electroanal. Chem.* **1979**, *101*, 19.
- Ozeki, S.; Wakai, C.; Ono, S. *J. Phys. Chem.* **1991**, *95*, 10557. Ozeki, S.; Miyamoto, J.; Watanabe, T. *Langmuir* **1996**, *12*, 2115. Ozeki, S.; Miyamoto, J.; Ono, S.; Wakai, C.; Watanabe, T. *J. Phys. Chem.* **1996**, *100*, 4205. Ozeki, S.; Sato, H. *Encyclopedia of Surfaces and Colloid Science*; Hubbard, A., Ed.; Marcel Dekker: New York, 2002; Vol. 3, p 3120.
- Higashitani, K.; Iseri, H.; Okuhara, K.; Kage, A.; Hatake, S. *J. Colloid Interface Sci.* **1995**, *172*, 383. Higashitani, K.; Oshitani, J. *J. Colloid Interface Sci.* **1998**, *204*, 363.
- Hosoda, N.; Mori, H.; Sogoshi, N.; Nagasawa, A.; Nakabayashi, S. *J. Phys. Chem. A* **2004**, *108*, 1461. Inaba, H.; Saitou, T.; Tozaki, K.; Hayashi, H. *J. Appl. Phys.* **2004**, *96*, 6127. Iwasaka, M.; Ueno, S. *J. Appl. Phys.* **1998**, *83*, 6459.
- Otsuka, I.; Ozeki, S. *J. Phys. Chem. B* **2006**, *110*, 1509. Ozeki, S.; Otsuka, I. *J. Phys. Chem. B* **2006**, *110*, 20067.



Influence of pH on dendritic structure of strongly fluorescent persulfate-treated poly(amidoamine) dendrimer

Govindachetty Saravanan*, Hideki Abe**

Advanced Electronic Materials Center, National Institute for Materials Science, 1-2-1 Senken, Tsukuba, Ibaraki 305-0047, Japan

ARTICLE INFO

Article history:

Received 9 March 2011

Received in revised form 25 August 2011

Accepted 9 September 2011

Available online 16 September 2011

Keywords:

Poly(amidoamine) dendrimer
Ammonium persulfate treatment
Fluorescence
Dendritic structure
FT-IR spectroscopy
X-ray photoelectron spectroscopy

ABSTRACT

The influence of pH on the dendritic structure of strongly fluorescent ammonium persulfate (APS)-treated poly(amidoamine) (PAMAM) dendrimers was examined. The APS-treated PAMAM dendrimers were prepared by aging of 0.2 mM aqueous solutions of a hydroxyl groups-terminated, generation-five PAMAM (G5OH) dendrimer together with 200 µl of 0.1 M APS solutions. The G5OH dendrimer showed an absorbance at 280 nm, which was red-shifted to 360 nm after APS treatment. The APS-treated G5OH dendrimer solutions emitted much stronger fluorescence than the pristine G5OH dendrimer solutions when irradiated at 360 nm. The pH of the G5OH dendrimer solution is 7.6 while that of the APS-treated G5OH dendrimer solution is 5.2. The pore surface of both pristine and fluorescent G5OH dendrimers was altered more significantly under acidic than basic conditions. The tertiary amine groups of the pore surface of the fluorescent G5OH dendrimers were protonated by APS treatment as well as under the acidic condition; therefore, the pore surface of the G5OH dendrimer was filled with tertiary ammonium cations, which were, however, further deprotonated under basic conditions. The sulfur anions (VI and II) were generated during the hydrolysis of APS, which were interacted with the G5OH dendrimers under both acidic and basic conditions.

© 2011 Elsevier B.V. All rights reserved.

1. Introduction

It has been found that bio-compatible, nonimmunogenic, poly(amidoamine) (PAMAM) dendrimers emit purely intrinsic but weak blue-fluorescence upon irradiation of UV light [1]. Despite the potential versatility of PAMAM dendrimers, weakness in the fluorescence has limited their applications in the biomedical area. Therefore, research on the enhancement of the fluorescence of PAMAM dendrimers has been fueled by their potential utilization in practical biomedical applications, such as specific targeting, imaging, and/or treatments of cancer [2].

Strong, monochromatic fluorescent PAMAM dendrimers have been achieved by labeling of fluorescent ligands (e.g., fluorescein isothiocyanate-folic acid) [3] and imaging dyes (e.g., rhodamine and carboxyfluorescein) [4] on the peripheral functional groups of PAMAM dendrimers as well as the synthesis of metal nanoparticles and/or quantum dots on the pore surface of the PAMAM dendrimer (PAMAM dendrimer-encapsulated nanoparticles, PAMAM DENs) [5–7]. The encapsulated metal nanoparticles and/or quantum dot PAMAM DENs showed strong enough fluorescence emission upon

irradiation of UV light. However, PAMAM dendrimers played the role of an optically inert support that dispersed the nanoparticles and/or nanodots in solvents. Fabrications on both the peripheral groups and the pore surface of PAMAM dendrimers by novel fluorophores without altering the physical and chemical properties are often complicated due to the requirements of toxic compounds and multiple synthetic steps. Therefore, purely intrinsic, strong fluorescence emissions of PAMAM dendrimers have been anticipated for biomedical applications.

Lee et al. showed strong, monochromatic fluorescence of generation-two, hydroxyl-terminated PAMAM dendrimers (G2OH) (quantum yield $58 \pm 5\%$ relative to quinine sulfate) in the absence of fluorophores on the pore surface or peripheral functional groups [8]. G2OH dendrimers showed enhanced fluorescence when treated under oxidizing conditions (persulfate-treated PAMAM dendrimers) for several hours. Fluorescent persulfate-treated PAMAM dendrimers have been prepared by aging of PAMAM dendrimers together with persulfate solutions. It has been reported that the pH of persulfate solutions falls to the acidic condition due to the generation of permonosulfuric acid during the aging processes [9]. Although the strong fluorescence behavior of persulfate-treated PAMAM dendrimers has been examined, little information has been obtained about the dendritic structures of persulfate-treated PAMAM dendrimers at different pH.

Various studies about PAMAM dendrimers comprising different generation and peripheral functional groups indicate that

* Corresponding author. Tel.: +81 29 851 3354; fax: +81 29 859 2801.

** Corresponding author.

E-mail addresses: saravanan.govindachetty@nims.go.jp (G. Saravanan), abe.hideki@nims.go.jp (H. Abe).

the fluorescence behavior of PAMAM dendrimers are significantly influenced by the dendritic structures or the pore surface of the functional groups of PAMAM dendrimers rather than the peripheral functional groups [10]. The amide carbonyls and N-H moieties of dendrimers interact on the pore surface through both inter- and intramolecular hydrogen bonding in aqueous solutions [11]. Furthermore, the strength of hydrogen bonding in the dendrimer is enhanced under acidic conditions [12]. The higher generation of PAMAM dendrimers emits considerable fluorescence and is comparable with the lower generation [13]. PAMAM dendrimers emit strong fluorescence at lower pH, and the tertiary amine groups of PAMAM dendrimers are protonated, filling the whole dendritic interior with cations in an acidic medium [12,13a,13b]. By considering the falling of pH of persulfate solutions during hydrolysis, detailed structural characterizations of persulfate-treated PAMAM dendrimers at different pH and the influence of pH on the dendritic structures of PAMAM dendrimers will be needed to understand the strong fluorescence behavior of persulfate-treated PAMAM dendrimers.

In this work, the dendritic structures of ammonium persulfate-treated PAMAM dendrimers (generation-five, hydroxyl-terminated) (hereafter called APS-G5OH) were examined at different pH. The optical properties of APS-G5OH were examined by UV-visible and fluorescence spectroscopy. Fourier-transform IR (FT-IR) and X-ray photoelectron spectroscopy (XPS) techniques were employed to examine the influence of pH on the dendritic structures of PAMAM dendrimers. Pristine generation-five, hydroxyl-terminated PAMAM dendrimers (hereafter called G5OH) were utilized as a reference to compare the optical properties and dendritic structure of APS-G5OH at different pH.

2. Experimental

2.1. Materials

A 5 wt.% methanol solution of G5OH was purchased from Aldrich. Ammonium persulfate ($(\text{NH}_4)_2\text{S}_2\text{O}_8$) (APS) was purchased from Kishida Chemicals. Hydrochloric acid and sodium hydroxide were purchased from Kishida Chemicals. All chemicals were used as received for sample preparation without any further purification. Purified water was prepared using the Millipore system.

Aqueous solutions of 0.2 mM G5OH dendrimers and 0.1 M APS were prepared and stored in the refrigerator. 5 ml of 0.2 mM G5OH solutions was stirred in the presence of 0.2 ml of 0.1 M APS for several days at room temperature. Similarly, 5 ml of 0.2 mM G5OH solutions was prepared for reference purposes but in the absence of APS. The APS-G5OH solution turned to pale yellow, while the pristine G5OH solution remained colorless after 8 days. Diluted hydrochloric acid and sodium hydroxide were used to adjust the pH.

2.2. Characterization

UV-visible and fluorescence spectra of pristine G5OH and APS-G5OH solutions were collected on a Hitachi U-2900 and F-7000, respectively. A Xenon lamp, operated at 150 W, was utilized as an excitation source. The sample solutions were irradiated at 360 nm for the emission spectra and 450 nm for the excitation spectra. FT-IR spectra were obtained in a single-beam absorbance mode at a resolution of 4 cm^{-1} with a Perkin-Elmer FT-IR (Spectrum GX-R) system equipped with a MIRTGS detector. FT-IR samples were prepared by dropping 200 μl of sample solutions onto the surface of CaF_2 crystals and drying them under a vacuum. X-ray photoelectron spectroscopy (XPS) with a Thermo Scientific Theta probe of PAMAM dendrimer films on carbon substrates was performed using an Al $\text{K}\alpha$

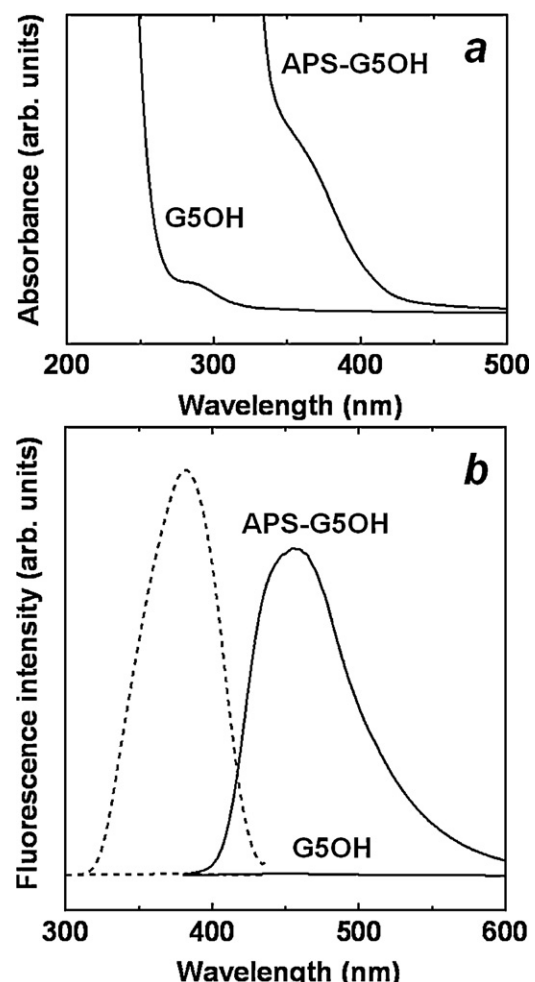


Fig. 1. UV-visible spectra (a) and emission (solid line) and excitation (dashed line) spectra (b) for an aqueous solution of 0.2 mM G5OH and APS-G5OH.

monochromatized X-ray beam at a constant dwell time of 50 ms. An aliquot of 100 μl of sample solutions was dried onto carbon substrates under a vacuum. Carbon black (Vulcan XC-72, Cabot Co., Ltd.) was mixed with the sample solutions for XPS measurements to avoid the charging effect. X-ray scans were performed with a $400\text{ }\mu\text{m}^2$ sampling area using pass energies of 200 eV for a wide scan and of 100 eV for a narrow scan. The anode voltage and current were 14 kV and 7.2 mA, respectively. All core-level spectra were obtained at photoelectron takeoff angles between 20.31° and 79.69° with respect to the PAMAM dendrimer films.

3. Results and discussion

3.1. Optical properties of pristine and APS-G5OH dendrimer

Fig. 1a shows the UV-visible spectra for an aqueous solution of 0.2 mM G5OH and APS-G5OH. G5OH showed a weak shoulder peak at 280 nm, may be assigned to the $n-\pi^*$ transition of the branching units of dendrimer molecules [1d]. APS-G5OH also showed a weak shoulder peak; however, the peak shifted substantially to a higher wavelength and was observed at around 360 nm. The aging of the PAMAM dendrimer in the presence of a persulfate solution resulted in a larger red shift in wavelength. Fig. 1b shows the emission and excitation spectra for an aqueous solution of 0.2 mM G5OH and APS-G5OH. The G5OH dendrimer showed weak emission and excitation bands at 445 and 370 nm, respectively. However, APS-G5OH showed very strong emission and excitation bands which

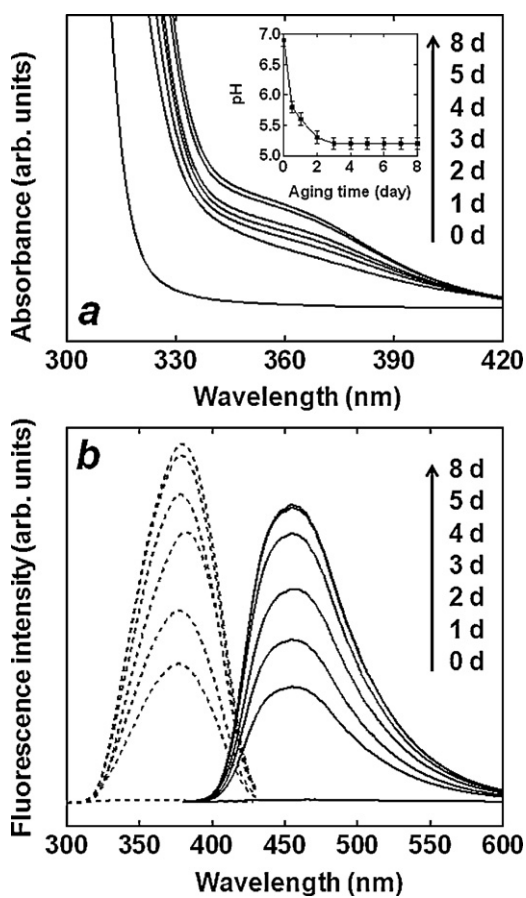
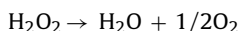
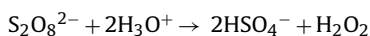
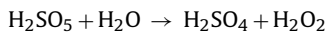
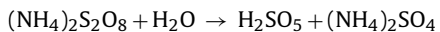


Fig. 2. UV-visible spectra (a) and emission and excitation spectra (b) for an aqueous solution of 0.2 mM G5OH in the presence of APS at different aging interval. Inset shows the pH dependences as a function of aging interval.

were shifted to a higher wavelength ca. 10 nm, consistently with other reported results [8].

The aging effects of G5OH in the presence of APS were also examined. Fig. 2a shows the successive UV-visible spectra for an aqueous solution of 0.2 mM APS-G5OH at various aging interval. The weak shoulder peak of G5OH showed red shift in wavelength with increasing aging. The intensity of emission and excitation bands for APS-G5OH became much stronger with increasing aging as shown in Fig. 2b, indicating that the optical properties of G5OH were altered significantly during aging. It should be noted that pH of APS-G5OH solution decreased with increasing aging interval and reached a constant pH value after 2 days as shown in the inset of Fig. 2a. pH of the pristine G5OH solution is 7.6, while pH of the APS-G5OH is 5.2. This is because permonosulfuric acid, sulfuric acid, peroxyomonosulfate, and hydrogen peroxide were generated during the hydrolysis of APS by the following reactions [9].



The red shift in absorption band as well as the enhancement in the fluorescence of APS-G5OH is most likely attributed to changes in the dendritic structure due to the falling of pH. Wang et al. reported that generation-four amine-terminated PAMAM dendrimers emitted strong fluorescence under acidic conditions and also showed

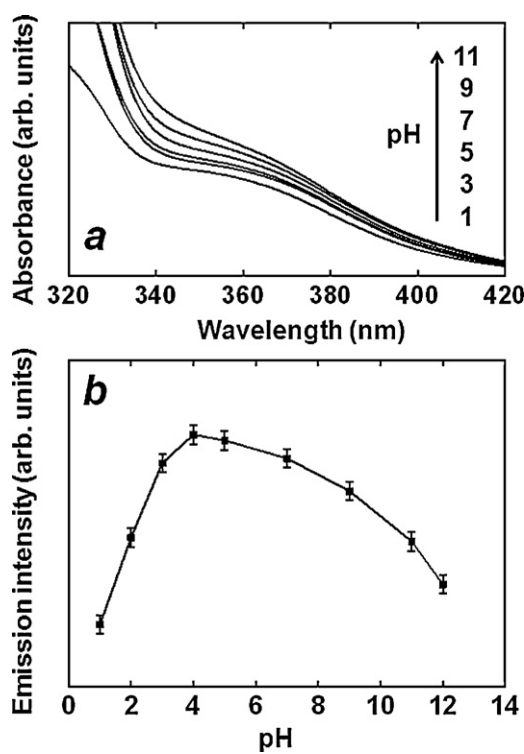


Fig. 3. UV-visible spectra (a) and emission intensities (b) for an aqueous solution of aged 0.2 mM APS-G5OH at different pH.

that the fluorescence emission of PAMAM dendrimers is strongly dependent on the pH of the sample solution [10].

The optical properties of APS-G5OH were further examined at different pH. Fig. 3a shows the UV-visible spectra for an aqueous solution of 0.2 mM APS-G5OH at different pH. The weak shoulder peak of APS-G5OH showed red shift in wavelength with increasing pH. Fig. 3b shows the emission intensities of an aqueous solution of APS-G5OH at different pH. The emission intensity of APS-G5OH showed a critical pH at 4, where the strong fluorescence emission was observed. However, the emission intensity of APS-G5OH decreased rapidly both under acidic condition at less than 4 and basic condition. The similar critical pH has also been observed in the case of generation 2 and 4, amine terminated PAMAM dendrimer [10]. These results indicate that dendritic structure of APS-G5OH was altered significantly by changing of pH.

3.2. FT-IR spectra of pristine and APS-G5OH dendrimers

FT-IR spectroscopic measurements were performed over pristine G5OH and fluorescent APS-G5OH to examine the dendritic structures after APS treatment. Fig. 4 shows the FT-IR spectra of G5OH and APS-G5OH films that were prepared from the as-prepared sample solutions on the CaF₂ substrate. The G5OH film showed a shoulder and a characteristic band at approximately 3500 and 3300 cm⁻¹ for O-H (terminal groups) and a hydrogen-bonded N-H stretching band of the amide functional groups of the PAMAM dendrimer, respectively [11b]. The band was observed at 3090 cm⁻¹ and can be assigned to the overtone of the (N-H) bending/(C-N) stretching modes. Symmetric and asymmetric stretching vibrations of methylene groups were observed at 2837 and 2942 cm⁻¹, respectively (Fig. 4a) [11b]. The shoulder band for the surface hydroxyl group remained at approximately the same position in the case of the APS-G5OH film. However, a broad band was observed in the region ~3300 cm⁻¹ for the APS-G5OH dendrimer due to the overlapping of hydrogen-bonded N-H

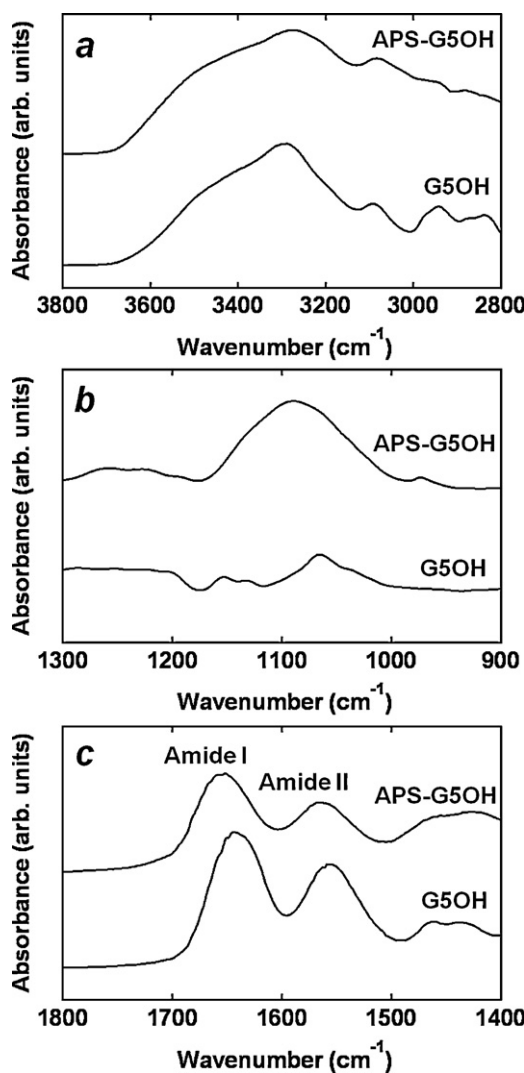


Fig. 4. FT-IR spectral profiles of as-prepared G5OH and APS-G5OH films.

of the amide functional group and anti-symmetric stretching vibrations of ammonium ions, which can also be observed in the same region [14]. Moreover, the symmetric and asymmetric stretching vibrations of methylene groups of G5OH became weaker after APS treatment. Fig. 4b shows a C–N stretching band for tertiary amines of G5OH, which was observed at 1066 cm⁻¹ [15]. In addition to that, a weak doublet peak was observed in the region of 1132–1153 cm⁻¹ for skeletal C–C stretching [11b]. However, the APS-G5OH showed a broad band in the region of 1175–990 cm⁻¹ due to the overlapping of the C–N stretching band, skeletal C–C stretching band, asymmetric stretching band of SO₄²⁻ (1090 cm⁻¹), and HO–S–OH symmetric bending (1137 cm⁻¹) (see text for details) [11b,16]. In addition, a weak band at 972 cm⁻¹ also evidenced the existence of SO₄²⁻ in APS-G5OH [14b]. G5OH showed two strong absorption peaks at 1642 and 1555 cm⁻¹ that can be assigned to a carbonyl (C=O) stretching mode of the amide group (amide I) and (N–H) bending/(C–N) stretching modes (amide II), respectively as shown in Fig. 4c [11b,17]. In addition to these peaks, a couple of weak peaks for CH₂ scissoring modes were observed in the region from 1435 to 1460 cm⁻¹ [18]. Both the amide I and II stretching bands of APS-G5OH shifted to a higher wavenumber by 10 cm⁻¹ relative to that for pristine G5OH. These results indicate that the dendritic structure or the pore surface of the APS-G5OH is significantly altered by APS treatment and, thus, the dendritic structure of APS-G5OH is different from that of pristine G5OH.

3.2.1. FT-IR spectra of pristine and APS-G5OH dendrimer under different pH

The pristine G5OH and APS-G5OH films were examined further at different pH to ensure the influence of pH on the dendritic structure. Fig. 5 shows the FT-IR spectra for G5OH and APS-G5OH films that were prepared from the as-prepared PAMAM dendrimer solutions at different pH. At any pH, the stretching bands of surface hydroxyl groups ($\approx 3490\text{ cm}^{-1}$) of G5OH did not change. The band for the hydrogen-bonded N–H of the amide functional group of G5OH became broader under acidic conditions, likely due to the enhancement in the strength of hydrogen bonding with near-pore-surface functional groups as well as the protonation of tertiary amine groups [12,13]. However, at higher pH, the hydrogen-bonded N–H stretching band could be clearly seen. The stretching bands for the overtone of amide II and symmetric and asymmetric stretching modes of methylene groups did not change at any pH (Fig. 5a). Fig. 5b shows the FT-IR spectra for APS-G5OH films at different pH. At any pH, no significant changes were observed for the stretching bands of either the surface hydroxyl- or hydrogen-bonded N–H groups; however, the N–H stretching band was slightly broader at higher pH. The C–N stretching band of tertiary aliphatic amines of as-prepared G5OH did not change at any pH. Skeletal C–C stretching bands could be clearly seen when the pH was above 3 (Fig. 5c). However, a broad band was observed in the region of 1170–990 cm⁻¹ for APS-G5OH under acidic conditions. This broad band was separated into multiple bands when the pH of the solutions is above 7 that can be assigned for C–N stretching band and skeletal C–C stretching, asymmetric stretching band of SO₄²⁻ (1090 cm⁻¹) and HO–S–OH symmetric bending (1137 cm⁻¹) [11b,16]. The asymmetric stretching band of SO₄²⁻ and HO–S–OH symmetric bending can be clearly seen under basic conditions and is stronger at higher pH (Fig. 5d). Fig. 5e and f shows the characteristic changes for the amide I and II bands of G5OH and APS-G5OH at different pH, respectively. As can be seen in more detail in Fig. 6, the amide I band of as-prepared G5OH shifts to a higher wavenumber with decreasing pH. Conversely, no significant shift was observed with increasing pH. It should be noted that the amide II band of as-prepared G5OH changes under neither acidic nor basic conditions. In contrast, the amide I band of as-prepared APS-G5OH shifts to a higher wavenumber with decreasing pH but drastically to a lower wavenumber with increasing pH. The amide II band of as-prepared APS-G5OH does not change further with decreasing pH but shifts to a lower wavenumber with increasing pH. The amide I band for both G5OH and APS-G5OH shifts to a higher wavenumber under acidic conditions, likely due to the enhancement in the strength of hydrogen bonding.

These results indicate that the pore surface of G5OH and APS-G5OH was significantly altered under different pH and can be manipulated on the basis of the following explanations. (i) The strength of the hydrogen bonding on the pore surface of PAMAM dendrimers is likely to be enhanced under acidic conditions [12]. (ii) The pK_a value of the tertiary amine of the pore surface is in the range between 3 and 6. Therefore, the tertiary amines of the pore surface of PAMAM dendrimers are protonated under acidic conditions, resulting in the formation of tertiary ammonium cations that makes more rigid-dendritic globular structure due to the strong charge-charge repulsions [13]. (iii) The anions of permonosulfuric acid and/or sulfuric acid, which are generated from the hydrolysis of APS, interacted with G5OH. Furthermore, the interaction of these anions with G5OH can change under different pH.

3.3. X-ray photoelectron spectra of as-prepared pristine and APS-G5OH dendrimer

The chemical states of C 1s, N 1s, O 1s, and S 2p of as-prepared G5OH and APS-G5OH films were examined by XPS measurements

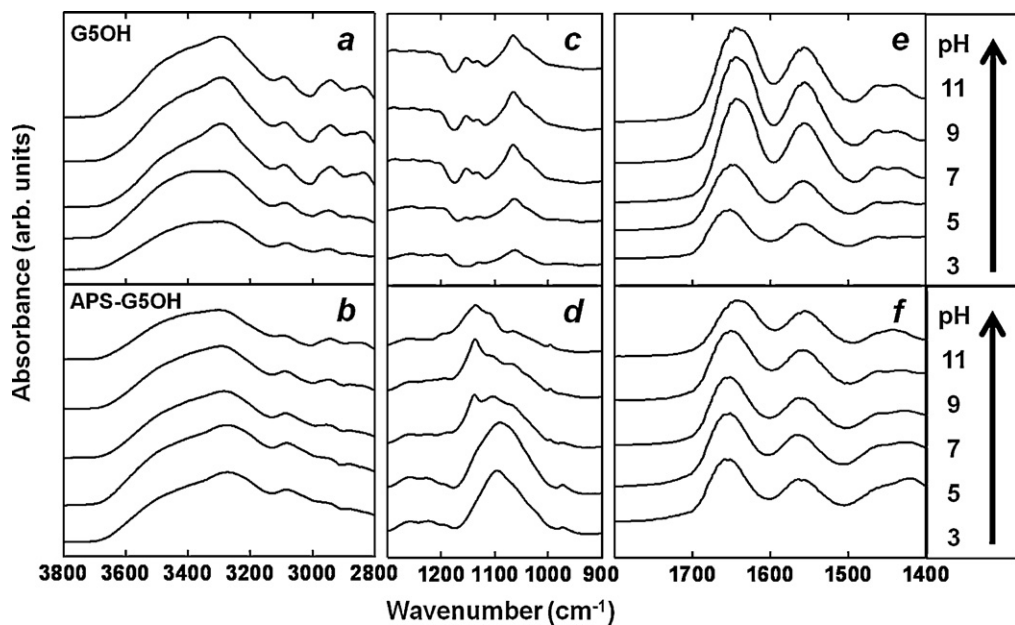


Fig. 5. FT-IR spectral profiles of G5OH and APS-G5OH films. The films were prepared from aqueous solutions of 0.2 mM G5OH and APS-G5OH solutions at different pH.

in order to rationalize the strong fluorescence behavior of APS-G5OH. XPS spectra in the C 1s region for G5OH and APS-G5OH films at any pH showed peaks at the same binding energy of 284.2 eV, indicating that the dendrimer films were free from a charging effect (Fig. S1) [19]. Fig. 7 shows the XPS spectra of as-prepared G5OH and APS-G5OH in the N 1s and O 1s regions. The binding energies of as-prepared G5OH and APS-G5OH are significantly different in the N 1s regions. The N 1s spectra of as-prepared G5OH can be deconvoluted into two component peaks centered at the binding energies of 399.4 and 400.1 eV for tertiary amine and amide groups, respectively [17b,20]. The binding energy of amide nitrogen retained the same position observed at (400.0 eV); however, the tertiary amine peak shifted largely to a deeper level (401.9 eV) due to the formation of a tertiary ammonium cation by protonation of the tertiary amine in the case of the as-prepared APS-G5OH PAMAM dendrimer (pH 5.2) [21]. It should be noted that the binding energy of O 1s of both as-prepared G5OH (532.1 eV) and APS-G5OH (532.2 eV) did not show any significant changes in the O 1s regions [17b,20].

3.3.1. X-ray photoelectron spectra of pristine and APS-G5OH dendrimers in the N 1s region under different pH

Fig. 8 shows the XPS profiles of G5OH and APS-G5OH films prepared from the sample solutions at pH 3 and 11 in the N 1s

region to ensure the influence of pH on the dendritic structures. G5OH showed the binding energies of amide nitrogen and a tertiary ammonium cation peak centered at 400.1 and 402.3 eV in the N 1s region, respectively, at pH 3. No characteristic tertiary ammonium cation peak was observed for G5OH at pH 11; however, a weak peak was observed at 400.6 eV. In addition, no significant changes in the binding energy of amide nitrogen were observed at 400.0 eV at pH 11 (Fig. 8a). APS-G5OH also showed a similar trend in the N 1s region, similarly to G5OH at pH 3 and 11 (Fig. 8b, Table 1). It should be noted that the intensity of the tertiary ammonium cation peak of APS-G5OH is much stronger than that of pristine G5OH relative to the amide nitrogen peak at pH 3. In addition, the binding energy of as-prepared APS-G5OH (401.9 eV) shifts further to a higher binding energy, 402.2 eV at pH 3, indicating that tertiary amine nitrogen was not fully protonated in the case of as-prepared APS-G5OH (pH 5.2). The unprotonated tertiary amine groups of as-prepared APS-G5OH were further protonated with decreasing pH, and, thus, the tertiary ammonium cation peak shifted further to a deeper level (ca. 0.3 eV) compared to as-prepared APS-G5OH. It is worthy of note that a weak peak with slightly higher binding energy than that of the tertiary amine was observed in the cases of both G5OH and APS-G5OH at 400.6 eV and 401.2 eV, respectively, at pH 11, indicating that the tertiary ammonium cation is deprotonated, but not completely, even at higher pH [22]. However, some more direct evidence should be needed to correlate the protonation and deprotonation of the tertiary amine at different pH. Neither G5OH nor APS-G5OH showed any characteristic changes in the O 1s region at either pH 3 or 11, as shown in the supporting information (Fig. S2, Table 1), indicating that the chemical state of oxygen of both amide and surface hydroxyl groups was not affected under either the acidic or the basic condition.

3.3.2. X-ray photoelectron spectra of APS-G5OH dendrimer in the S 2p region under different pH

Fig. 9 shows the XPS profiles of as-prepared APS-G5OH and at pH 3 and 11 in the S 2p region. All profiles show two main peaks of S_A and S_B corresponding to the sulfur atoms, which are in the oxidation state of VI (e.g., SO_4^{2-}) and II (e.g., $S_2O_3^{2-}$, S^{2-}), respectively. The hydrolysis of APS would produce unstable free radicals ($SO_4^{\bullet-}$), hydrogen peroxide, and peroxymonosulfate, which are converted

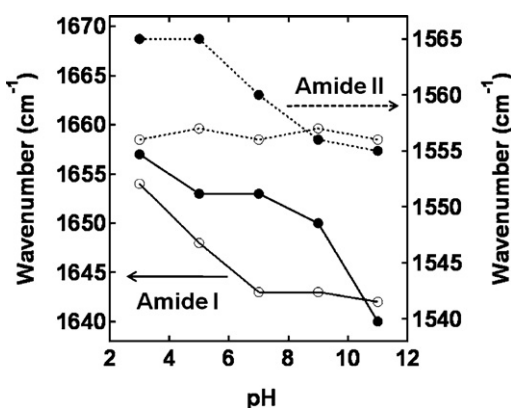


Fig. 6. pH dependences of amide I and II bands of G5OH (open circle) and APS-G5OH (closed circle).

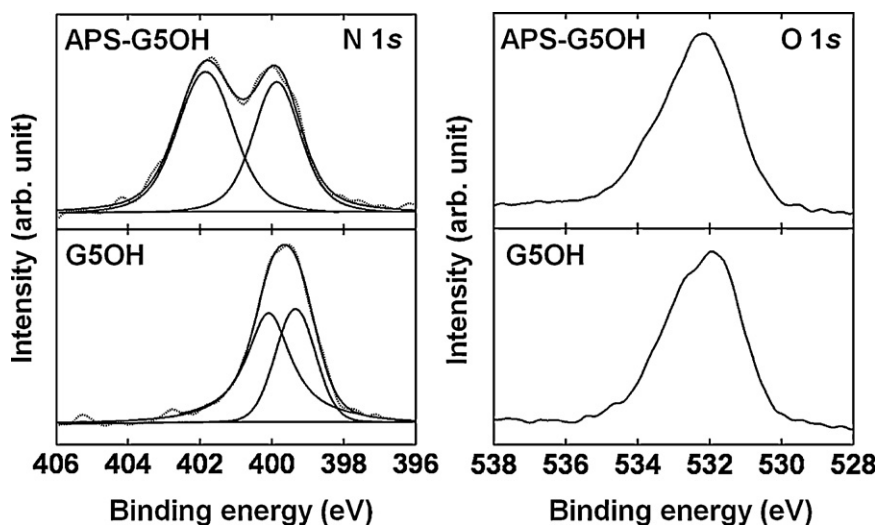


Fig. 7. XPS profiles for the as-prepared G5OH and APS-G5OH in the N 1s and O 1s regions.

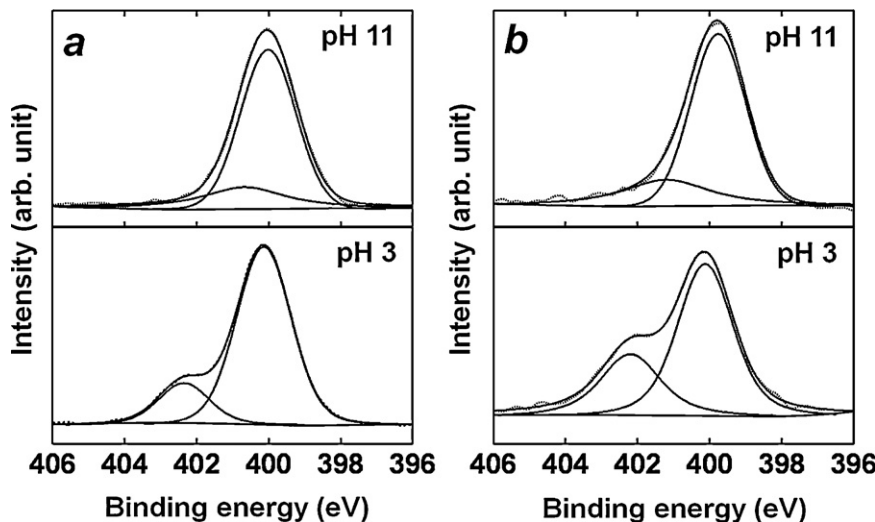


Fig. 8. XPS profiles for G5OH (a) and APS-G5OH (b) in the N 1s regions under acidic (pH 3) and basic (pH 11) conditions.

further into stable sulfur VI and II ions [9b]. It has been reported that the core-level S 2p peaks of H_2SO_4 also show similar S (VI) and S (II) peaks [23]. The S_A peak can be resolved into two component peaks of spin orbit doublets, $S 2p_{3/2}$ and $S 2p_{1/2}$. The spin orbit doublets of as-prepared APS-G5OH ($S 2p_{3/2} = 168.6$ eV and $S 2p_{1/2} = 170.0$ eV) shift to a shallower level under an acidic condition (pH 3) centered at 168.4 and 169.5 eV, respectively. On the other hand, the $S 2p_{3/2}$ peak shifts to a deeper level (168.9 eV), but the $S 2p_{1/2}$ peak retains the same value, similarly to as-prepared

APS-G5OH (170.0 eV) at pH 11. The spin orbit splitting value of as-prepared APS-G5OH (1.40 eV) achieved a lower value at both pH 3 and 11 (1.10 eV). It should be noted that the doublet peak of S_B for as-prepared APS-G5OH showed only a slight change at pH 3; however, the intensity of the S_B peak becomes much stronger than that of S_A at pH 11. These results indicate that the oxidation state of both VI and II corresponding to sulfur atoms of APS-G5OH, as well as their interactions with G5OH, is significantly altered under different pH.

Table 1

XPS binding energy assignments of the core level peaks for as-prepared G5OH and APS-G5OH and under different pH.

Sample	N 1s (eV)		O 1s (eV)		S 2p (eV)	
	$\text{O}=\text{C}-\text{NH}$	$-\text{N}\text{H}$	(-CO, SO, O ₂ , etc.)		$\text{S} (\text{VI})$	
					$2 p_{1/2}$	$2 p_{3/2}$
G5OH (as-prepared)	400.1	399.4	532.1		—	—
APS-G5OH (as-prepared)	400.0	401.9	532.2	170.0	168.6	163.6
G5OH (pH 3)	400.1	402.4	532.2	—	—	—
G5OH (pH 11)	400.0	400.6	532.2	—	—	—
APS-G5OH (pH 3)	400.1	402.2	532.1	169.5	168.4	163.6
APS-G5OH (pH 11)	399.9	401.2	532.1	170.0	168.9	163.6

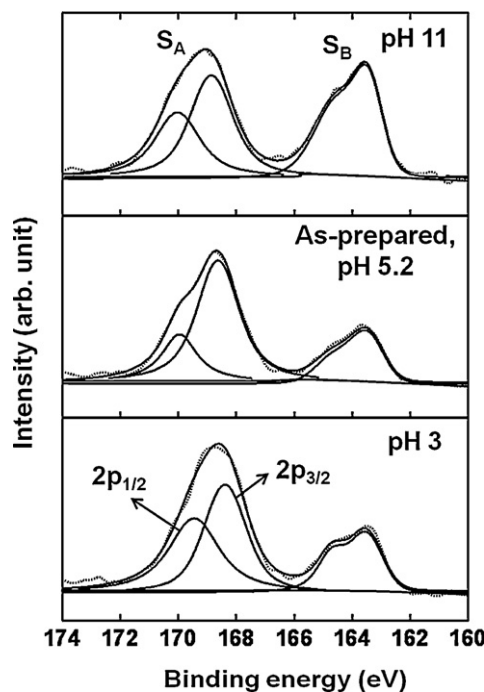


Fig. 9. XPS profiles for APS-treated G5 PAMAM dendrimers in the S 2p region under different pH.

Fig. 10 summarizes the change of the dendritic structure of pristine G5OH by APS treatment as well as the influence of pH on the dendritic structures of pristine G5OH and APS-G5OH. G5OH contains hydroxyl groups on its periphery as well as tertiary amines and amide functional groups on the pore surface. From the FT-IR and XPS results, the peripheral hydroxyl and amide nitrogen of the pore surface of G5OH are not affected by the APS treatment. However, the tertiary amine groups are protonated by APS treatment due to the falling of pH from 7.6 to 5.2, and, thus APS-G5OH fills with tertiary ammonium cations on the pore surface. The sulfur (VI and II) ions interact with these cations on the pore surface of APS-G5OH (**Fig. 10b**). The peripheral hydroxyl and amide nitrogen of both G5OH and APS-G5OH are not affected by the change in the pH. On the other hand, the tertiary amine groups of both G5OH and APS-G5OH are significantly affected by the change in the pH. The pH of the pristine G5OH is 7.2; therefore, G5OH is not protonated in an aqueous solution. Tertiary ammonium cations are formed by the protonation of the tertiary amine of G5OH, when the pH of the pristine G5OH solution is down to acidic condition. On the other hand, the tertiary ammonium cations of the pore surface of G5OH are deprotonated when the solution achieves a basic condition (**Fig. 10c**). A similar trend was observed in the case of APS-G5OH under acidic and basic conditions, similarly to the case of G5OH. The protonated tertiary amine groups of APS-G5OH due to the falling of pH by APS treatment which are deprotonated when the pH of the solution become to basic condition. The sulfur ions (VI and II) interact with APS-G5OH regardless of the change in the pH, as shown in **Fig. 10d**. Therefore, the enhancement in the fluorescence of APS-G5OH is most likely attributed the changes in the local environment of the branching units of the dendrimer molecules are summarized as follows. The formation of rigid, globular dendritic structures due to the strong charge–charge repulsions between tertiary ammonium cations [13] and the strong hydrogen bonding between $-\text{C}=\text{O}$ and $-\text{N}-\text{H}$ moieties in amide groups under acidic condition. Thus, the globular rigid-dendritic structure most likely exhibits strong fluorescence rather than vibrational relaxation [24].

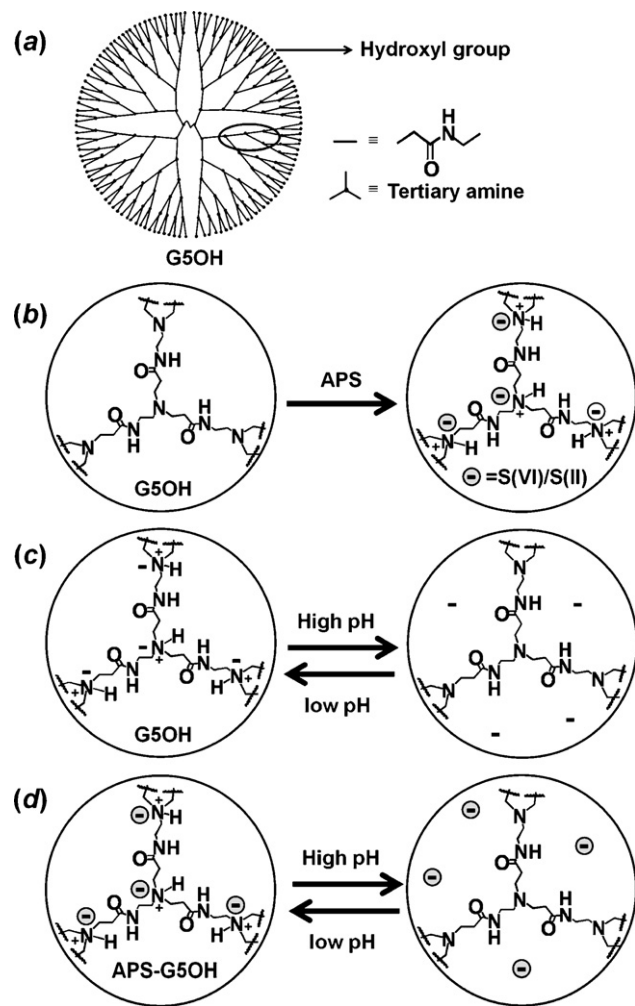


Fig. 10. (a) Structure of the ethylenediamine core G5OH dendrimer. The shaded area for the schematic illustration of the changes in the dendritic structures of G5OH dendrimer by APS treatment and at different pH is shown. (b) Schematic illustrations of the formation of APS-G5OH from G5OH by APS treatment. Schematic illustrations of pristine G5OH (c) and APS-G5OH (d) under acidic and basic conditions.

4. Conclusion

The dendritic structures of both pristine and APS-treated, hydroxyl-terminated, generation-five PAMAM dendrimers were examined at different pH. The pH of the APS-treated PAMAM dendrimer is 5.2, while that of the pristine PAMAM dendrimers is 7.6. No significant changes were observed for the peripheral hydroxyl or the amide nitrogen of PAMAM dendrimers by APS treatment. Tertiary ammonium cations were formed on the pore surface of the PAMAM dendrimer by protonation of tertiary amine groups during APS treatment as well as under acidic conditions; thus, the PAMAM dendrimer fills with tertiary ammonium cations (R_3NH^+ , $\text{R} = \text{CH}_2^-$) on the pore surface. Neither the peripheral hydroxyls nor the amide nitrogen of both pristine and APS-treated PAMAM dendrimers were significantly affected at any pH. Therefore, the formation of tertiary ammonium cations on the pore surface of the APS-treated PAMAM dendrimer is most likely involved in the fluorescence enhancement, while the weakly fluorescent pristine PAMAM dendrimer possesses tertiary amine groups on the pore surface.

Acknowledgement

The authors thank Mr. Koji Funaba, Nanotechnology Innovation Center, National Institute for Materials Science for his help with spectroscopic studies.

Appendix A. Supplementary data

Supplementary data associated with this article can be found, in the online version, at doi:10.1016/j.jphotochem.2011.09.012.

References

- [1] (a) G. Pistolis, A. Malliaris, C.M. Paleos, D. Tsiorvas, Study of poly(amidoamine) starburst dendrimers by fluorescence probing, *Langmuir* 13 (1997) 5870–5875; (b) D.A. Wade, P.A. Torres, S.A. Tucker, Spectrochemical investigations in dendritic media: evaluation of nitromethane as a selective fluorescence quenching agent in aqueous carboxylate-terminated polyamido amine (PAMAM) dendrimers, *Anal. Chim. Acta* 397 (1999) 17–31;
- (c) O. Varnavski, R.G. Ispasoiu, L. Balogh, D. Tomalia, T. Goodson III, Ultrafast time-resolved photoluminescence from novel metal-dendrimer nanocomposites, *J. Chem. Phys.* 114 (2001) 1962–1965;
- (d) C.L. Larson, S.A. Tucker, Intrinsic fluorescence of carboxylate-terminated polyamido amine dendrimers, *Appl. Spectrosc.* 55 (2001) 679–683.
- [2] (a) E.C. Wiener, S. Konda, A. Shadron, M. Brechbiel, O. Gansow, Targeting dendrimer-chelates to tumors and tumor cells expressing the high-affinity folate receptor, *Invest. Radiol.* 32 (1997) 748–754;
- (b) J.F. Kukowska-Latallo, K.A. Candido, Z. Cao, S.S. Nigavekar, I.J. Majoros, T.P. Thomas, L.P. Balogh, M.K. Khan, J.R. Baker, Nanoparticle targeting of anticancer drug improves therapeutic response in animal model of human epithelial cancer, *Cancer Res.* 65 (2005) 5317–5324;
- (c) I.J. Majoros, T.P. Thomas, C.B. Mehta, J.R. Baker, Poly(amidoamine) dendrimer-based multifunctional engineered nanodevice for cancer therapy, *J. Med. Chem.* 48 (2005) 5892–5899;
- (d) I.J. Majoros, A. Myc, T. Thomas, C.B. Mehta, J.R. Baker, PAMAM dendrimer-based multifunctional conjugate for cancer therapy: synthesis, characterization, and functionality, *Biomacromolecules* 7 (2006) 572–579.
- [3] S.H. Wang, X. Shi, M.V. Antwerp, Z. Cao, S.D. Swanson, X. Bi, J.R. Baker, Dendrimer-functionalized iron oxide nanoparticles for specific targeting and imaging of cancer cells, *Adv. Funct. Mater.* 17 (2007) 3043–3050.
- [4] L. Albertazzi, B. Storti, L. Marchetti, F. Beltram, Delivery and subcellular targeting of dendrimer-based fluorescent pH sensors in living cells, *J. Am. Chem. Soc.* 132 (2010) 18158–18167.
- [5] (a) M. Zhao, R.M. Crooks, Homogeneous hydrogenation catalysis with monodisperse, dendrimer-encapsulated Pd and Pt nanoparticles, *Angew. Chem. Int. Ed.* 38 (1999) 364–366;
- (b) K. Esumi, A. Suzuki, A. Yamahira, K. Torigoe, Role of poly(amidoamine) dendrimers for preparing nanoparticles of gold, platinum, and silver, *Langmuir* 16 (2000) 2604–2608;
- (c) R.M. Crooks, M. Zhao, L. Sun, V. Chechik, L.K. Yeung, Dendrimer-encapsulated metal nanoparticles: synthesis, characterization, and applications to catalysis, *Acc. Chem. Res.* 34 (2001) 181–190;
- (d) O.S. Alexeev, A. Siani, G. Lafaye, C.T. Williams, H.J. Ploehn, M.D. Amiridis, EXAFS characterization of dendrimer-Pt nanocomposites used for the preparation of Pt/γ-Al₂O₃ catalysts, *J. Phys. Chem. B* 110 (2006) 24903–24914;
- (e) N.N. Hoover, B.J. Auten, B.D. Chandler, Tuning supported catalyst reactivity with dendrimer-templated Pt-Cu nanoparticles, *J. Phys. Chem. B* 110 (2006) 8606–8612.
- [6] J. Zheng, J.T. Petty, R.M. Dickson, High quantum yield blue emission from water-soluble Au₈ nanodots, *J. Am. Chem. Soc.* 125 (2003) 7780–7781.
- [7] X.C. Wu, A.M. Bittner, K. Kern, Synthesis, photoluminescence, and adsorption of CdS/dendrimer nanocomposites, *J. Phys. Chem. B* 109 (2005) 230–239.
- [8] W.I. Lee, Y. Bae, A.J. Bard, Strong blue photoluminescence and ECL from OH-terminated PAMAM dendrimers in the absence of gold nanoparticles, *J. Am. Chem. Soc.* 126 (2004) 8358–8359.
- [9] (a) J.F. Gall, G.L. Church, R.L. Brown, Solubility of ammoniumpersulfate in water and in solutions of sulfuric acid and ammonium sulfate, *J. Phys. Chem.* 47 (1943) 645–649;
- (b) M. Mazur, Preparation of three-dimensional polymeric structures using gas bubbles as templates, *J. Phys. Chem. C* 112 (2008) 13528–13534;
- (c) A.A. Qaiser, M.M. Hyland, D.A. Patterson, Control of polyaniline deposition on microporous cellulose ester membranes by in situ chemical polymerization, *J. Phys. Chem. B* 113 (2009) 14986–14993.
- [10] (a) D. Wang, T. Imae, Fluorescence emission from dendrimers and its pH dependence, *J. Am. Chem. Soc.* 126 (2004) 13204–13205;
- (b) D. Wang, T. Imae, M. Miki, Fluorescence emission from PAMAM and PPI dendrimers, *J. Colloid Interface Sci.* 306 (2007) 222–227.
- [11] (a) A. Pevsner, M. Diem, Infrared spectroscopic studies of major cellular components. Part I: the effect of hydration on the spectra of proteins, *Appl. Spectrosc.* 55 (2001) 788–793;
- (b) D.S. Deutscher, A. Siani, P.T. Fanson, H. Hirata, S. Matsumoto, C.T. Williams, M.D. Amiridis, FT-IR investigation of the thermal decomposition of poly(amidoamine) dendrimers and dendrimer–metal nanocomposites supported on Al₂O₃ and ZrO₂, *J. Phys. Chem. C* 111 (2007) 4246–4255.
- [12] D.I. Malyarenko, R.L. Vold, G.L. Hoatson, Solid state deuteron NMR studies of polyamidoamine dendrimer salts. 1. Structure and hydrogen bonding, *Macromolecules* 33 (2000) 1268–1279.
- [13] (a) W. Chen, D.A. Tomalia, J.L. Thomas, Unusual pH-dependent polarity changes in PAMAM dendrimers: evidence for pH-responsive conformational changes, *Macromolecules* 33 (2000) 9169–9172;
- (b) M.H. Kleinman, J.H. Flory, D.A. Tomalia, N.J. Turro, Effect of protonation and PAMAM dendrimer size on the complexation and dynamic mobility of 2-naphthol, *J. Phys. Chem. B* 104 (2000) 11472–11479;
- (c) K. Funayama, T. Imae, K. Aoi, K. Tsutsumiuchi, M. Okada, M. Furusaka, M. Nagao, Small-angle neutron scattering investigations of layer-block dendrimers in aqueous solutions, *J. Phys. Chem. B* 107 (2003) 1532–1539.
- [14] (a) R.A. Nyquist, C.L. Putzig, M.A. Leugers, *Handbook of Infrared and Raman Spectra of Inorganic Compounds and Organic Salts*, Academic Press, San Diego, CA, 1997;
- (b) H. Siebner-Freibach, Y. Hadar, S. Yariv, I. Lapides, Y. Chen, Thermospectroscopic study of the adsorption mechanism of the hydroxamic siderophore ferrioxamine B by calcium montmorillonite, *J. Agric. Food Chem.* 54 (2006) 1399–1408;
- (c) M. Kumar, S. Singh, V.K. Shahi, Cross-linked poly(vinyl alcohol)-poly(acrylonitrile-co-2-dimethylamino ethylmethacrylate) based anion-exchange membranes in aqueous media, *J. Phys. Chem. B* 114 (2010) 198–206.
- [15] (a) D. Lin-Vien, N.B. Colthup, W.G. Fateley, J.G. Grasselli, *The Handbook of Infrared and Raman Characteristic Frequencies of Organic Molecules*, Academic Press, San Diego, CA, 1991;
- (b) R.M. Silverstein, R.C. Bassler, T.C. Morrill, *Spectroscopic Identification of Organic Compounds*, third ed., John Wiley and Sons, New York, 1991.
- [16] E.D. Guldin, L.R. Schindler, J.T. Roberts, Growth and characterization of sulfuric acid under ultrahigh vacuum, *J. Phys. Chem.* 99 (1995) 16059–16066.
- [17] (a) D. Liu, J. Gao, C.J. Murphy, C.T. Williams, In situ attenuated total reflection infrared spectroscopy of dendrimer-stabilized platinum nanoparticles adsorbed on alumina, *J. Phys. Chem. B* 108 (2004) 12911–12916;
- (b) O. Ozturk, T.J. Black, K. Perrine, K. Pizzolato, C.T. Williams, F.W. Parsons, J.S. Ratliff, J. Gao, C.J. Murphy, H. Xie, H.J. Ploehn, D.A. Chen, Thermal decomposition of generation-4 polyamidoamine dendrimer films: decomposition catalyzed by dendrimer-encapsulated Pt particles, *Langmuir* 21 (2005) 3998–4006.
- [18] (a) A. Manna, T. Imae, K. Aoi, M. Okada, T. Yogo, Synthesis of dendrimer-passivated noble metal nanoparticles in a polar medium: comparison of size between silver and gold particles, *Chem. Mater.* 13 (2001) 1674–1681;
- (b) G. Socrates, *Infrared and Raman Characteristic Group Frequencies*, Third ed., Wiley, Chichester, 2001.
- [19] G. Saravanan, H. Abe, Y. Xu, N. Sekido, H. Hirata, S. Matsumoto, H. Yoshikawa, Y. Yamabe-Mitarai, Pt₅Ti nanoparticles: fine dispersion on SiO₂ supports, enhanced catalytic CO oxidation, and chemical stability at elevated temperatures, *Langmuir* 26 (2010) 11446–11451.
- [20] (a) J. Charlier, V. Detalle, F. Valin, C. Bureau, G. Lécaon, Study of ultrathin polyamide-6,6 films on clean copper and platinum, *J. Vac. Sci. Technol. A* 15 (1997) 353–364;
- (b) A.J. Wagner, G.M. Wolfe, D.H. Fairbrother, Reactivity of vapor-deposited metal atoms with nitrogen-containing polymers and organic surfaces studied by in situ XPS, *Appl. Surf. Sci.* 219 (2003) 317–328.
- [21] (a) A. Adenier, M.M. Chehimi, I. Gallardo, J. Pinson, N. Vilà, Electrochemical oxidation of aliphatic amines and their attachment to carbon and metal surfaces, *Langmuir* 20 (2004) 8243–8253;
- (b) G. Zhai, W.H. Yu, E.T. Kang, K.G. Neoh, C.C. Huang, D.J. Liaw, Functionalization of hydrogen-terminated silicon with polybetaine brushes via surface-initiated reversible addition-fragmentation chain-transfer (RAFT) polymerization, *Ind. Eng. Chem. Res.* 43 (2004) 1673–1680;
- (c) M. Datta, H.J. Mathieu, D. Landolt, Characterization of transpassive films on nickel by sputter profiling and angle resolved AES/XPS, *Appl. Surf. Sci.* 18 (1994) 299–314.
- [22] M.S. Diallo, K. Falconer, J.H. Johnson Jr., W.A. Goddard III, Dendritic anion hosts: perchlorate uptake by G5-NH₂ poly(propyleneimine) dendrimer in water and model electrolyte solutions, *Environ. Sci. Technol.* 41 (2007) 6521–6527.
- [23] R. Graupner, J. Abraham, A. Venczelová, T. Seyller, F. Henrich, M.M. Kappes, A. Hirsch, L. Ley, Doping of single-walled carbon nanotube bundles by Bronsted acids, *Phys. Chem. Chem. Phys.* 5 (2003) 5472–5476.
- [24] (a) B. Valeur, *Molecular Fluorescence: Principles and Applications*, Wiley-VCH, Verlag GmbH, Weinheim, Germany, 2001;
- (b) Y. Lin, J.-W. Gao, H.-W. Liu, Y.-S. Li, Synthesis and characterization of hyperbranched poly(ether amide)s with thermoresponsive property and unexpected strong blue photoluminescence, *Macromolecules* 42 (2009) 3237–3246.

Supplementary data

Influence of pH on Dendritic Structure of Strongly Fluorescent Persulfate-treated Poly(amidoamine) Dendrimer

Govindachetty Saravanan* and Hideki Abe*

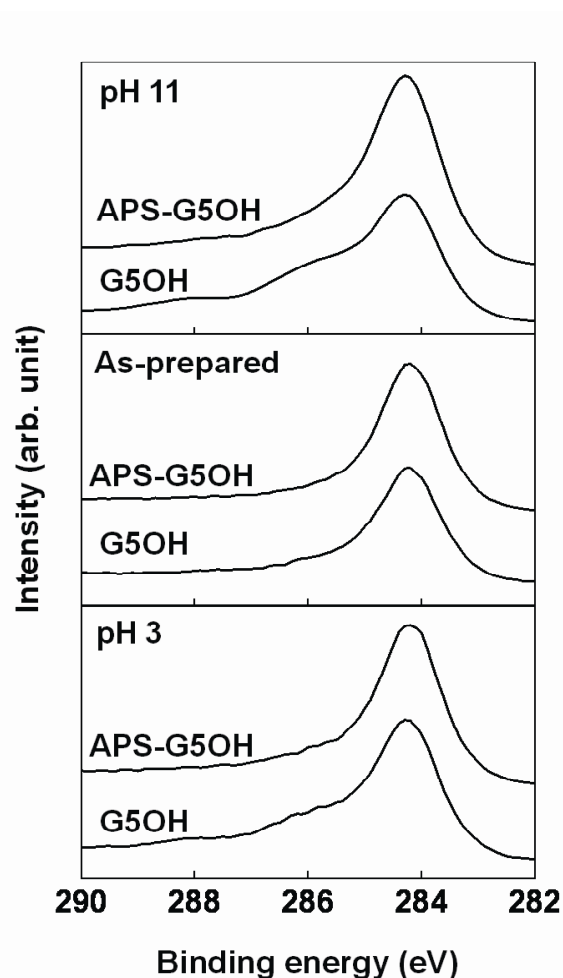


Fig S1. XPS profiles for as-prepared G5OH and APS-G5OH films in the C1s region.

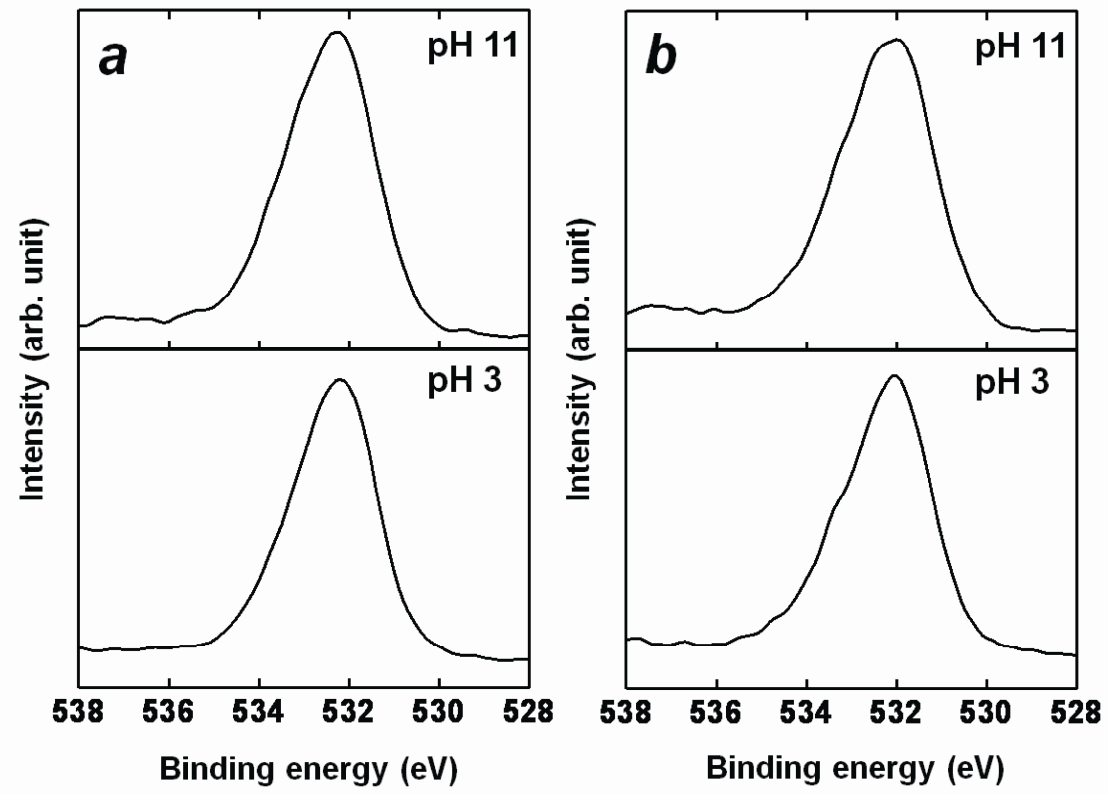


Fig S2. XPS profiles for G5OH and APS-G5OH in the O 1s regions at pH 3 and 11.

Visual Observation and Characterization of Fluorescent Poly(amido amine) Dendrimer in Film State

Govindachetty Saravanan¹ and Toyoko Imae^{1, 2,*}

¹Graduate School of Science and Technology, Keio University, Hiyoshi, Yokohama 223-8522, Japan

²Graduate Institute of Engineering, National Taiwan University of Science and Technology,
Section 4, Taipei 10607, Taiwan

The fluorescent property of PAMAM dendrimers were examined at film state rather than in solution. The O₂-treated PAMAM dendrimer displayed strong blue fluorescence due to its conservation of luminance in the film state and diminished its intensity with degas. The fluorescent property of PAMAM dendrimers was utilized as a fluorescent probe on functional patterned substrates for visual observation by a fluorescence microscope. G4 and G4.5 PAMAM dendrimers having peripheral groups of functional amine and carboxylate, respectively, were adsorbed selectively by electrostatic interactions on patterned carboxylic acid and amine terminated surfaces, respectively resulting in strong fluorescent patterns. This suggests the possible application of fluorescent PAMAM dendrimers as a fluorophor for the visualizable reactions. It was confirmed from an X-ray photoelectron spectroscopy that O₂ molecules interact with tertiary amine moiety in PAMAM dendrimers but not amide group. These results give us an important support for the principle of fluorescence phenomenon.

Keywords: Patterned Poly(amido amine) Dendrimer Film, Fluorescence Microscope, X-ray Photoelectron Spectroscopy.

1. INTRODUCTION

The family of poly(amido amine) (PAMAM) dendrimer can be used to monitor the properties of biomaterials owing to its well-characterized architecture, biocompatibility, nonimmunogenicity, and water-solubility.¹ Number of studies about molecular assemblies of PAMAM dendrimers on various solid substrates are carried out by adsorption, self-assembled monolayer (SAM) and patterning techniques where the various peripheral groups ($-OH$, $-COOH$, $-NH_2$) of PAMAM dendrimers having high reactivity selectively bind to the functional substrates.^{2–9} The SAM of dendrimers has been used as a DNA (or polyelectrolyte) detector and a biochemical sensor based on polyelectrolyte-ligand interaction.^{10–13} The molecular assemblies of PAMAM dendrimers have also been patterned by techniques of microcontact printing,^{14–17} scanning probe lithography¹⁸ and photolithography,¹⁹ which were examined by atomic force microscopy, scanning electron microscopy, etc. However, there are no reports of visual observation on selective adsorption of PAMAM dendrimers on solid substrates.

It has been found that the family of aged or O₂-treated PAMAM dendrimer emits blue photoluminescence under excitation around 360 nm. The fluorescence of PAMAM dendrimers and their derivatives or analogs has been studied by some research groups.^{20–33} Therefore, it is expected that when the target materials are selectively labeled by fluorescent PAMAM dendrimer as a fluorescent probe, one is allowed to investigate properties and assembling of the objective materials by simple fluorescence technique. Incidentally, the visualization by a fluorescence microscopy has been carried out on PAMAM dendrimer-dyed fibers and dendritic nanohydrogels of PAMAM Dendron.^{28–29} Additionally, it can be noticed that the current investigation of photoluminescence for the family of PAMAM dendrimer has been carried out only in solution.

In the present work, the selective adsorption of fluorescent G4 and G4.5 (G: generation) PAMAM dendrimers on patterned SAM substrates with different affinities to dendrimers is visually detected by a fluorescence microscopy. SAM preparation and photolithography are used to create the functional substrates with carboxylic acid- or amine-terminated pattern along with methyl-terminated pattern. Subsequently, the fluorescent property of dendrimers in a solid state on the substrates is successfully investigated

*Author to whom correspondence should be addressed.

under gas/degas process of oxygen. The present work indicates the extensive possibility for family of PAMAM dendrimer to be utilized even at the solid film as a fluorescence probe on the microscopic observation. Moreover, facile and highly sensitive detection of fluorescent dendrimer probe on a fluorescence microscope is the strong advantage on the various biomedical applications, sensing technology and molecular recognition.

2. EXPERIMENTAL DETAILS

2.1. Materials

Methanol solutions of G4 and G4.5 PAMAM dendrimers (PAMAM-NH₂, PAMAM-COO) were purchased from Aldrich Co., Ltd. These dendrimers contain 64 (amine) and 128 (carboxylate) terminal groups, respectively. *n*-octadecyltrimethoxysilane (ODS), 3-aminopropyltriethoxysilane (APS) and ammoniumpersulfate ((NH₄)₂S₂O₈) were obtained from Tokyo Chemical Industries, Co., Ltd., Acros Organics Co., Ltd, and Wako Chemicals Co., Ltd, respectively. Ethanol and toluene were products from Junsei Chemical Co., Ltd. Purified water was prepared by a Millipore milli-Q system.

2.2. Preparation

Silicon and glass substrates (Matsunami micro cover glass, 18 × 18 mm) were patterned by SAM procedure and photolithography.^{19,34} Prior to the patterning on silicon or glass substrate, the substrates were carefully cleaned by ultrasonication for 5 min each in piranha solution, water, acetone, and ethanol, followed by drying in an oven. The substrates were further cleaned photochemically by irradiation of UV light in vacuum which is generated from an excimer lamp (Ushio Electric UER20-172V, $\lambda = 172$ nm with a power density of 10 mWcm⁻²) in order to remove any organic contaminants. The UV irradiation was carried out at a pressure of 1.5×10^2 pa with a proximate gap of <10 nm between the substrate and photomask. The radiation at short wavelength produces the oxygen atoms and ozone molecules from atmospheric oxygen molecules by photoexcitation, which decompose the carbon–carbon and carbon–hydrogen bonds of organic molecules.³⁵

Two different types of precursors, ODS and APS, were employed for the preparation of carboxylic acid and amine terminated patterns, respectively. The carboxylic acid (ODS-COOH) and amine (ODS-NH₂) terminated patterns were immersed in a 0.5 mM solution of G4 or G4.5 PAMAM dendrimer for 24 h and thus the dendrimer-treated substrates were denoted by PAMAM-NH₂/ODS-COOH, PAMAM-COO⁻/ODS-COOH, PAMAM-NH₂/ODS-NH₂, and PAMAM-COO⁻/ODS-NH₂. Prior to the immersion of these substrates, solutions of PAMAM dendrimers were aged for 7 days under the addition of an aqueous 0.1 M solution

of ammoniumpersulfate. The dendrimer-treated substrates were dried by N₂ gas and then examined by optical and fluorescence microscopy.

The G4 and G4.5 PAMAM dendrimer films on well-cleaned quartz and silicon (*n* type (100) wafer, Nilaco Co.) substrates were prepared from 50 mm³ of a 5 wt% PAMAM dendrimer solution by a spin coating method where the substrates were rotated at 100 rpm for 5 min. This process was repeated for four times and then the films were dried overnight at room temperature under vacuum. PAMAM dendrimer films on substrates were aged in the presence of O₂ gas and degassed. Then the films were analyzed by UV-visible absorption spectroscopy, fluorescence spectroscopy and X-ray photoelectron spectroscopy (XPS).

2.3. Measurements

UV-visible absorption spectra on quartz substrates were collected on a Shimadzu Bio Spec-1600 spectrometer. Fluorescence spectra were recorded on a Hitachi F-3010 fluorescence spectrophotometer, where the excitation source was Xenon lamp operated at 150 W. The optical (Halogen lamp, LHS-H100P-1, 12 V, 100 W) and fluorescence (super high pressure mercury lamp, Model C-SHG1, 100 W) microscopic images were taken on a Nikon-Eclipse TE 2000-U microscope. For fluorescence microscopic images, the silicon substrates were irradiated at 365 nm excitation wavelength by using DM 400 and RA 400 filters. XPS studies on quartz substrates were performed on a JPS-9000 MX JEOL photoelectron spectrometer using MgK α monochromatized X-ray beam at a constant dwell time of 100 ms. X-ray scans were performed by using pass energies of 50 eV for wide scan and of 10 eV for narrow scan. The anode voltage and current were 10 kV and 10 mA, respectively. All core level spectra were obtained at a photoelectron takeoff angle of 90° with respect to the PAMAM dendrimer films.

3. RESULTS AND DISCUSSION

3.1. Visual Observation of G4 and G4.5 PAMAM Dendrimers on ODS-COOH and ODS-NH₂ Patterned Substrates

The functional patterned substrates allow us to investigate the properties and assembling of materials and can be used for various applications like sensing technologies, organic light-emitting diodes, organic thin-film transistors, etc.^{36–41} Moreover, they can be model surfaces of biomaterials which are prepared readily by a large variety of available techniques.^{42,43} The substrates with –NH₂ or –COOH surface pattern along with methyl surface pattern are ones of model surfaces of biomaterials. The fluorescent G4 and G4.5 PAMAM dendrimers possessing –NH₂ and –COO⁻ functional groups, respectively, on their periphery can be expected to be adsorbed selectively on these model

surfaces. The fluorescent PAMAM dendrimers were pre-treated by adding an aqueous 0.1 M $(\text{NH}_4)_2\text{S}_2\text{O}_8$ solution and used throughout the patterning experiments, because this treatment enhances the fluorescence of PAMAM dendrimers even at very short time process.²⁵ Figure 1 shows the comparison of fluorescence intensity of persulfate-treated and untreated G4 PAMAM dendrimer on silicon substrate which was prepared by spin-coating dendrimer in water (0.5 mM) at 10 rpm for five times. The persulfate-treated dendrimer displayed a strong blue fluorescence emission band at 452 nm at excitation wavelength of 360 nm and an excitation band at 370 nm at emission wavelength of 452 nm. The fairly strong fluorescence intensity of persulfate-treated dendrimer superior to untreated one indicates the conservation of luminescence even at the film state.

Figure 2 denotes the procedure for the selective adsorption of PAMAM dendrimer on methyl/carboxylic acid terminated patterned silicon substrates. For this purpose, the well-cleaned silicon substrates were put together with a few drops (0.2 cm^3) of ODS liquid in a Teflon container, which was covered tight with a lip and then retained in an oven at 150°C for 3 h. The formation of ODS SAMs on substrates was examined by contact angle of pure water; the silicon substrate terminated with methyl groups brought about a highly hydrophobic contact angle at $86 \pm 2^\circ$. The carboxylic acid pattern was prepared as rectangular closed area by exposing an ODS SAM substrate to UV light for 100 s under photo mask in the presence of oxygen gas. Then alkyl groups of ODS out of the photo mask underwent partial oxidation on the exposure process through UV light and were decomposed into

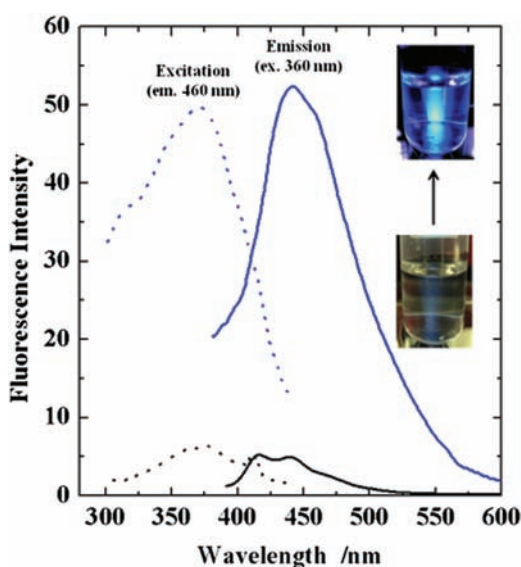


Fig. 1. Fluorescence spectra of pristine (black) and persulfate-treated (blue) G4 PAMAM dendrimer films on a silicon substrate. Insets are photos of 0.5 mM G4 PAMAM dendrimer solutions before preparing films.

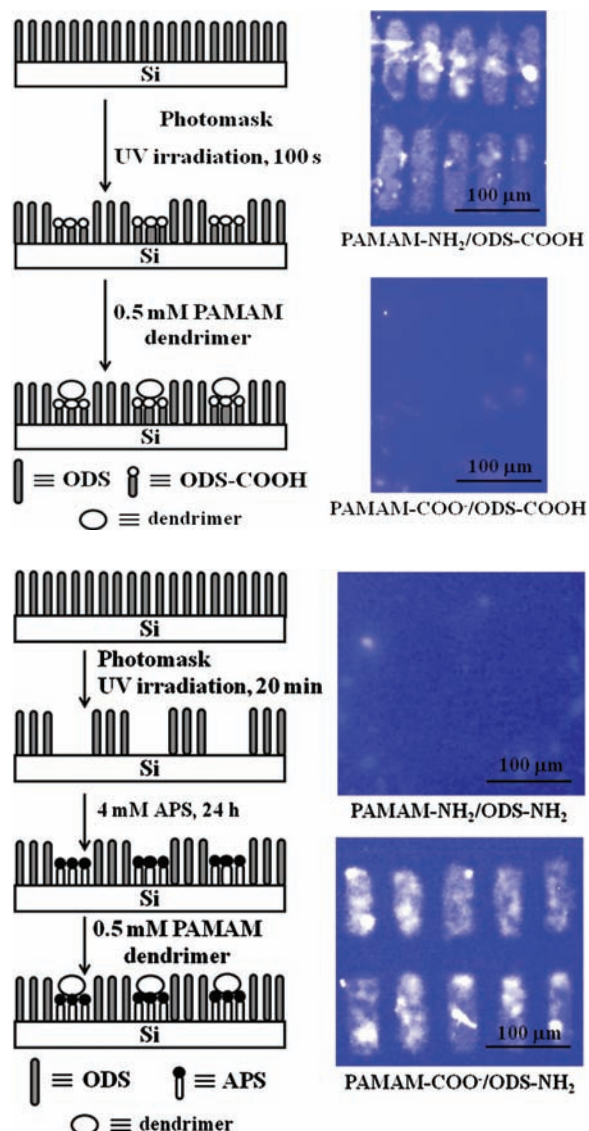


Fig. 2. A scheme of the pattern preparation on ODS SAM on a silicon substrate and the adsorption of PAMAM dendrimers on it. Photographs indicate fluorescence microscopic images after the adsorption procedure of G4 and G4.5 PAMAM (PAMAM-NH_2 , PAMAM-COO^-) dendrimers. (top) Carboxylic acid pattern on an ODS SAM (ODS-COOH); (bottom) Amine pattern on an ODS SAM (ODS-NH₂).

carboxylic acidterminated pattern,^{19,44,45} which resulted in the ODS-COOH patterned substrate with ODS frame. The water contact angle of the resultant substrate was $64 \pm 2^\circ$.

After the adsorption of G4 PAMAM dendrimer, as shown in Figure 2, the fluorescence microscopic image of the substrate at excitation wavelength of 365 nm displayed strong fluorescent pattern with two distinct regions, that is, the dark frame and the bright fluorescent rectangles. The dark frame is indicative of the ODS SAM without adsorption of dendrimer, because amine-terminated G4 PAMAM dendrimer does not adsorb on methyl-terminated pattern. Whereas, the clear and well-defined fluorescent region suggests the adsorption of fluorescent G4 PAMAM

dendrimer, since the peripheral amine groups of G4 PAMAM dendrimer bind on carboxylic acid-terminated substrate. Then the binding interaction should be electrostatic, because the adsorption process was carried out in water at neutral pH where amine and carboxylic acid are protonated and deprotonated, respectively.

The reverse effect is also expected i.e., G4.5 PAMAM dendrimer (with $-COOH$ peripheral groups) will interact with amine-terminated substrate. Figure 2 shows the procedure for preparation of APS SAM pattern on ODS SAM substrate. The ODS SAM substrate loaded photo mask was irradiated by UV light for 20 min in the presence of oxygen so as to remove completely ODS SAM from the unmasked area.⁴⁵ The APS SAM was introduced on the ODS-removed pattern by immersion of patterned ODS substrates for 24 h in a 4 mM toluene solution of APS. Thus the resultant patterned substrate of ODS and APS ($ODS-NH_2$) was washed with toluene and ethanol, dried under N_2 atmosphere and maintained for 1 h at 120 °C in oven. Then G4.5 PAMAM dendrimers were adsorbed on the $ODS-NH_2$ patterned substrate. As expected, strong fluorescent pattern was displayed, as shown in Figure 2. The bright rectangular region is an outcome of an effective interaction between $-COOH$ peripheral groups of G4.5 PAMAM dendrimers and NH_2 terminated pattern on the substrate. However, the dark frame region suggests that no such interaction was observed between G4.5 PAMAM dendrimer and methyl-terminated group of ODS SAM on the substrate.

The results described above indicate that the electrostatic interaction is a main driving force of the selective

adsorption of dendrimers on the patterned substrates. In order to make sure this conclusion, the adsorption behavior of G4.5 PAMAM dendrimer on ODS-COOH or G4 PAMAM dendrimer on ODS-NH₂ was examined. As seen in Figure 2, distinct bright regions were not observed for both combinations, suggesting no considerable attraction between dendrimer and patterned substrate in this combination. Additionally, it can be insisted that the fluorescence microscopic observation is the highly excellent technique to detect the existence of PAMAM dendrimers on the selected area, since the distinction by the optical microscopic images is not easy for the dendrimers on glass substrates, which are prepared by the procedure same as that on silicon substrates, as shown in Figure 3.

3.2. Effect of O_2 Gas on G4 and G4.5 PAMAM Dendrimer in Film State

Different from previous works which were done in solutions,^{13, 19, 24–26, 46} dendrimers in the film state provide us the solvent-free fluorescence behavior and the outright evaluation on the structural aspect of PAMAM dendrimers during aging under O_2 gas. Figure 4 shows emission fluorescence spectra for G4.5 PAMAM dendrimer film on a silicon substrate which was aged under O_2 gas at various time intervals. When the substrate was irradiated at 360 nm, a strong emission band was observed at 435 nm, and its intensity increased with increasing aging time. The same trend was also found in excitation fluorescence spectra: The strong excitation band was observed at 370 nm and intensified with increasing aging time at the emission of 460 nm, as shown in Figure 4. These results support

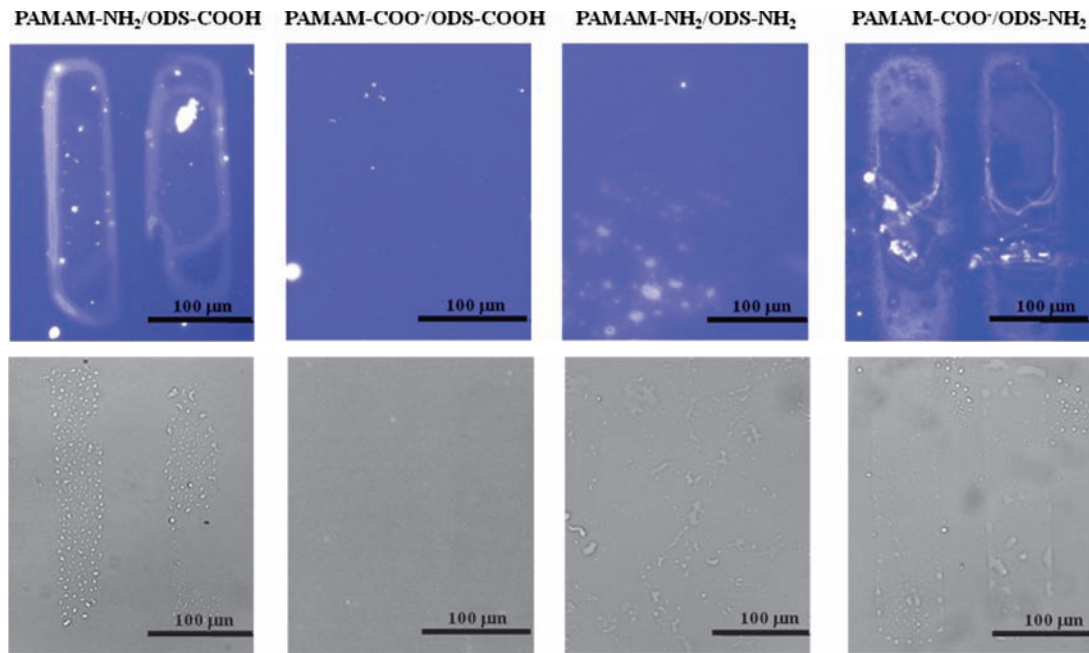


Fig. 3. Fluorescence (top) and optical (bottom) microscopic images of PAMAM-NH₂/ODS-COOH, PAMAM-COO⁻/ODS-COOH, PAMAM-NH₂/ODS-NH₂, PAMAM-COO⁻/ODS-NH₂.

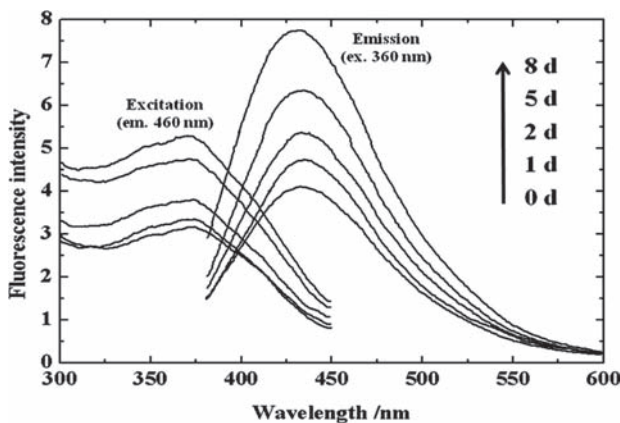


Fig. 4. Fluorescence spectra of a G4.5 PAMAM dendrimer film on a silicon substrate at different aging time under O_2 gas atmosphere.

that O_2 molecules are doped within PAMAM dendrimer in the film and participate in the enhancement of the fluorescence intensity.

O_2 -treated PAMAM dendrimer films were overnight subject to vacuum condition in order to ensure the enhanced fluorescence property through doping O_2 . The emission fluorescence intensity of O_2 -treated G4.5 PAMAM dendrimer films decreased after vacuum treatment, as shown in Figure 5(top). As with the emission fluorescence intensity, the excitation fluorescence intensity also decreased after vacuum treatment. The similar trends on fluorescence variation were found again for G4 PAMAM dendrimer films, as seen in Figure 5(bottom). It should be noticed that the successive gas/degas process on G4 PAMAM dendrimer films reproduced the increase/decrease behavior of emission and excitation intensities (see Fig. 5(bottom, inset)). These results clearly indicate that O_2 molecules are doped within PAMAM dendrimer films by noncovalent binding to enhance the fluorescence property of PAMAM dendrimers.

According to the successive UV-visible absorption spectra for a G4.5 PAMAM dendrimer film on quartz substrate which was aged in the presence of O_2 gas at various time intervals as shown in Figure 6, an absorption band (maybe, assigned to $n-\pi^*$ transition) was observed at 286 nm and intensified systematically with increasing aging time. Since the present experiments were carried out at solvent-free, this variation in the absorption band is the intrinsic behavior of PAMAM dendrimer. Therefore, it should be noticed that the local configuration of PAMAM dendrimer in the film may be changed during aging process under O_2 atmosphere. However, it must also be recognized that the position of the absorption band is lower than that of the excitation band.

The pristine and O_2 -treated PAMAM dendrimer films on quartz substrate were examined further by high resolution XPS in order to investigate the influence of O_2 gas on the enhancement of fluorescence. High resolution spectra were recorded for the main core level peaks of C, N, and

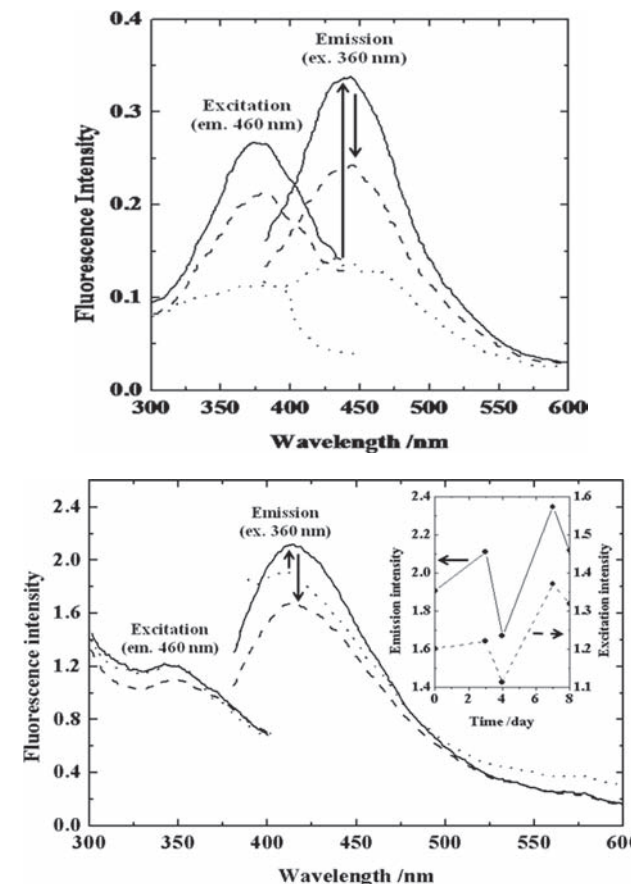


Fig. 5. Fluorescence spectra of PAMAM dendrimer films on a silicon substrate. Dotted line: pristine, solid line: O_2 -treated (3 d), dashed line: degas-treated (overnight in vacuum). (top) G4.5, (bottom) G4. An inset is a plot of fluorescence intensity variation during two cycles of the O_2 -and degas-treatments.

O and exemplified in Figure 7. The XPS was deconvoluted into component peaks and resultant data are summarized in Table I. The C1s region of a G4 PAMAM dendrimer film revealed clearly the different chemical states of carbon

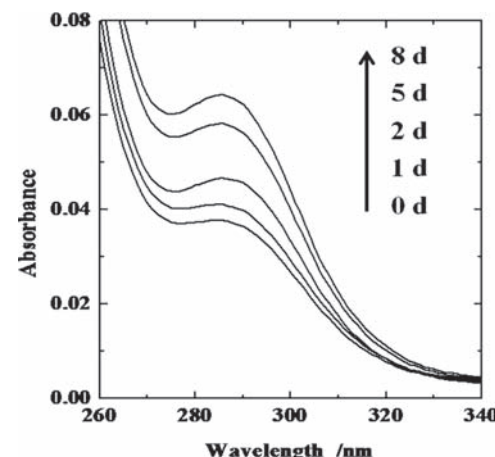


Fig. 6. UV-visible absorption spectra of a G4.5 PAMAM dendrimer film on a quartz substrate at different aging time under O_2 gas atmosphere.

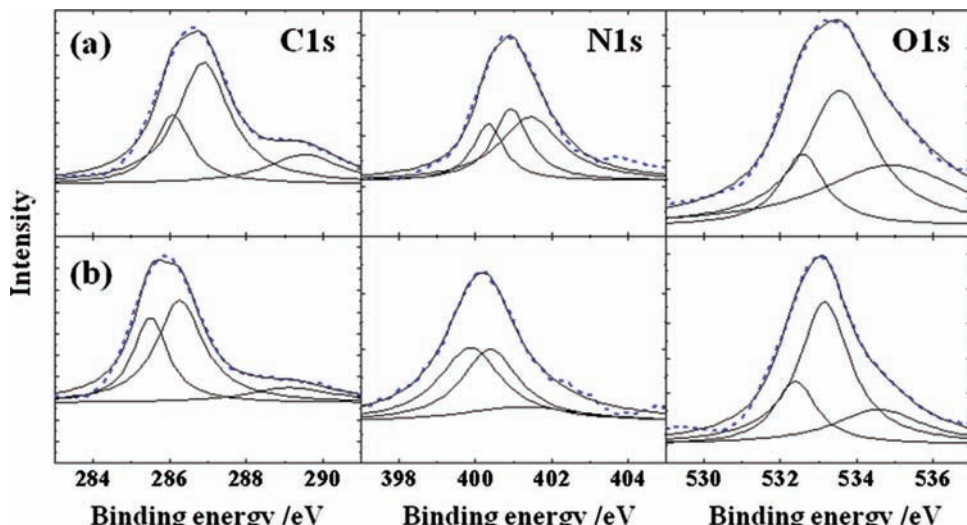


Fig. 7. Observed XPS of G4 PAMAM dendrimer films on a quartz substrate and deconvolution of C1s, N1s, and O1s peaks. (a) Pristine; (b) O₂-treated (8 d).

(see Fig. 7 and Table I).^{47,48} The component peaks were obtained at binding energies of 286.1 (C=C=O), 286.9 (C–N), and 289.6 (C=O) eV for the pristine G4 PAMAM dendrimer film. The binding energy of C–N peak was considerably lowered to 285.6 eV after aged at O₂ atmosphere, while the binding energies of C=C=O and C=O peaks remained in the almost same energy. Changes were also observed in the N1s region for G4 PAMAM dendrimer film. The N1s spectra can be deconvoluted into three component peaks at the binding energies of 400.4 (N–H₂), 401.0 (N–C), and 401.5 (NH–C=O) eV. The amide nitrogen exists at higher binding energy than primary and tertiary amine nitrogen, since amide nitrogen bears the partial positive charge because of its resonance structure. Although the binding energies of the primary amine and amide nitrogen were not changed by O₂-treatment, the energy of the tertiary amine nitrogen shifted 1.2 eV and observed at 399.8 eV. In the broad O1s spectra for PAMAM dendrimer films, the O1s peak of the amide oxygen was observed at 533.3 eV and did not vary even after O₂-treatment. However, the peak of pristine dendrimer film at 535.0 eV lowered down to 534.4 eV after O₂-treatment. The third peak was observed at the binding energy of 532.6 eV, although the energy is scarcely susceptible for O₂-treatment. While both peaks at 535.0 and 532.6 eV are not assigned to oxygen in PAMAM dendrimer, the O1s

peaks of surface oxide and hydroxyl of quartz substrate appear in this region. Then, it is difficult to distinguish the peaks of surface oxide or hydroxyl groups on quartz and those of other chemical states of oxygen such as free O₂ or H₂O, as previously reported.^{48,49} Figure 8 displays XPS of a G4 PAMAM dendrimer film on a silicon substrate at different aging time under O₂ gas atmosphere. It is consistent with the results in Figure 7 that the C, N, and O peaks varied to lower binding energies with aging. However, it should be noticed that the remarkable variation of binding energy occurred after aging for three days, although the detectable change in fluorescence intensity was observed even after aging for one day under O₂ gas.

The XPS of G4.5 PAMAM dendrimer films behaved like that of G4 PAMAM dendrimer films on the effect of O₂-treatment (see Table I). Differently from invariable C1s peaks of C=C=O (286.9 eV) and C=O (289.6 eV), a C–N (287.3 eV) peak shifted to 286.2 eV. In the N1s region, while the peaks for tertiary amine and amide nitrogen were observed at the binding energy of 401.1 and 401.3 eV, respectively, the binding energy of tertiary amine nitrogen shifted to 400.5 eV but there was no considerable shift for amide nitrogen after the O₂-treatment. For the O1s region, the peaks at the binding energies of 532.5 eV (C–OH) and 533.1 eV (C=O) were invariable for both pristine and aged G4.5 PAMAM dendrimer film.

Table I. XPS peaks of pristine and O₂-treated G4 and G4.5 PAMAM dendrimer films (number: binding energy in eV).

PAMAM dendrimer film	C1s			N1s			O1s		
	C=C=O	C–N	C=O	NH ₂	–N<	O=C–NH	OH	C=O	
Pristine G4	286.1	286.9	289.6	400.4	401.0	401.5	532.6	533.3	535.0
O ₂ -treated G4	286.2	285.6	289.5	400.4	399.8	401.4	532.5	533.2	534.4
Pristine G4.5	286.9	287.3	289.6	—	401.1	401.3	532.5	533.1	535.0
O ₂ -treated G4.5	287.0	286.2	289.6	—	400.5	401.1	532.4	533.1	534.1

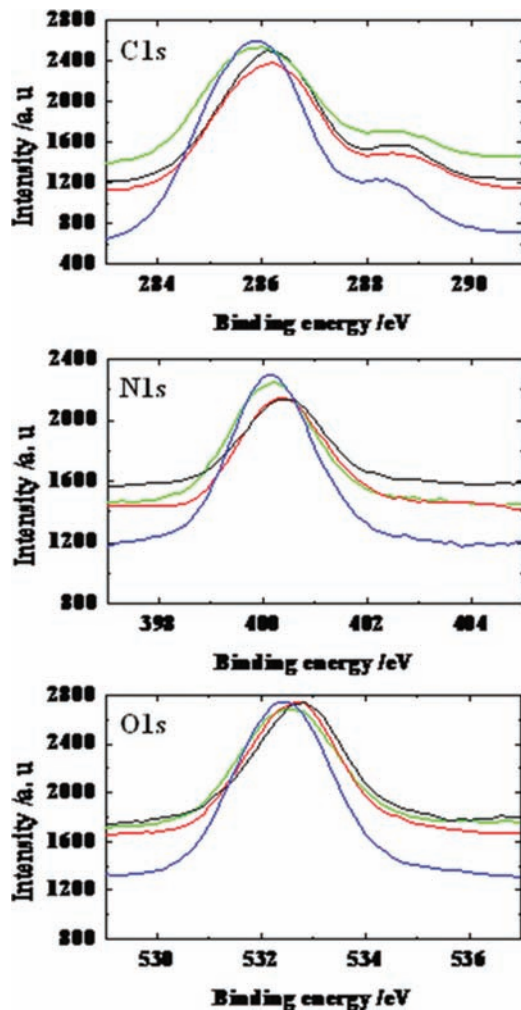
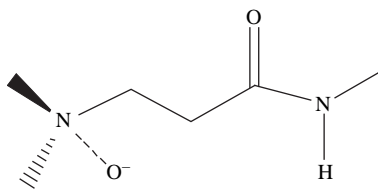


Fig. 8. Observed XPS of a G4 PAMAM dendrimer film on a silicon substrate at different aging time under O_2 gas atmosphere. Aging time: pristine (red), 3 d (black), 6 d (green), 20 d (blue).

The binding energy at 535.0 eV of the pristine film lowered into 534.1 eV after O_2 -treatment.

The PAMAM dendrimer consists of three different components, such as amide spacer, tertiary amine, and peripheral $-COO^-$ or $-NH_2$ (in the case of G4.5 and G4 PAMAM dendrimers, respectively) functional groups in their chemical structure. Then the XPS examination allows us to estimate the effect of O_2 treatment at atomic level. The XPS results for G4 and G4.5 PAMAM dendrimers are summarized in common as follows:

- (1) The binding energies of carbon, nitrogen and oxygen in amide and primary amine are not affected by the O_2 -treatment.
- (2) The binding energies of carbon and nitrogen in tertiary amine are lowered on the process of the O_2 -treatment.
- (3) Besides peaks from PAMAM dendrimer, the additional component peak of O1s is observed at 535.0 eV and it is lowered after the O_2 -treatment, suggesting the existence of other chemical states of oxygen, e.g., O_2



Scheme 1. Schematic representation of O_2 -encapsulated, branched element of PAMAM dendrimer unit. O_2 molecules attack the tertiary amine moiety rather than the amide spacer moiety.

in the PAMAM dendrimer film. Then it is assumed that the tertiary amine moiety in the PAMAM dendrimer is attacked by O_2 as illustrated in Scheme 1 and, as a result, that the binding energies of tertiary amine moiety and O_2 are lowered, that is, the binding are stabilized. These results seem to be consistent with previous reports that tertiary amine should be a common moiety of PAMAM and related dendrimers with blue photoluminescence phenomenon,⁴⁶ that is, the family of PAMAM dendrimers with different terminal moieties ($-OH$, $-COOH$, $-NH_2$, etc.),^{25, 26, 29} poly(alkyleneimine) dendrimers,^{31, 32} poly(amino ester) dendrimers,²⁷ poly(propyl ether imine) dendrimer,³³ polyethyleneimine³⁰ and triethylamine.⁴⁶

4. CONCLUSIONS

Fluorescent G4 and G4.5 PAMAM dendrimers were characterized at film state. O_2 -treated PAMAM dendrimer films displayed the luminescence which was detected by excitation and emission spectra. Selective adsorption of fluorescent PAMAM dendrimers on hydrophilic/hydrophobic patterned substrates was determined by means of a fluorescence microscope. It was conformed from strong luminescence on corresponding pattern that the peripheral $-NH_2$ and $-COOH$ functional groups of G4 and G4.5 PAMAM dendrimers, respectively, were selectively adsorbed on carboxylic acid and amine terminated patterns, respectively by strong electrostatic interaction. However, no such fluorescence patterns were observed, if there were no strong interactions between PAMAM dendrimers and functionalized substrates. Luminescence intensity changed with O_2 filling and degas, indicating the nonchemical binding of O_2 with dendrimer. It could be newly mentioned from XPS that O_2 -treatment affected tertiary amine moiety but not amide group in the PAMAM dendrimers.

Obviously, the present results suggest that the luminescent behavior occurs not only in solution but also even at film state. Moreover, the direct discovery of the affect of O_2 on tertiary amine in PAMAM dendrimer allows us to confirm previous assumption⁴⁶ for the luminescence mechanism of PAMAM dendrimers. The attractive features of the present technique are the simplicity, reproducibility, and sensitivity on the detection of the selective

adsorption of PAMAM dendrimers on functionalized substrates. Further, the fluorescent property of PAMAM dendrimers utilized through the present procedure is highly effective, suggesting that family of PAMAM dendrimers can be used to label and monitor the target systems as fluorophor. Especially, the fluorescent PAMAM dendrimers, which are nontoxic, can be selectively labeled to the functionalized systems such as biomaterials and valuably utilized as a sensor of selective molecular recognition in medical therapy and testing.

Acknowledgment: This work was financially supported in part by Japan-Taiwan Joint Research Program of Interchange Association, Japan.

References and Notes

1. A. K. J. Patri, U. J. Majoros, and J. Baker, *J. Curr Opin Chem Biol.* 6, 466 (2002).
2. S. Rubin, G. Bar, T. N. Taylor, R. W. Cutts, J. Zawodzinski, and A. Thomas, *J. Vac. Sci. Technol. A* 1870 (1996).
3. G. Bar, S. Rubin, R. W. Cutts, T. N. Taylor, J. Zawodzinski, and A. Thomas, *Langmuir* 12, 1172 (1996).
4. S. A. Evenson and J. P. S. Badyal, *Adv. Mater.* 9, 1097 (1997).
5. H. Tokuhisa, M. Zhao, L. A. Baker, V. T. Phan, D. L. Dermody, M. E. Garcia, R. F. Peez, R. M. Crooks, and T. T. Mayer, *J. Am. Chem. Soc.* 120, 4492 (1998).
6. L. A. Baker, F. P. Zamborini, L. Sun, and R. M. Crooks, *Anal. Chem.* 71, 4403 (1999).
7. K. M. A. Rahman, C. J. Durning, N. J. Turro, and D. A. Tomalia, *Langmuir* 16, 10154 (2000).
8. J. Li, D. Qin, J. J. R. Baker, and D. A. Tomalia, *Polym. Prepr.* 41, 1446 (2000).
9. M. Ito, T. Imae, K. Aoi, K. Tsutsumiuchi, H. Noda, and M. Okada, *Langmuir* 18, 9754 (2002).
10. H. C. Yoon, M.-Y. Hong, and H.-S. Kim, *Langmuir* 17, 1234 (2001).
11. M.-Y. Hong, H. C. Yoon, M.-Y. Hong, and H.-S. Kim, *Langmuir* 19, 416 (2003).
12. E. Kim, K. Kim, H. Yang, Y. T. Kim, and J. Kwak, *Anal. Chem.* 75, 5665 (2003).
13. T. Yamazaki and T. Imae, *J. Nanosci. Nanotech.* 5, 1066 (2005).
14. D. Arrington, M. Curry, and S. C. Street, *Langmuir* 18, 7788 (2002).
15. H. Li, D. J. Kang, M. J. Blamire, and E. T. S. Huck, *Nano Lett.* 2, 347 (2002).
16. X. C. Wu, A. M. Bittner, and K. Kern, *Langmuir* 18, 4984 (2002).
17. A. M. Bittner, X. C. Wu, and K. Kern, *Adv. Funct. Mater.* 12, 432 (2002).
18. R. McKendry, W. T. S. Huck, B. Weeks, M. Fiorini, C. Abell, and T. Rayment, *Nano Lett.* 2, 713 (2002).
19. T. Yamazaki, T. Imae, H. Sugimura, N. Saito, K. Hayashi, and O. Takai, *J. Nanosci. Nanotechnol.* 5, 1792 (2005).
20. D. M. Watkins, Y. Sayed-Sweet, J. W. Kilmash, N. J. Turro, and D. A. Tomalia, *Langmuir* 13, 3136 (1997).
21. M. H. Kleinman, J. H. Flory, D. A. Tomalia, and N. J. Turro, *J. Phys. Chem. B* 104, 11472 (2000).
22. W. Chen, D. A. Tomalia, and J. L. Thomas, *Macromolecules* 33, 9169 (2000).
23. P. M. R. Paulo, R. Gronheid, F. C. De Schryver, and S. M. B. Costa, *Macromolecules* 36, 9135 (2003).
24. J. Zhang, J. T. Petty, and R. M. Dickson, *J. Am. Chem. Soc.* 125, 7780 (2003).
25. I. W. Lee, Y. Bae, and A. J. Bard, *J. Am. Chem. Soc.* 126, 8358 (2004).
26. D. Wang and T. Imae, *J. Am. Chem. Soc.* 126, 13204 (2004).
27. D. Wu, Y. Liu, C. He, and S. H. Goh, *Macromolecules* 38, 9906 (2005).
28. D. Onoshima and T. Imae, *Soft Matter* 2, 141 (2006).
29. D. Wang, T. Imae, and M. Miki, *J. colloid Interface Sci.* 306, 222 (2007).
30. L. Pastor-Pérez, Y. Chen, Z. Shen, A. Lahoz, and S.-E. Stiriba, *Macromol. Rapid Commun.* 28, 1404 (2007).
31. O. Yemul and T. Imae, *Colloid Polym. Sci.* 286, 747 (2008).
32. K. Tamano and T. Imae, *J. Nanosci. Nanotechnol.* 8, 4329 (2008).
33. G. Jayamurugan, C. P. Umesh, and N. Jayaraman, *Org. Lett.* 10, 9 (2008).
34. H. Sugimura, A. Hozumi, T. Kameyama, and O. Takai, *Surf. Interface Anal.* 34, 550 (2002).
35. K. Inoue, M. Michimori, M. Okuyama, and Y. Hamakawa, *Jpn. J. Appl. Phys.* 26, 805 (1987).
36. A. Bernard, E. Delamarche, H. Schmid, B. Michel, H. R. Bosshard, and H. Biebuyck, *Langmuir* 14, 2225 (1998).
37. N. L. Jeon, I. S. Choi, G. M. Whitesides, N. Y. Kim, P. E. Laibinis, Y. Harada, K. R. Finnie, G. S. Girolami, and R. G. Nuzzo, *Appl. Phys. Lett.* 76, 4201 (1999).
38. H. X. He, Q. G. Li, Z. Y. Zhou, H. Zhang, S. F. Y. Li, and Z. F. Liu, *Langmuir* 16, 9683 (2000).
39. Y. Koide, Q. Wang, J. Cui, D. D. Benson, and T. J. Marks, *J. Am. Chem. Soc.* 122, 11266 (2000).
40. C. R. Kagen, T. L. Breen, and L. L. Kosbar, *Appl. Phys. Lett.* 79, 3536 (2001).
41. T. L. Breen, P. M. Fryer, R. W. Nunes, and M. E. Rothwell, *Langmuir* 18, 194 (2002).
42. H. Seidel, L. Csepregi, A. Heuberger, and H. Baumgaertel, *J. Electrochem. Soc.* 137, 3612 (1990); H. Seidel, L. Csepregi, A. Heuberger, and H. Baumgaertel, *J. Electrochem. Soc.* 137, 3626 (1990).
43. H. Sugimura and N. Nakagiri, *Appl. Phys. A* 66, S427 (1998); H. Sugimura, K. Ushiyama, A. Hozumi, and O. Takai, *Langmuir* 16, 885 (2000).
44. L. Hong, H. Sugimura, T. Furukawa, and O. Takai, *Langmuir* 19, 1966 (2003); L. Hong, K. Hayashi, H. Sugimura, O. Takai, N. Nakagiri, and M. Okada, *Surf. Coat. Technol.* 169, 211 (2003).
45. The oxidation of methyl groups of ODS on Si substrates by UV light was strongly depended on the proximate gap between the substrate and photomask, and the pressure of oxygen.
46. C.-C. Chu and T. Imae, *Macromol. Rapid Commun.* 30, 89 (2009).
47. G. Beamson and D. Briggs, High Resolution XPS of Organic Polymers: The Scienta ESCA300 database, John Wiley and Sons, New York (1992).
48. R. Schlapak, D. Armitage, S.-N. Zeni, G. Latini, J. H. Gruber, P. Mesquida, Y. Samotskaya, M. Hohage, F. Cacialli, and S. Howorka, *Langmuir* 23, 8916 (2007).
49. S. E. Koh, K. D. McDonald, D. H. Holt, C. S. Dulcey, J. A. Chaney, and P. E. Pehrsson, *Langmuir* 22, 6249 (2006).

Received: 26 September 2010. Accepted: 21 October 2010.